Identification of a dynamic center line model and its implementation in FLORIDyn

A comparison between MOESP and DMDc system identification

S.H. Halvorsen

Master of Science Thesis

Delft University of Technology

Delft Center for Systems and Control

Identification of a dynamic center line model and its implementation in FLORIDyn

A comparison between MOESP and DMDc system identification

MASTER OF SCIENCE THESIS

For the degree of Master of Science in Systems and Control at Delft University of Technology

S.H. Halvorsen

June 23, 2022

Faculty of Mechanical, Maritime and Materials Engineering (3mE) · Delft University of Technology

Abstract

Wind energy plays an essential role in the transition to a sustainable future and wind turbines allow us to utilize it. Wind turbines are often installed in close proximity to make the best use of the given space and to save costs. This also has the disadvantage that the turbines influence each other due to wakes. This is where wind farm control strategies can help to increase the power generated by the farm again. Model based wake steering is a promising strategy which utilizes a surrogate model to determine the best set-points for the wind farm. FLORIDyn is one surrogate model which provides basic flow dynamics at a very low computational cost.

In this thesis we increase the fidelity of FLORIDyn by extracting features from high fidelity simulations and extending the model. A crucial element of the wake description is the center line, especially for wake steering. We present a pipeline which 1.) extracts the center line from given flow field data, 2.) converts the center line into FLORIDyn model inputs, 3.) identifies a state-space model to translate the low fidelity center line behaviour to one closer to the high fidelity, and eventually 4.) extends the model.

To achieve this, we test and compare DMDc and MOESP system identification methods in two simulation cases with a 10 deg and 20 deg yaw step. The results indicate that the DMDc implementation has a better fit than the MOESP models. To get an idea of the general behaviour, we also test the models in a 15 deg case they have not been trained for.

Previously, the FLORIS and FLORIDyn parameters had only been trained for steady state conditions. This study can be seen as a proof-of-work that shows that dynamic extensions for FLORIDyn are possible, and how to perform this for the center line. The DMDc system identification showed to be a promising tool in identifying high fidelity dynamics from SOWFA simulations, due to its ability of identifying large scale physical systems. Research on the implementation of the FLORIDyn model in a model based wake steering framework is required to make a trade-off between the need for a more dynamical model, and following additional computational cost.

The current application of the framework is limited to the use of two dimensional SOWFA flow field snapshots at hub height, a turbulence free environment, the use of a single wind velocity and single yaw step data in the system identification. Further research and more extensive training data is required to broaden the framework to more real-life scenarios. Furthermore,

the computational efficiency of the identified DMDc model can still be improved by decreasing the amount of center line states, making it better applicable in a model based framework.

Table of Contents

List of Figures

List of Tables

Acknowledgements

I would like to thank my supervisors Prof.dr.ir. J.W. van Wingerden and Ir. M. Becker for the opportunity to study the topic and their guidance during the writing of this thesis. I would especially like to thank Ir. M. Becker for all his time and for our weekly meetings. It helped me a lot in making and reaching weekly goals. Furthermore, thank you for your help on the topic, with SOWFA, FLORIDyn and your critical eye on my findings and thesis. I would like to wish you the best of luck with your further research and development of FLORIDyn.

Furthermore, I would like to thank my thesis committee, consisting of Prof.dr.ir. J.W. van Wingerden, Dr.ir. D.J.N. Allaerts, Ir. M.J. van den Broek and Ir. M. Becker, for their interest in my work and their honest judgement.

Finally, I would like to thank all my friends, family and girlfriend for their support over the last years. Even-though the last three years have been overshadowed by the corona pandemic at multiple instances, you guys helped me stay motivated. The regular walks and coffee breaks with my roommates during lock downs and long weeks working from home definitely helped out a lot. Thank you all!

Delft, University of Technology
June 23, 2022

S.H. Halvorsen

Chapter 1

Introduction

1-1 Background information

In 2015, the Paris Climate Change Agreement was established. The goal of the agreement is to keep global warming below 1.5 °C by decarbonising the economy by 2050. One promising renewable energy source that could make a major contribution to this goal is offshore wind. Expectations of the European Commission are for the EU to generate at least 240 gigawatts (GW) of wind power by 2050. International organizations, specialised in energy, estimate this number to be even higher [30]. Globally, the International Renewable Energy Agency (IREA) expects the energy generated by offshore wind to increase to 520 GW by 2050 from 20 GW in 2018. The expected capacity of past and following years can be observed in Figure 1-1 [20].

To reach this amount of energy produced by offshore wind, more and larger wind farms are build. To give an idea of the increase in amounts of wind farms, current and planned farms in North-West Europe are depicted in Figure 1-2. Not only the amount and size of wind farms are increasing. In addition, the size of wind turbines that are being developed is also increasing. The development of wind turbine sizes over the years is depicted in Figures 1-3 and 1-4, with Figure 1-3 showing the comparison to some famous landmarks worldwide and the prediction of next-gen turbines up to 15 MW a piece. Figure 1-4 not only shows the development of wind turbine sizes, but also the average of wind turbines installed per project over the years, which is related to the number of turbines in a single wind farm. At the start of May 2021, the American federal government gave the green light for the nations first commercial offshore wind farm, which meets the expected size of both wind turbines and farms by Figures 1-3 and 1-4. Namely, a 84 turbine wind farm powered by 13 MW Haliade-X turbines from General Electrics [12].

A wind turbine converts kinetic energy of the wind into rotational energy by the blades. The rotational energy is then converted by the generator into electrical power. Due to the reduction of the kinetic energy in the flow, the downstream region of the turbine has a lower

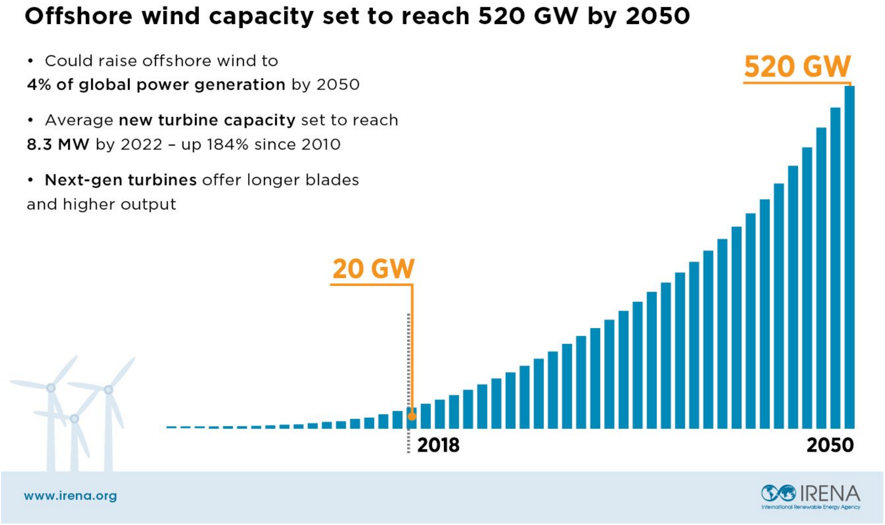

Figure 1-1: Prediction for global offshore wind capacity by the International Renewable Energy Agency [20].

wind speed and increased turbulence intensity. This area of decreased wind speed is called the wake. A turbine located in the wake of another turbine, produces less power and both its rotor blades and tower accumulate greater fatigue damage over time. A study by Nilsson et al. showed that this wake effect can bring the efficiency from an entire wind farm down by as much as 54% [26]. This can translate to a 20 to 30% power loss yearly [10] [23]. The lower wind speed in a wake still has noticeable influence at downwind turbines located 7 to 10 times the rotor diameter (denoted as D) away [2]. With the newest 13 MW turbine of GE having a rotor diameter of 220 m, the wake can get up to 2 kilometers in length [17]. Because of high installment and cable cost, wind turbines are installed at distances closer than 10 D [6]. Thus resulting in a decrease in wind farm efficiency.

1-2 Wind farm control

To decrease the effects of wakes at downwind turbines, and thus increase the efficiency of a wind farm, different control methods can be used. The traditional way of control is the 'greedy' controller, where every turbine maximizes its own power without the consideration of neighboring turbines. Different strategies exist that increase the total efficiency of a multiple turbine set-up. Two of these control strategies, that can be applied to stationary turbines, are introduced in Section 1-2-1. However, to enable real time wind farm control, model based control is required. This is due to the complicated aerodynamic interaction within wind farms. Model based control requires a computationally inexpensive wake model, that is able to reliably model the complicated and dynamical wake interactions [23]. Section 1-2-2 introduces one promising model based control method, after which Section 1-2-3 introduces the three wind farm models used in this study.

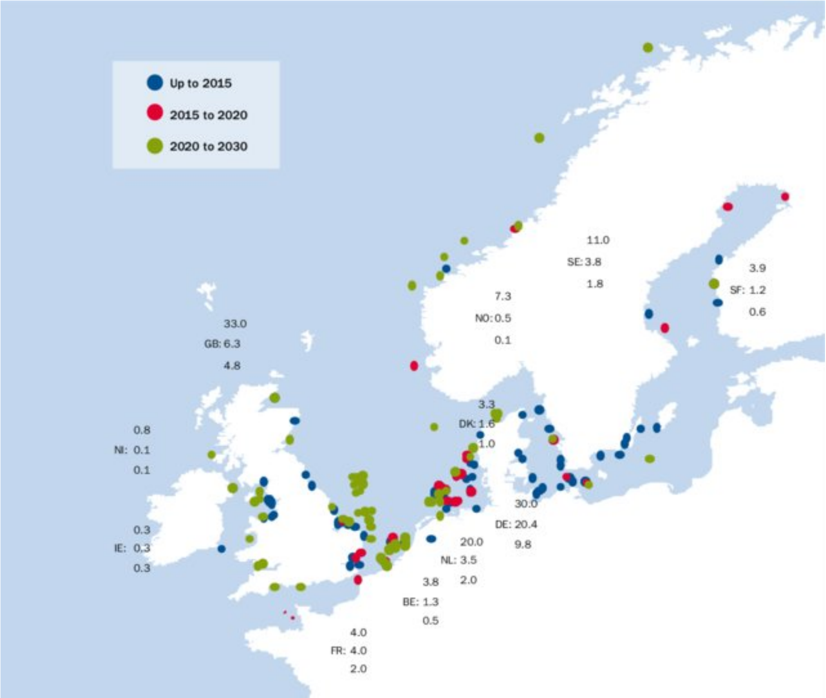

Figure 1-2: Prediction for offshore wind capacity by the International Renewable Energy Agency [37].

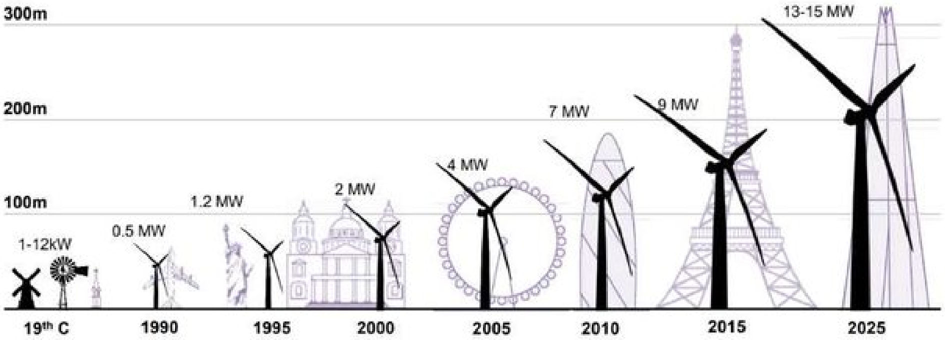

Figure 1-3: Evolution of wind turbine size and power output over the years [28].

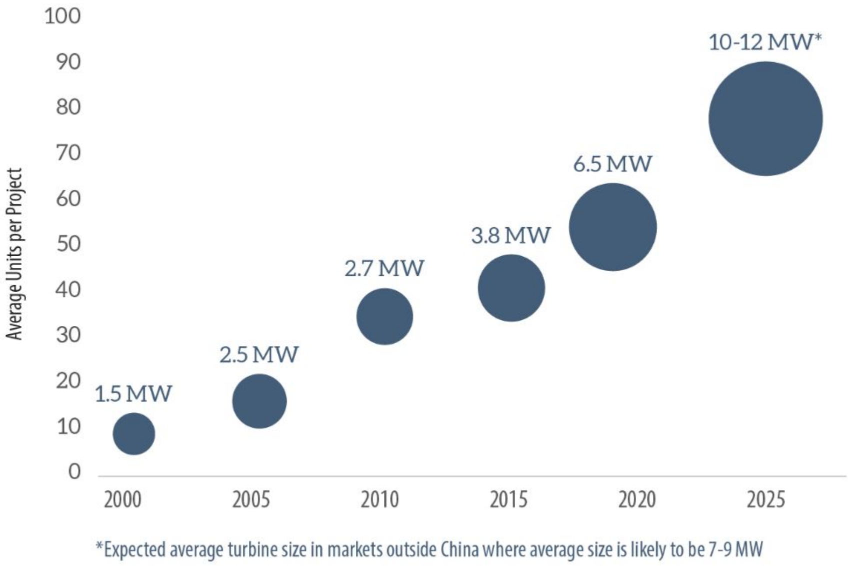

Figure 1-4: Evolution of wind turbine size and turbines per wind farm over the years [28].

1-2-1 Wind farm control strategies

For stationary turbines, two control strategies exist for mitigating the effects of aerodynamic coupling in a wind farm. The largest negative effect of aerodynamic coupling is the decrease in power output by turbines operating in the wake of other turbines. These two control strategies are depicted in Figure 1-5. The first method is power de-rating or axial induction-based control. The axial induction factor (a) describes the relation between the free wind speed and the wind speed at the rotor plane. From this relation, the thrust force of a turbine can be calculated and, therefore, the amount of energy it extracts from the wind, can be calculated. As shown in Figure 1-5a, de-rating the first turbine will decrease its influence on the wind. This will decrease its thrust force and, therefore, the extracted energy from the wind. The effect is a higher wind speed in the wake. Because the second turbine now experiences a higher wind velocity, its power output can be increased [23].

The second control strategy, shown in Figure 1-5b, is yaw-based wake steering or yaw-based wake redirection. The yaw angle, γ, or yaw of a turbine is the rotation of the rotor nacelle assembly (the turbine parts on top of the tower) around the tower of the turbine, or vertical axis. If a turbine would be located in the wake of another turbine in a greedy controlled wind farm, yaw-based wake steering would enable the upstream turbine to yaw and therefore 'steer' its wake away from the second turbine. The application of yaw-based wake steering in small setups and different simulations shows very promising results in increasing the efficiency of down wind turbines more, than the efficiency drop of yawed turbines [23]. This results in yaw-based wake steering being a superior control method over greedy control in the case of power maximisation.

One of the reasons for this wake redirection, stated by Burton et al, is due to the misalignment of the rotor plane with the incoming wind [9]. Therefore, different aerodynamic loads result in in-balanced load projections, resulting in gains in the wind's momentum in cross-

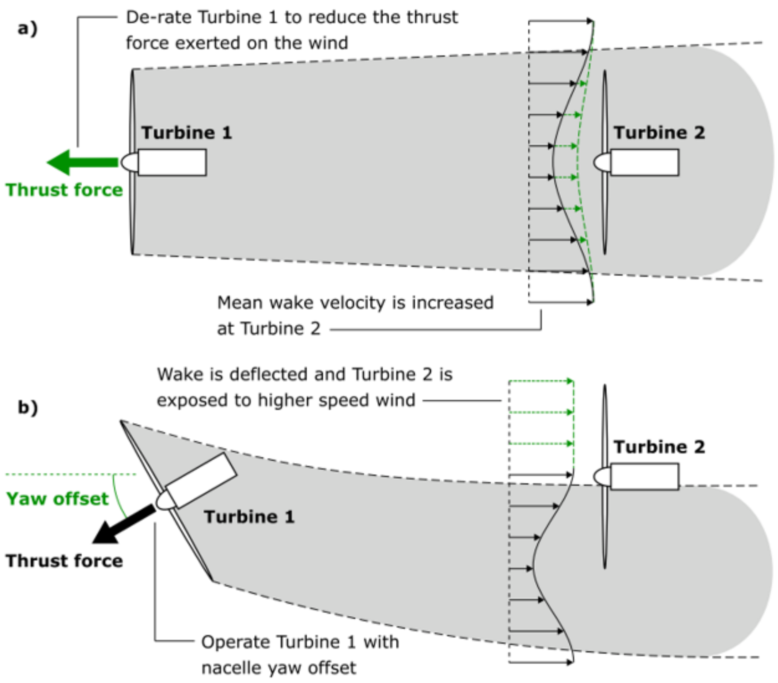

Figure 1-5: Wind farm control methods [23].

wind direction [23]. The second contribution of the wake redirection is due to the vertices that originate from these loads [16] [23]. The result of the steered wake is again visible in Figure 1-5b, where turbine 2 again experiences an increase in average wind speed, resulting in higher power output.

1-2-2 Model based control

Different studies in both literature and practice have been performed in implementing axial induction control and yaw-based wake steering [23]. Most studies focus on model-based control, mainly (variations of)Model Predictive Control (MPC). The basis of MPC is depicted in Figure 1-6. MPC is based on optimizing the control input over the near future using a surrogate model. After one or multiple steps of this input are applied, the optimization is performed again.

How far we optimize the input into the future is depending on our prediction horizon. We recognize this in Figure 1-6, for the power reference, P_{ref}, our MPC has calculated the current control input u_0 actuated on the system until input u_N where N is the prediction horizon. In the surrogate model, the current and future model outputs, z_0 until z_N are calculated using the current wind farm outputs y_0 and future optimized control inputs [14] [11]. In simple terms, this means that for every control action we want to perform, our MPC controller and, therefore, our surrogate model already have to perform multiple iterations. This emphasizes the need for a computationally inexpensive wake model, while still being able to model complex wake behavior to obtain reasonable predictions [8].

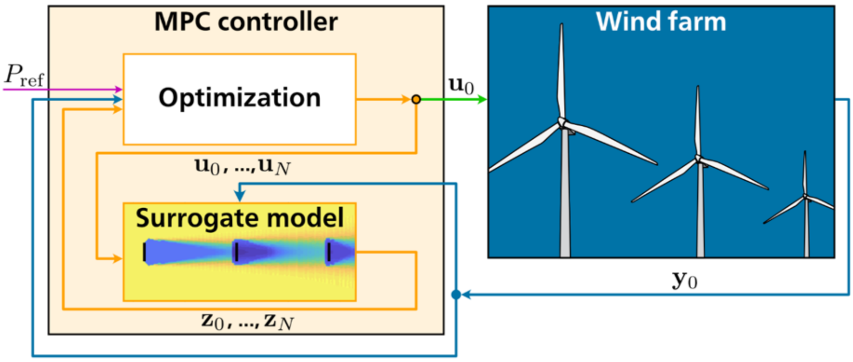

Figure 1-6: Wind farm control methods [3].

One study of Kheirabadi and Nagamune reviewed different studies of both power de-rating and yaw-based wake control [23]. Both control strategies were reviewed by studies using different optimization methods, control or optimization models, evaluation models, and even field and wind tunnel experiments. This study showed more promising results for yaw-based wake control with the objective of power maximization. Only a few studies showed a loss in efficiency, and the greatest increases in efficiency were found by high fidelity models, wind tunnel, and field tests. In the case of power de-rating, the increase of relative wind farm efficiency showed both positive and negative results for both field tests and model testing, regardless of the model fidelity. Low-fidelity models found the greatest increase in efficiency. The same conclusion is obtained by Boersma et al.. They state that literature shows that axial induction control will probably not increase power production, unless it is at the expense of increased structural loading. They furthermore state that yaw-based wake steering looks very promising and that more field testing is required to show its true potential [8].

1-2-3 Wind farm models

Different wake models exist, each with their own computational cost and fidelity. These models vary from very high-fidelity but computationally way too expensive to be used for model based control, to computationally very inexpensive static models. One example of such a high-fidelity is the open source model SOWFA and is often used in literature as a validation tool for models with less fidelity [27]. An example of a widely studied static model is FLORIS, a parametric model able of modelling the wakes and power outputs of different turbines in a farm. However, for implementation in model based control, dynamic wind farm models are preferred over these static models because they enable the use of closed-loop control methods and can account for model uncertainties [6]. One very promising dynamic model is FLORIDyn, it is an extension of FLORIS and also a parametric model with low computational cost [18]. It is able of transporting the steady-state FLORIS solution in downstream directions, resulting in a simplified approximation of dynamic wake propagation [23]. Latest work on FLORIDyn included the implementation of dealing with heterogeneous wind conditions, which is also very important to accurately model wakes in real live conditions [3]. Besides the low and high-fidelity models, medium-fidelity models like WFSim and FRED also exist.

These models are often based on two-dimensional Navier-Stokes equations. Differential equation solver tools are used to solve these partial differential equations [13]. Because FLORIDyn is parametric and not based on (simplifications of) natural laws, the interaction of modelled wakes with downstream turbines still lacks dynamics compared to medium or high-fidelity models.

1-3 Thesis goal and approach

This thesis explores SOWFA and FLORIDyn and makes a clear comparison in their performance. It furthermore finds the gap of dynamics in FLORIDyn compared to the higher fidelity SOWFA model. This gap is visible in electrical power output plots of two interacting turbines modelled by FLORIDyn and SOWFA. The power output of a downwind turbine modelled by FLORIDyn almost immediately increases or decreases when reached by state changes of upwind turbines through the wake. In high-fidelity models, these changes occur much more gradually. For FLORIDyn to become a more reliable model, which is required for model based control, it should also be able of modelling the state changes more dynamically. This thesis proposes a method of identifying a system relevant to accurately model the propagation of dynamically described yaw through the wake.

1-4 Thesis outline

The proposed method to solve the lack of wake advection in the FLORIDyn model is to identify the wake advection in SOWFA and translate this back to a more dynamic yaw description for FLORIDyn. The FLORIDyn model could be improved through the implementation of an identified system and translating the changing FLORIS turbine states to higher fidelity, dynamical turbine states in the traveling wake. Therefore, the main research question of the thesis will be:

Will the proposed cycle of identifying a state-space model relevant to accurately model the propagation of wind turbine state changes through the FLORIDyn wake improve the models performance?

The goal is to decrease the difference in electrical power output of turbines, and increase the wake advection description for different simulation cases of the FLORIDyn and SOWFA models. Targets that can be used to measure the improvement of the FLORIDyn model, are decreasing the difference of wake snap shots and turbine power outputs after a yaw step at the rotor plane. However, improvements should only minimally increase the computationally complexity of FLORIDyn.
Objectives:

- Decrease the difference in dynamic center line description and flow fields of FLORIDyn compared to SOWFA.

- Decrease the difference in electrical power output between FLORIDyn and SOWFA for multi-turbine cases.
- Optimize the FLORIDyn model at minimum cost of computational power.

1-4-1 Roadmap

To answer the main research question, different research questions about the proposed identification and validation cycle have to be answered.

Is it possible to accurately extract a high-fidelity center line deflection from SOWFA simulations, from which high-fidelity FLORIDyn turbine states can be estimated?

In order to answer this question, we first have to look at which wake variables can be estimated from the SOWFA data. To achieve accurate wake variable estimations which can be compared to those of FLORIDyn, the data should exclude the effect of wake meandering. In case meandering does occur in the SOWFA simulations, multiple simulations would show different wake advection. This is because the observed advection would include the meandering dynamics. Because no time-averaged SOWFA data can be used to eliminate the meandering dynamics, simulations without turbulence are used.
The steps that should be taken to answer this research question are:

1. Run turbulence free single turbine SOWFA and FLORIDyn simulations, with a yaw steps of 10 deg and 20 deg and a wind speed of $9.2\,\mathrm{m\,s^{-1}}$.
2. Extract the center line from the SOWFA data.
3. Identify the center line deflection from the wake data.
4. Evaluate the fidelity of the identified deflection and filter the data if necessary.
5. Identify the high-fidelity yaw of the FLORIDyn and SOWFA simulations through parameter estimation.

Is it possible to identify systems translating the FLORIDyn turbine states to more dynamical turbine states and implement these into FLORIDyn to achieve better wake advection?

Different input-output identification methods of the dynamic systems can be performed using the FLORIDyn yaw as the input and the estimated high-fidelity yaw as the output. Both the use of SISO and SIMO system identification can be performed and implemented.

1. Perform both SISO and SIMO MOESP system identification.
2. Perform SIMO Dynamic Mode Decomposition with Control system identification.
3. Evaluate the systems on performance and robustness.
4. Implement the best performing system in FLORIDyn.
5. Evaluate the effect to the dynamic wake behaviour, based on flow field plots of the single turbine case, and the power output of the two turbine case.

How robust are the identified systems to other simulation cases?

To answer the final research question, a validation of the new FLORIDyn model has to be performed. This validation is performed by a two turbine case, and should be using a different γ -step amplitude.

1. Acquire validation data: two turbine case under a different γ -step. Perform the same simulations with the new FLORIDyn model.
2. Perform validation between the SOWFA validation data and FLORIDyn data.

1-5 Scope research project

The goal of the research will be answering the previous main research question, supported by the three sub questions. The scope of the research is mainly narrowed down the the following statements:

- The training data will only be extracted from a single turbine case.
- Validation will be performed through single and two turbine cases.
- SOWFA is assumed to have similar wake behaviour as in reality. Real turbine measurements are outside the scope of this study.
- The study will not take minimizing steady state power output and flow field offsets into account and will focus an the dynamical behaviour of the wake and power output.

Chapter 2

Overview of the models: SOWFA, FLORIS, FLORIDyn

Different wind farm models already exist, ranging from high to low fidelity. High fidelity models are based on Computationally Fluid Dynamics (CFD) and describe large eddies traveling through the wake in detail. Therefore, they are often called Large Eddy Simulations (LES). Medium fidelity simulations are often simplifications of these models. They are still based on elementary laws of nature but with assumptions and are less detailed. Finally, low fidelity models are parametric or different analytical models which approximate the wake behavior. Due to the absence of differential equations, they are computationally superior to medium and high-fidelity models. However, parameters are only tuned for the model to satisfy specific circumstances and often miss out on complex dynamical interactions.
This section will elaborate more on the different wake models used in this study. It briefly explains the background of the used high-fidelity model, SOWFA, in Section 2-1. Furthermore, it explains the basic workings two different low-fidelity models. This includes two versions of FLORIS models in Section 2-2 and its dynamic predecessor, FLORIDyn, in Section 2-3.

2-1 SOWFA

The high-fidelity model SOWFA stands for Simulator for Offshore Wind Farm Applications and is developed by the National Renewable Energy Laboratory (NREL) [27]. It is based on the CFD software OpenFOAM [29]. SOWFA is capable of performing LES of wind turbines in close to realistic conditions. An example of such a SOWFA simulation is depicted in Figure 2-1. Here, a slice at hub height is visible from two turbines (the black lines) located 900 m apart. The first turbine is yawed by 20 deg. The eddies in the wake are visible in the figure. The effect of yaw-based wake steering is furthermore visible. Because SOWFA is of such high fidelity, depending on the complexity, a steady-state simulation of 600 s can take up to three weeks to calculate on a single core [36]. However, because of this complexity, SOWFA simulations are often used as validation data [36] [3] [7].

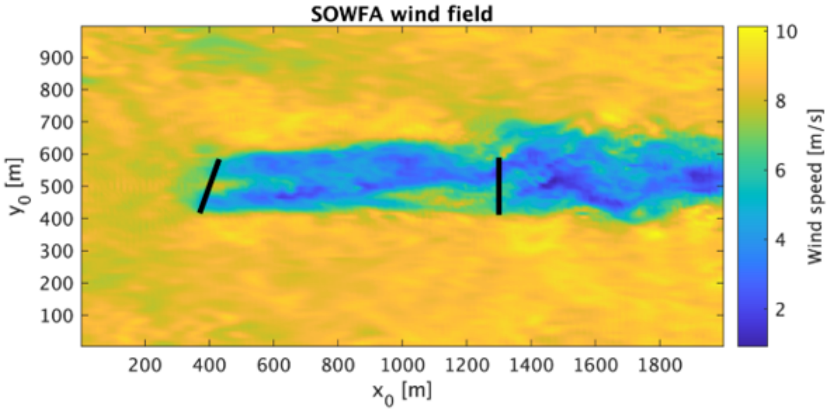

Figure 2-1: Slice at hub height of a SOWFA two turbine case simulation [3].

2-2 FLORIS

In 2014, Gebraad et al. introduced a data-driven parametric wind plant model called FLORIS: FLOw Redirection and Induction in Steady-state. FLORIS can be used in a wind farm controller to optimize yaw and induction settings for power maximization while reducing turbine loads. FLORIS is a static model able to predict steady-state wake locations, flow velocities, and turbine power outputs. Control variables in the model are yaw angles and axial induction factors of the turbines. Furthermore, model parameters are estimated based on turbine power productions and yaw angles. In their study, Gebraad et al. used SOWFA to develop FLORIS and identify its parameters. They furthermore used a game-theoretic approach to develop a model-based yaw steering control scheme. A proof of concept was done by implementing this scheme in SOWFA, where validation simulations showed its potential [19]. The following subsections elaborates more on the zone FLORIS model of Gebraad et al. and the Gaussian model developed by Bastankhah in 2016 [2].

2-2-1 The Zone FLORIS model

In the zone FLORIS model, the wake exists out of three wake zones and a center line description. The three wake zones as depicted in Figure 2-2(a) are an extension of the Jensen model [21]. The wake was expanded proportionally to the axial downstream distance with a uniform wind velocity of the wake. In the zone FLORIS model, each wake zone has its own velocity description and expansion factor. This is introduced, because closer to the edge, the wake has a faster wind speed recovery. Wake zones 1, 2, and 3 are respectively called the near, far, and mixing zone. In later studies, small changes are proposed to the zone FLORIS model to improve the center line deflection description and to fix discontinuities [35].

Center line description The wake center line in Figure 2-2(a) of turbine i at downwind position $x > X_i$, where X_i is the downwind position of the turbine, is given as:

$$y_{\mathrm{w},i}(x) = Y_i + \delta y_{\mathrm{w,\ rotation}\ ,i}(x) + \delta y_{\mathrm{w,\ yaw}\ ,i}(x) \tag{2-1}$$

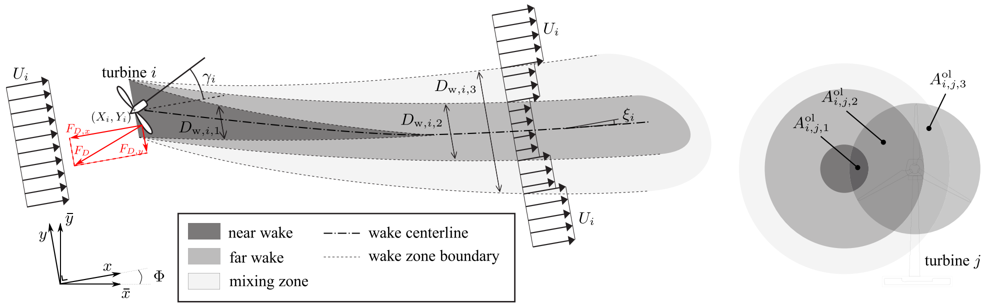

(a) Top view

(b) Cut-through at downstream turbine

Figure 2-2: Top (a) and downstream cut-through view (b) of the zone FLORIS model [19].

Where $\delta y_{\text{W, rotation }, i}(x)$ is the rotation-induced wake lateral offset. This offset occurs because the clockwise rotating blades of a turbine induces a small wake deflection and is described as the following linear function:

$$\delta y_{\text{w, rotation }, i}(x) = a_d + b_d \left[x - X_i\right] \tag{2-2}$$

Furthermore, $\delta y_{\text{w, yaw }, i}(x)$ is the yaw induced offset and is a function of the angle of the center line of the wake ξ_i:

$$\xi_i(x) \approx \frac{\xi_{\text{init }}\left(a_i, \gamma_i\right)}{\left[1 + 2k_d \frac{x - X_i}{D_i}\right]}^2 \text{ with } \xi_{\text{init }}\left(a_i, \gamma_i\right) = \frac{1}{2}\cos^2\left(\gamma_i\right)\sin\left(\gamma_i\right)C_T\left(a_i\right) \tag{2-3}$$

With D_i the rotor diameter, k_d a model parameter linked to the wake deflection and $\xi_{\text{init }}$ the initial angle of the wake at the rotor. Furthermore, $C_T\left(a_i\right) = 4a_i\left[1 - a_i\right]$ and is the thrust factor of a non-yawed turbine.

Turbine power output In the FLORIS model introduced by Gebraad et al., the power output P of a turbine $i \in \mathcal{F}$, where $\mathcal{F} = \{1, 2, \cdots, N\}$ denotes the set of turbines in a wind plant with N the total number of wind turbines, is given as:

$$P_i = \frac{1}{2}\rho A_i C_P\left(a_i, \gamma_i\right) U_i^3 \forall i \in \mathcal{F} \tag{2-4}$$

Here, ρ is the air density, A_i is the rotor swept area, C_{P} is the power coefficient of the turbine, and U_i the effective wind speed at the turbine ([19]). The power coefficient is furthermore a function of a_i and γ_i:

$$C_P\left(a_i, \gamma_i\right) = 4a_i\left[1 - a_i\right]^2 \eta\cos\left(\gamma_i\right)^{p_P} \tag{2-5}$$

With η a constant scaling to account for losses and p_P a parameter value equal to 2, obtained through wind tunnel tests.

2-2-2 The Gaussian FLORIS model

Instead of three different wake zones, Bastankhah and Porté-Angel suggested a Gaussian fit to the wind velocity outside the near wake, or potential core [2]. Using experimental wind tunnel data, they showed this normalized self-similar Gaussian fit to be a reasonable wake description, while varying over downwind distance and being independent of the turbine yaw angle. This way of modeling the wake is visualized in Figure 2-3. The potential core is the grey triangle, spanned by the un-yawed turbine blade tips and the point $x = x_0$, depending on γ and C_T. Inside the potential core, both the wind speed $u = u_0$ and flow angle $\theta = \theta_{c_0}$ are considered constant. After x_0, the wake center starts to recover, and θ_{c_0} decreases.
The study furthermore showed, that the wake growth rate is independent of the yaw angle and is mainly influenced by incoming flow characteristics. Where the zone FLORIS model does not include flow characteristics, the turbulence intensity is included in the Gaussian FLORIS model. The Gaussian model furthermore models the wake in the third dimension.

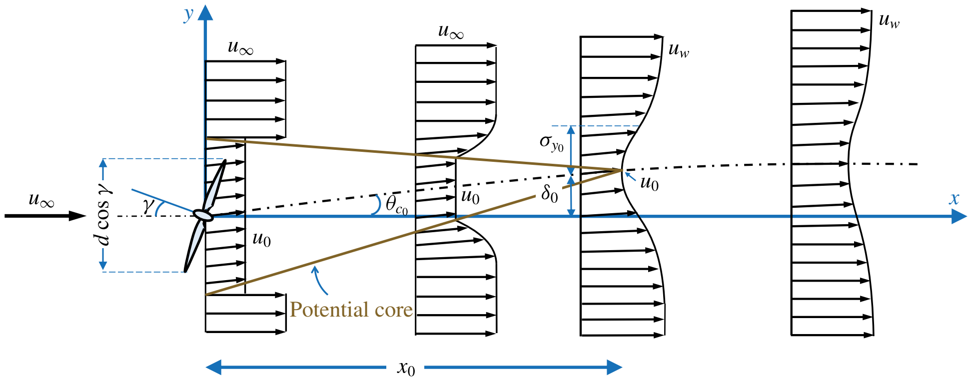

Figure 2-3: Wake shape of the Gaussian model with the near and far wake characteristics [2].

2-3 FLORIDyn

FLORIDyn is an extension of FLORIS, able to model the dynamic wake propagation effects. These propagation effects result in time delays between changes in control settings of a turbine, axial induction and yaw angle, and their effect on downwind turbines. This is due to the implementation of observation points that 'travel' through the wake. FLORIDyn was developed by Gebraad and Van Wingerden and stands for FLOw Redirection and Induction Dynamics [18]. This section introduces three different FLORIDyn models. First, the original Zone FLORIDyn model from Gebraad and Van Wingerden is introduced in Section 2-3-1. This is followed by the Gaussian FLORIDyn model in Section 2-3-2 and the latest FLORIDyn Center Line model in Section 2-3-3. After these Sections, we compare results from the most recent FLORIDyn model with SOWFA results in Section 2-3-4. After this comparison, the improper wake advection in FLORIDyn is established as the research gap on this model. This is treated in Section 2-3-5.

2-3-1 The Zone FLORIDyn model

Like FLORIS, FLORIDyn is a parametric model, and depends on 17 parameters. It furthermore has the potential to be used for dynamic optimization within model-based control due to its computational cheapness compared to other dynamic wake models. As in the zone FLORIS model, the wake of the FLORIDyn model from Gebraad and Van Wingerden was divided into zones. Gebraad and Van Wingerden used a seven zone description, each with their own expansion and wind speed recovery properties.

To dynamically describe the wake, Observation Points (OPs) are introduced. A visual representation of this is depicted in Figure 2-4. OPs are created at the rotor plane and travel through the wake with the discrete-time step k. At every time step, the turbine measurements γ_T, a_T, and U_T are passed down to the next observation point. Figure 2-4 furthermore shows how FLORIS, in combination with a linear relation, is used to update the downwind and crosswind location of the OPS. Deflection and expansion of the wake zones are then calculated similarly as in FLORIS, after which the effective flow velocities at the downstream turbines can be estimated. The latter is done through the use of reduction factors, which make it possible to include the influence of multiple wakes on OPs.

2-3-2 The Gaussian FLORIDyn model including heterogeneous flow

In 2022 Becker et al. developed a FLORIDyn model with an underlying Gaussian FLORIS model [5]. To go to a three dimensional flowfield, a sunflower distribution is used to distribute the OPs in the crosswind plane. The algorithm is based on Vogel's application of the sunflower distribution [41]. These OPs now inherent the states from the turbine they originate from and the time step they were created. The turbine on his part saves the states necessary for calculating the wake and their trajectory: γ, a , and the wind speed at the rotor plane. Becker furthermore introduced chains of OPs, where all OPs created at the same relative position in the wake form a chain. Chain ID data is stored at the OPs. The turbine OPs belong to their relative position in the wake, and their relative area is now stored once for the entire chain, resulting in reduced computational load [3] [5].

The travel speed of OPs was also changed. They now travel at the free wind speed, in comparison to the effective wind speed. Initial two-turbine case simulations with FLORIDyn and their validation with SOWFA showed that OPs traveling at their own wind speed show a too large delay in 'delivering' state changes to downwind turbines. However, this does result in state changes arriving at downwind turbines too fast [3]. Another problem with OPs traveling with the effective wind speed was that it leads to overlapping areas between slower and faster OPs, which describe different turbine states. A final advantage of the free wind speed implementation, is that the effective wind speeds of the OPs do not have to be calculated any more at ever time step, decreasing the computational load. This is only required for the OPs at the rotor planes to calculate the turbine power output [5].

As shortly mentioned in Section 2-3-1, is the calculation of reduced wind speeds, u_{red}, in wakes done through the use of reduction factors. To be able to include a variable wind direction, the wind speeds have to be transformed to vectors. The free wind speed becomes two dimensional: $\mathbf{u} = [u_{x_0}, u_{y_0}]^\top$. With u_{x_0} and u_{y_0} the x and y velocities in the world coordinate system respectively. The reduced wind speed now becomes: $\mathbf{u}_{\text{red}} = \mathbf{u}(1 - r)$.

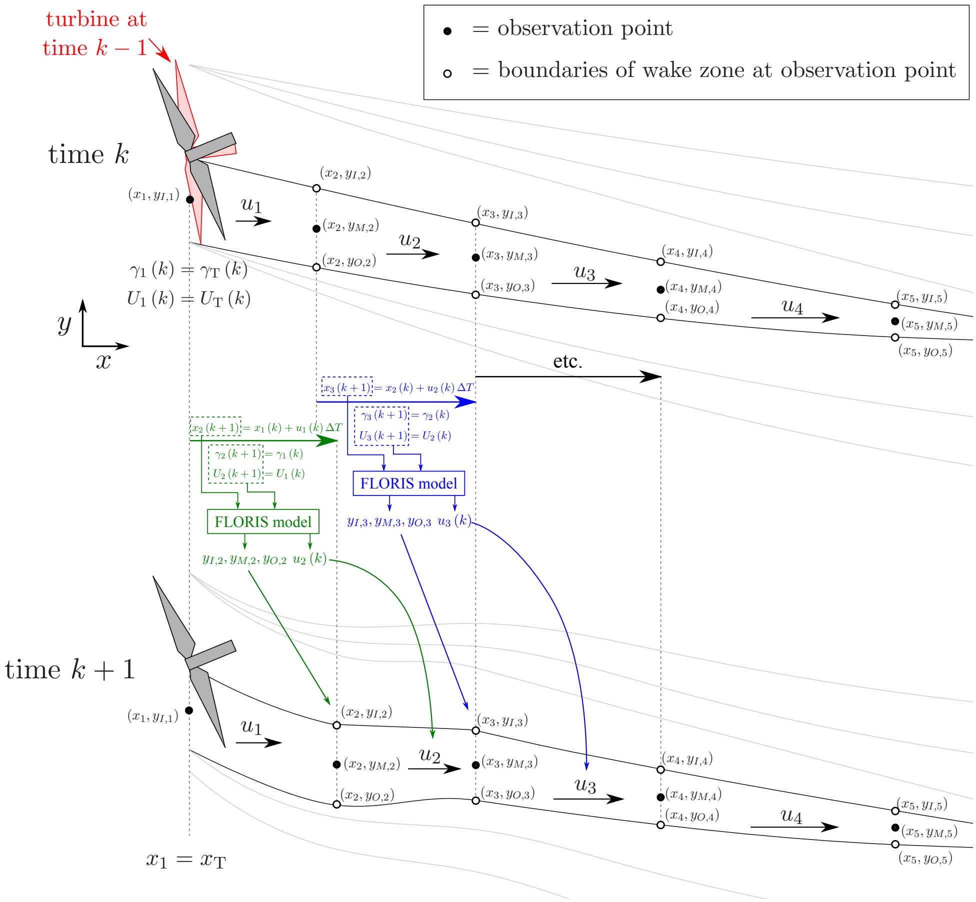

Figure 2-4: Illustration of the state update mechanism in the FLORIDyn model. Since we only consider one turbine and wake, t and z indices are omitted in the notation [18].

Because of the variable wind direction, Becker makes a differentiation between the wake coordinate system K_1 and the world coordinate system K_0. Resulting in indices for the coordinates equal to their matching system. Thus, x_1, y_1, z_1 being the OPs down and crosswind location in the wake and x_0, y_0, z_0 their location in the world coordinate system. The rotational matrix $\mathbf{R}_{01}$ is introduced to translate the wake coordinates of a turbine to the world coordinates:

$$r_0 = \begin{bmatrix} x_0 \\ y_0 \\ z_0 \end{bmatrix} = t_0 + \mathbf{R}_{01}(\varphi) r_1 = \begin{bmatrix} x_{0,\ \mathrm{T}} \\ y_{0,\ \mathrm{T}} \\ z_{0,\ \mathrm{T}} \end{bmatrix} + \begin{bmatrix} \cos\varphi & -\sin\varphi & 0 \\ \sin\varphi & \cos\varphi & 0 \\ 0 & 0 & 1 \end{bmatrix} \begin{bmatrix} x_1 \\ y_1 \\ z_1 \end{bmatrix} \tag{2-6}$$

Here, r_1 is the location vector in K_1, t_0 is the turbine location and r_0 is the location vector in the world [5]. Furthermore, $\mathbf{R}_{01}$ is used to update the location from an OP in the world coordinate system, $r_{0,0P}(k)$, to the next time step, $k+1$. This is done by first updating it's location in the wake coordinate system, $r_{1,\mathrm{OP}}(k) \rightarrow r_{1,\mathrm{OP}}(k+1)$. Updating $r_{0,0P}(k+1)$ is done through the following relation:

$$r_{0,\mathrm{OP}}(k+1) = \boldsymbol{r}_{0,\mathrm{OP}}(k) + \mathbf{R}_{01}\left(\varphi_{0,\mathrm{OP}}\right)\left[\boldsymbol{r}_{1,\mathrm{OP}}(k+1) - r_{1,\mathrm{OP}}(k)\right] \tag{2-7}$$

Becker visualised this in Figure 2-5, showing the process for both a constant and variable wind inflow direction [5].

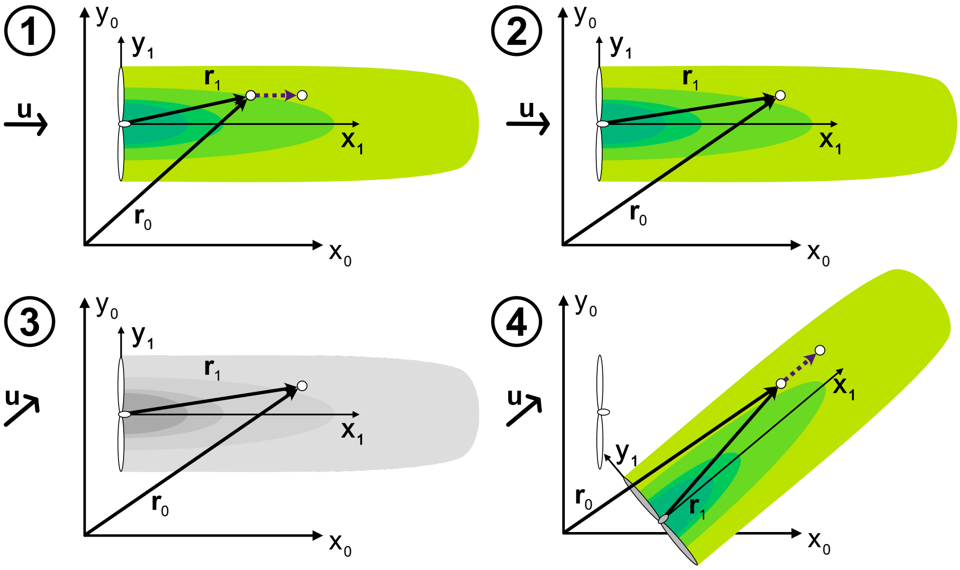

Figure 2-5: This figure visualizes the working of Equation 2-7, which is applied for each OP individually. In (1 → 2), the position update of an OP in a time step with a constant wind direction is depicted. (3 → 4) shows the position update when the wind direction changes. In this case, the wake coordinate system is rotated around the OP's location to match the new downstream direction. This causes the apparent origin of the wake in the world coordinate system to change, which is visualized by the gray turbine. [5]

2-3-3 FLORIDyn Center Line model

In the most recent FLORIDyn version from Becker, only one chain of OPs exist per turbine. Therefore, only one OP per turbine is created at the rotor center every time step. Resulting in the OPs following the center line [4]. The OPs have three different kind of states, the first being the OP location, x_{OP}, in both K_0 and K_1: $\mathrm{x}_{\mathrm{OP}} = [\mathrm{x}_{\mathrm{OP},0}, \mathrm{x}_{\mathrm{OP},1}]^\top$. The other sets consist of turbine states x_{T} and wind field states x_{WF}. The OP propagation is related to that of earlier FLORIDyn versions. The new downwind location $x_{\mathrm{OP},1,\mathrm{x}}$ depends on the old location, time step δt, and the free wind speed $x_{\mathrm{WF},\mathrm{u}}$. The crosswind location is described by the deflection function δ, depending on $x_{\mathrm{OP},1,\mathrm{x}}(k+1)$, x_{T} and x_{WF}. Both the down and crosswind updated locations are described in K_1 as follows:

$$x_{\mathrm{OP},1,\mathrm{x}}(k+1) = x_{\mathrm{OP},1,\mathrm{x}}(k) + \Delta t x_{\mathrm{WF},\mathrm{u}} \tag{2-8}$$

$$\mathbf{x}_{\mathrm{OP},1,\mathrm{y},\mathrm{z}}(k+1) = \delta\left(x_{\mathrm{OP},1,\mathrm{x}}(k+1), \mathbf{x}_{\mathrm{T}}, \mathbf{x}_{\mathrm{WF}}\right) \tag{2-9}$$

The translation of the OP location from K_1 to K_0 follows equation 2-7, where now the new OP states are used:

$$\mathbf{x}_{\mathrm{OP},0}(k+1) = \mathbf{x}_{\mathrm{OP},0}(k) + \mathbf{R}_{01}\left(\mathrm{x}_{\mathrm{WF},\varphi}\right) \underbrace{\left[\mathrm{x}_{\mathrm{OP},1}(k+1) - \mathrm{x}_{\mathrm{OP},1}(k)\right]}_{\text{step in } \mathcal{K}_1}, \tag{2-10}$$

Due to a sparse amount of OPs in the new center line based FLORIDyn model, Becker revised turbine influence on world locations [4]. To calculate the influence of turbine wakes on world locations $\mathbf{l}_0$, a method to extrapolate the wake influence was presented. This is done through identifying the two closest OPs of a turbine to $\mathbf{l}_0$ and interpolating their states to an artificial closest OP* on the center line. The inverted rotational matrix is then used to calculate the influence of a turbine on $\mathbf{l}_0$. This can be done for every turbine to create a Temporary Wind Farm (TWF). However, Becker only used the two closest OP* in his implementation to approximate the wake and wind field conditions in $\mathbf{l}_0$. The reader interested in the exact coordinate transformation is referred to Becker et al. 2022 [4].

2-3-4 Two turbine case: comparing SOWFA with FLORIDyn

This section will make a comparison between SOWFA and FLORIDyn through the use of a steady state wake snapshot and turbine power output. The used FLORIDyn model in this comparison with SOWFA and in the following sections is the FLORIDyn Center Line model of Becker from 2022 [4]. Figure 2-6 shows a velocity snapshot from the two turbine case from the FLORIDyn and SOWFA model and their error. The simulation is that of a 2 turbine set-up with a 20 deg yaw step of the upwind turbine, T0, at 300 s with a yaw speed of $0.3\,\mathrm{deg\,s^{-1}}$. The snapshot is taken at $\mathrm{t} = 1000\,\mathrm{s}$, at this moment, steady state is reached. Furthermore, the FLORIDyn center line of T0 is visualised in all plots. Two differences between the FLORIDyn and SOWFA snapshots are the velocity deficit overestimation around the blade tips and nacelle, and the exclusion of the induction zone in front of the turbines in FLORIDyn. Because the blade tip and nacelle error recover before the next turbine is reached, the error is assumed not to be relevant in this work. The FLORIDyn model furthermore slightly overestimates the wake steering. However, the error in front of T1 does not show large over or undershoots and is between $1.3\,\mathrm{ms}^{-1}$ and $-1.4\,\mathrm{ms}^{-1}$.

For the same two turbine case, the generated power was plotted in Figure 2-7. It shows a constant power underestimation of T0 by 0.13 MW by FLORIDyn. Furthermore, the increasing FLORIDyn generated power of T1 makes a sudden stop when reaching 1.061 MW, while in the SOWFA validation data an overshoot, followed by an undershoot, of the steady state power is visible. Furthermore, there occurs a power offset of 0.99 MW with FLORIDyn. This constant offset occurs because the FLORIDyn parameters are not trained in the 0 % TI case. Because training the steady state parameters of the power output is out of the scope of this research, the normalized generated power of this 2T case is shown in Figure 2-8. From these results, a similar difference between the dynamic SOWFA and FLORIDyn normalized generated power output, without the offset, is noticeable. Further differences in dynamics can be observed in the power output of a 2T case with a faster yaw-step of 15 deg with $1\,\mathrm{deg\,s}^{-1}$, as seen in Figure 2-9. As described in section 2-3-2, the OPs travel at free wind speed. Becker noted that this does result in state changes arriving to early at downwind turbines [5]. This can also be observed in the power plot of T1. Note that from 300 s to 400 s the generated power from T1 is still dropping from the flow field initialisation in SOWFA. However where the state changes in FLORIDyn reach T1 at 400 s, with an abrupt increase in its power output, a different behaviour occurs in the SOWFA validation data. Here, the power first experiences a drop around 424 s before rising. Furthermore, there is an overshoot of 1.05 MW compared to the FLORIDyn steady state.

2-3-5 Improper wake advection in FLORIDyn

FLORIDyn showed its overall potential as a computationally inexpensive dynamic control-oriented model. However, in two turbine case including a yaw step, it still shows a lack of dynamics needed to accurately approach the turbine electrical power output of the SOWFA simulation. In FLORIDyn, turbine state changes are stored unaltered in the OPs and are also not changed during the propagation. Once these OPs with the updated turbine states arrive at the downstream turbine, the turbine is directly affected by the change. Under natural circumstances the wake would show a characteristic reaction or development based on the turbine state change, which is missing in FLORIDyn. It can also be assumed that the downstream turbine has its own characteristic reaction to changes in the flow ([3]). Simply implementing a filter for the C_P alone is discouraged. Such a filter must be tuned for variations in other variables the power output depends on, such as the effective wind speed at the turbine rotor plane and its own and upstream turbine yaw angles. This would mean that different filters need to be identified for every extra turbine in a multi-turbine case. Therefore, the problem should be tackled at the upwind turbine, with a dynamical description of how turbine state changes propagate through their wake. To identify realistic realistic dynamics, and parameters describing these dynamics, the use of high-fidelity data is essential.

To identify the lack of turbine state dynamics, the two turbine flow field of FLORIDyn, SOWFA and their error is plotted at the moment the FLORIDyn yaw-induced wake dynamics reach the downwind turbine. This occurs at t = 400 s in the 20 deg yaw step of $0.3\,\mathrm{deg\,s}^{-1}$ 2T case and is visualised in Figure 2-10. It can be observed that the SOWFA yaw step of the wake

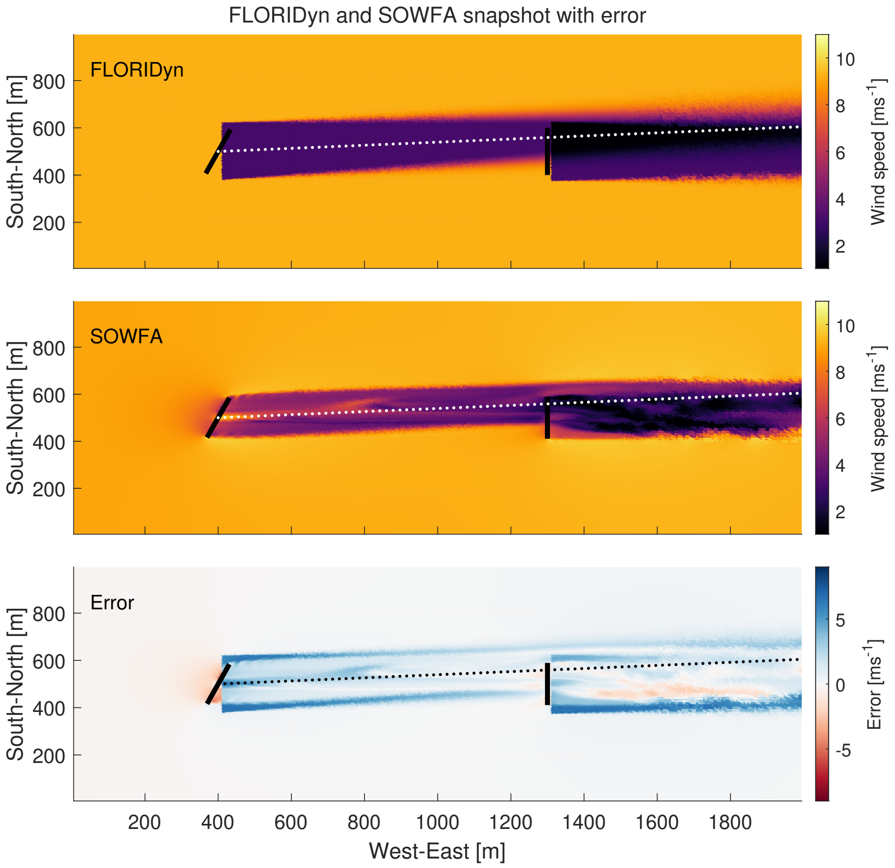

Figure 2-6: FLORIDyn, SOWFA and their error plot of a 2 turbine simulation with $20\,\mathrm{deg}$ yaw step of $0.3\,\mathrm{deg\,s^{-1}}$ by T0 at $300\,\mathrm{s}$. Snapshots taken at $1000\,\mathrm{s}$. The FLORIDyn center line of T0 is visualised in all plots.

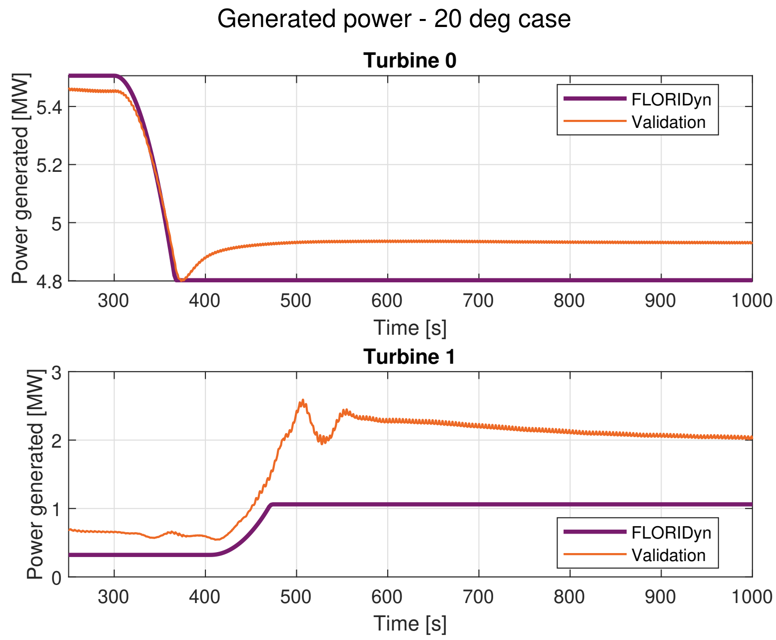

Figure 2-7: Power output over time of a 2 turbine simulation with $20\,\text{deg}$ yaw step of $0.3\,\text{deg}\,\text{s}^{-1}$ by T0 at $300\,\text{s}$.

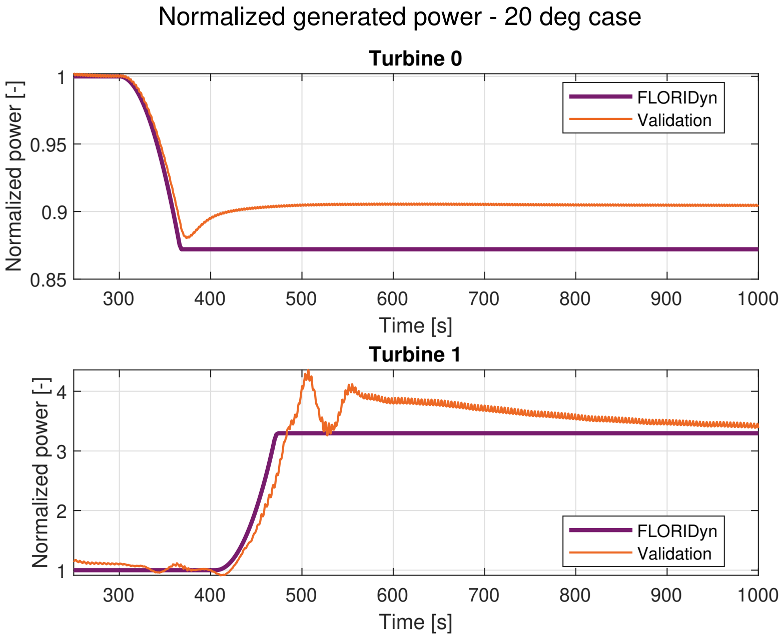

Figure 2-8: Normalized generated power output over time of a 2 turbine simulation with $20\,\text{deg}\,\text{s}^{-1}$ yaw step of $0.3\,\text{deg}\,\text{s}^{-1}$ by T0 at $300\,\text{s}$.

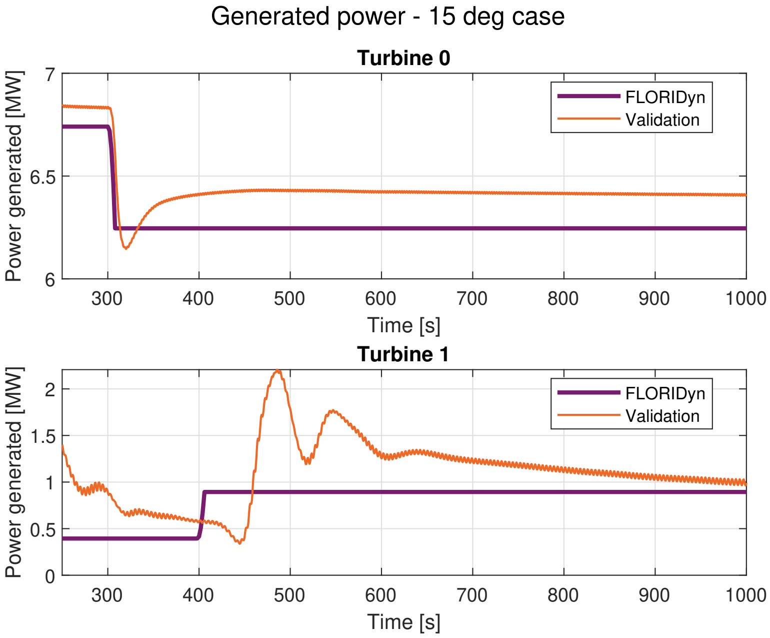

Figure 2-9: Power output over time of a 2 turbine simulation with $15\,\text{deg}$ yaw step of $2\,\text{deg}\,\text{s}^{-1}$ by T0 at $300\,\text{s}$.

is located at $1100\,\text{m}$. Furthermore, the SOWFA wake looks to have more of an S-shape at the location of the turbine state propagation, compared to the graduate ramp of the FLORIDyn wake. This indicates on an improper wake advection description in FLORIDyn. Advection is a broad term in physics and is defined as the exchange of energy, moisture, or momentum due to horizontal heterogeneity (Chang, 1968) or as the Cambridge dictionary describes: "the transport of a substance or heat by the flow of a liquid". Therefore, the movement of wakes through the free flow is called wake advection.

A more realistic wake advection description of upwind turbines could improve the downwind turbine power output in the two turbine case. A realistic approach of turbine electrical power output is required for FLORIDyn to satisfy as a model in MPC to optimize wind farm power output. This is because optimal control inputs and model predictions are calculated over multiple discrete time steps, the prediction horizon. For abrupt power changes in the model, the MPC might calculate abrupt optimal control inputs without taking the right delay into account.

Advection in other wake models In the FAST.Farm model, advection is depicted as the movement of a yaw step change through the wake [22]. To improve the wake advection and deflection description, all variables needed for the wake description are filtered by a recursive, single-pole low-pass filter with exponential smoothing [22]. In this model, the filtered states and parameters describing the wake are the rotor diameter D, γ, the axial wind velocity, and the turbulence intensity. Further filtered inputs for the boundary conditions at the rotor plane are C_T and the relative wind speed.

The filtered states are implemented to accelerate the wake from near to far wake and evolve

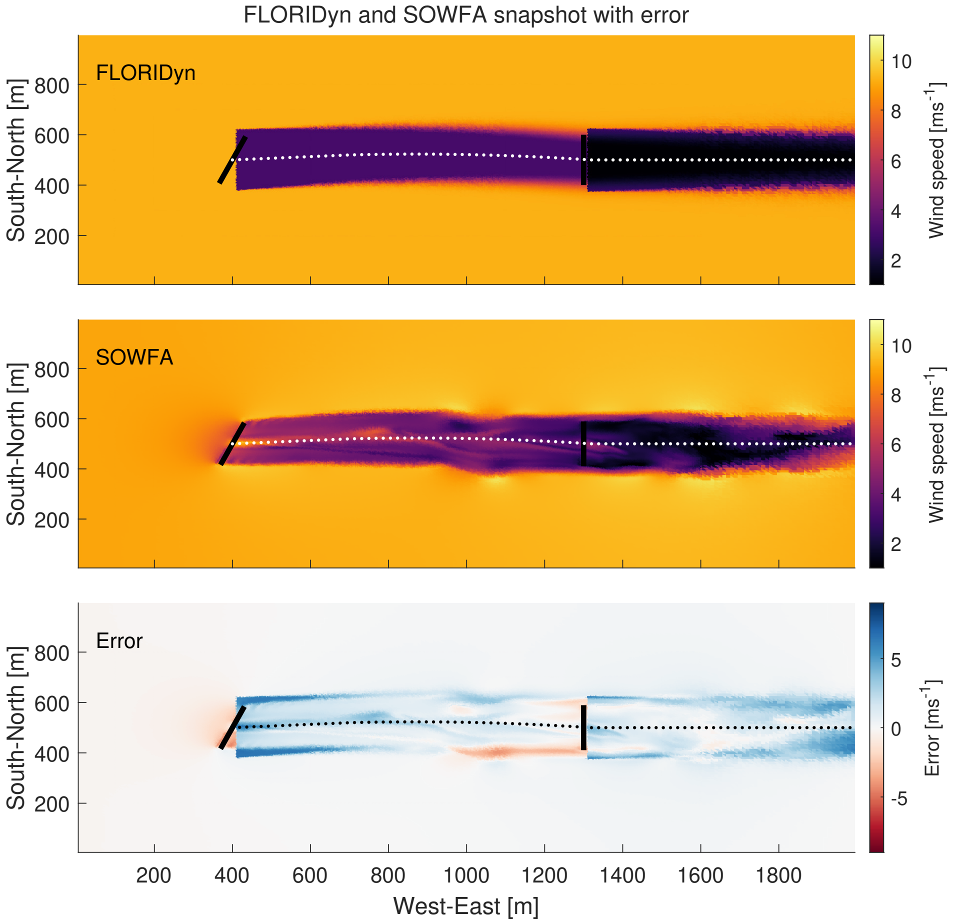

Figure 2-10: FLORIDyn, SOWFA and their error plot of a 2 turbine simulation with $20\,\mathrm{deg}$ yaw step of $0.3\,\mathrm{deg\,s^{-1}}$ by T0 at $300\,\mathrm{s}$. Snapshots taken at $400\,\mathrm{s}$. The FLORIDyn center line of T0 is visualised in all plots.

the wake deficit to changes based on conditions at the rotor.

A study by E. Machefaux et al. tried to empirically model the advection velocity of a single wake using lidar-based measurements ([25]). Two-dimensional lidar measurements were used to create a vertical slice through the wake at four different downstream distances: 80m, 120m, 160m, and 200m. From these measurements, the lateral center position of the wake could be tracked at these distances. Time-shifting these results showed a strong correlation of the patterns, only being scaled in amplitude. Using the time shifts between pairs of cross-sections, the advection velocity was estimated.
Using these findings, results from the Hills vortex theory and CFD simulations, an empirical relationship was concluded. The expression for the advection velocity of a Hill's spherical vortex was obtained as:

$$\frac{U_a}{U_\infty} = 1 - 0.4\frac{\Delta u}{U_\infty} \tag{2-11}$$

In a fixed coordinate system, U_a is defined as the advection velocity at a certain downwind position, U_∞ the free-stream velocity, and Δu the maximum wake deficit at that downwind position. This relation is thus able to describe the axial wake velocity.

Chapter 3

Proposed method and theory: including wake advection in FLORIDyn

3-1 Center line extraction

For yaw-based wake control, simulating the right wake deflection is very important. To properly model the deflection across downwind distances, the center line of the wake needs to be identified. Multiple studies have used the estimation of high-fidelity wake center lines as validation for low-fidelity center line descriptions. For instance in the study from Machefaux, where the center position at four downwind distances was used to estimate the wake advection velocity. Figure 3-1 shows the result of the center line extraction from wind tunnel measurements. This result is used to validate the potential core center line description in the Gaussian FLORIS description [2]. The following section explains how the center line can be extracted using a weighted geometric center approach.

3-1-1 Weighted geometric center approach

One method of extracting this center line from a high-fidelity flow field, is the use of the Weighted Geometric-Center Approach as described by:

$$y_{wake} = \frac{\sum_i u_i y_i}{\sum_i u_i}, \quad \forall u_i < u_{thresh} \tag{3-1}$$

where y_{wake} is the center of a crosswind wake slice, u_i is the instantaneous sampled velocity with mean shear removed, and u_{thresh} is a user-specified threshold value. The vertical position can be determined analogously by replacing y with z [33]. However, in this approach, high velocities at the wake boundary have a higher weight than low velocities at the wakes center. This results in sensitivity to the wake boundary defined by $u_i < u_{thresh}$. To avoid this, the

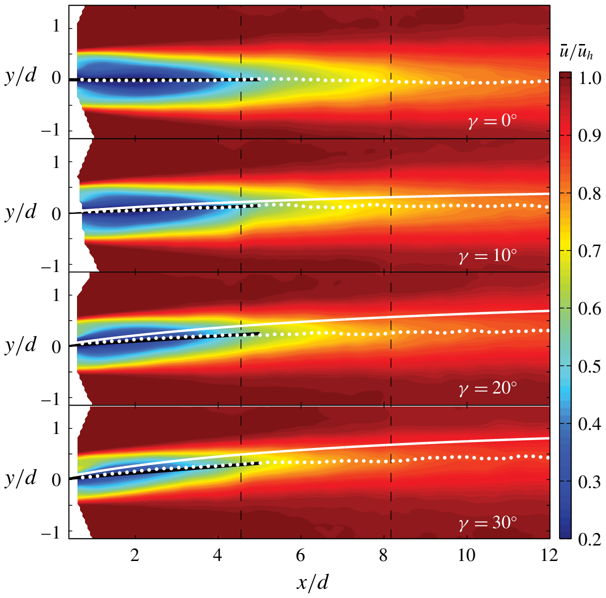

Figure 3-1: Contours of the normalized mean stream-wise velocity in the horizontal plane at hub height downwind of a turbine for different yaw angles. White dots and white lines represent the wake-center trajectory in the horizontal plane obtained from the wind tunnel measurements and theory (Jiménez et al., 2010), respectively. Black lines show the initial wake deflection predicted by (Coleman et al., 1945) [2].

following relation is derived, which penalises the wake boundary and gives the highest weights to locations with low velocities in the wake:

$$y_{wake} = \frac{\sum_i (u_{thresh} - u_i) y_i}{\sum_i (u_{thresh} - u_i)}, \quad \forall u_i < u_{thresh} \tag{3-2}$$

3-2 Estimation of a dynamic yaw description

To improve the performance of parametric models, their parameters need to be estimated to better align them with high-fidelity data. First, two different methods of parameter estimation in FLORIS are introduced. After this, a nonlinear least squares minimisation problem is formulated to identify a dynamic yaw description from center line data extracted from high-fidelity simulations.

3-2-1 Parameter estimation in FLORIS

In the original FLORIS model, the wake deflection, expansion, and decay was tuned 'manually' to fit the SOWFA power data of two different two-turbine cases. In one case the γ of the upstream turbine was varied, and in the other the crosswind position of the downwind turbine. Validation was performed by comparing the wake velocity profiles of a single turbine at 7D for different γ-angles [19].

Another method of parameter estimation is performed by Doekemeijer, Van der Hoek and

Van Wingerden [15]. It is done through minimizing the root-mean-square error (RMSE) of time-averaged flow fields from SOWFA,$U^{\text{SOWFA}} \in \mathbb{R}^{N_\text{u}}$, and from FLORIS, $U^{\text{FLORIS}} \in \mathbb{R}^{N_\text{u}}$:

$$J_{\text{fit}}(\Omega) = \frac{1}{N_\text{u}} \sum_{i=1}^{N_\text{u}} w_i \left(U_i^{\text{FLORIS}}(\Omega) - U_i^{\text{SOWFA}} \right)^2 \tag{3-3}$$

where N_u samples are taken from wake profiles at four different downwind positions. Higher weights were included at 5 and 7D. These wake profiles were measured for wind speeds of 7.0 and 8.2 m/s for seven different yaw set points, ranging from -30 to $30\,\text{deg}$.

3-2-2 Dynamic yaw estimation using a least squares problem

In FLORIDyn, the deflection function models the center line in the wake coordinate system. One way to describe this dynamically after a γ-step, is using a more dynamic γ as an input to the function. From the SOWFA center line, we can use parameter estimation to estimate a γ that is translated to this SOWFA deflection using the FLORIS deflection function. To do this, the following minimisation problem is derived, which minimises the RMSE between the extracted SOWFA and FLORIDyn deflection at the x coordinate x_1 in the wake coordinate system:

$$\min_{\gamma} \left(\delta_{SOWFA,x_1} - \delta(\gamma, x_1) \right)^2 \tag{3-4}$$

Where δ_{SOWFA,x_1} is the SOWFA deflection at x_1. The minimisation problem is solved for all locations of x_1 for which a deflection is extracted from the SOWFA data, and for all identified center lines over time. This nonlinear least squares problem is solved using the Levenberg-Marquardt algorithm. For the deflection, the Gaussian FLORIS model is used, as it is in the FLORIDyn Center Line model:

$$\begin{aligned} \delta(\gamma, x_1) = &\, \theta_{\text{pc}} \max\left(x_1, x_\text{c}\right) + \\ & \frac{1}{2}\left(\text{sign}\left(x_1 - x_\text{c}\right) + 1\right) \frac{\theta_{\text{pc}}}{14.7} \sqrt{\frac{\cos\gamma}{k_y k_z C_\text{T}}} \left(2.9 + 1.3\sqrt{1 - C_\text{T}} - C_\text{T}\right) \times \\ & \ln\left[\frac{\left(1.6 + \sqrt{C_\text{T}}\right)\left(1.6\sqrt{\frac{8\sigma_y\sigma_z}{\text{D}^2\cos\gamma}} - \sqrt{C_\text{T}}\right)}{\left(1.6 - \sqrt{C_\text{T}}\right)\left(1.6\sqrt{\frac{8\sigma_y\sigma_z}{\text{D}^2\cos\gamma}} + \sqrt{C_\text{T}}\right)} \right] \text{D} \end{aligned} \tag{3-5}$$

With the following functions for the potential core length x_c and potential core angle θ_{pc}:

$$x_\text{c} = \frac{\cos\gamma\left(1 + \sqrt{1 - C_\text{T}}\right)}{\sqrt{2}\left(\alpha^* I + \beta^*\left(1 - \sqrt{1 - C_\text{T}}\right)\right)} \text{D} \tag{3-6}$$

With the constants $\alpha^* = 2.32$ and $\beta^* = 0.154$

$$\theta_{\text{pc}} = \frac{0.3\gamma}{\cos\gamma}\left(1 - \sqrt{1 - C_\text{T}\cos\gamma}\right) \tag{3-7}$$

Furthermore, the Thrust Coefficient C_T is defined as:

$$C_\mathrm{T} = -\left(-2\mathrm{a}+1\right)^2 + 1 \tag{3-8}$$

And the standard deviations for the Gaussian wake expansion σ_y and σ_z:

$$\sigma_y = \max\left(x_1 - x_\mathrm{c}, 0\right) k_y + \min\left(\frac{x_1}{x_\mathrm{c}}, 1\right) \frac{\mathrm{D}}{\sqrt{8}} \cos\gamma \tag{3-9}$$

$$\sigma_z = \max\left(x_1 - x_\mathrm{c}, 0\right) k_z + \min\left(\frac{x_1}{x_\mathrm{c}}, 1\right) \frac{\mathrm{D}}{\sqrt{8}} \tag{3-10}$$

And finally the constants $k_a = 0.38371$ and $k_b = 0.003678$, Turbulence Intensity $I = 0.00$ and axial induction $a = 0.33$. The other constants were derived from these constants as:

$$k_y = k_z = k_a I + k_b \tag{3-11}$$

Note that I is set to zero because turbulence free SOWFA simulations are used to extract the center line.

3-3 System identification

3-3-1 MOESP

The Multivariable Output Error State sPace (MOESP) framework is a subspace model identification method and introduced in 1992 by Verhaegen and Dewilde [38] [39]. Subspace identification methods are based on robust linear-algebra problems and tools. These tools are RQ decomposition, Singular Value Decomposition (SVD) and the solution of a linear least squares problem [40]. RQ decomposition decomposes a matrix in both a upper triangular (R) and orthogonal (Q) matrix. In subspace identification, the data equation is used to relate input and output matrices to matrices containing system matrices.

The data equation The data equation is as follows:

$$Y_{0,s,N} = \mathcal{O}_s X_{0,N} + \mathcal{T}_s U_{0,s,N} \tag{3-12}$$

With the output data matrix $Y_{0,s,N}$ and input matrix $U_{0,s,N}$:

$$Y_{0,s,N} = \begin{bmatrix} y(0) & y(1) & \cdots & y(N-1) \\ y(1) & y(2) & \cdots & y(N) \\ \vdots & \vdots & \ddots & \vdots \\ y(s-1) & y(s) & \cdots & y(N+s-2) \end{bmatrix} \tag{3-13}$$

$$U_{0,s,N} = \begin{bmatrix} u(0) & u(1) & \cdots & u(N-1) \\ u(1) & u(2) & \cdots & u(N) \\ \vdots & \vdots & \ddots & \vdots \\ u(s-1) & u(s) & & u(N+s-2) \end{bmatrix} \tag{3-14}$$

The matrices constructed of the system matrices are the extended observability matrix $\mathcal{O}_s$ and the Toeplitz matrix $\mathcal{T}_s$:

$$\mathcal{O}_s = \begin{bmatrix} C \\ CA \\ CA^2 \\ \vdots \\ CA^{s-1} \end{bmatrix} \tag{3-15}$$

$$\mathcal{T}_s = \begin{bmatrix} D & 0 & 0 & \cdots & 0 \\ CB & D & 0 & \cdots & 0 \\ CAB & CB & D & & 0 \\ \vdots & & \ddots & \ddots & \\ CA^{s-2}B & CA^{s-3}B & \cdots & CB & D \end{bmatrix} \tag{3-16}$$

The MOESP framework MOESP stands for "Multivariable Output-Error State-sPace" and is a method to identify the state matrices and output-error from the data equation. The estimated state-space model thus becomes:

$$\begin{aligned} x(k+1) &= Ax(k) + Bu(k) \\ y(k) &= Cx(k) + Du(k) + v(k) \end{aligned} \tag{3-17}$$

where $v(k)$ is an ergodic white-noise sequence with variance $\sigma^2 I_\ell$ that is uncorrelated with $u(k)$ [40]. To identify the system matrices A and C, the column space of $\mathcal{O}_s$ has to be calculated. This is done through the following steps. First of all, an RQ decomposition is performed:

$$\begin{bmatrix} U_{0,s,N} \\ Y_{0,s,N} \end{bmatrix} = \begin{bmatrix} R_{11} & 0 \\ R_{21} & R_{22} \end{bmatrix} \begin{bmatrix} Q_1 \\ Q_2 \end{bmatrix} \tag{3-18}$$

After which the following SVD is performed:

$$\lim_{N\to\infty} \frac{1}{\sqrt{N}} R_{22} = \begin{bmatrix} U_n & U_2 \end{bmatrix} \begin{bmatrix} \sqrt{\sum_n^2 + \sigma^2 I_n} & 0 \\ 0 & \sigma I_{s\ell-n} \end{bmatrix} \begin{bmatrix} V_1^T \\ V_2^T \end{bmatrix} \tag{3-19}$$

The following relation now holds:

$$\text{range}\,(U_n) = \text{range}\,(\mathcal{O}_s) \tag{3-20}$$

With the column space of $\mathcal{O}_s$ derived, estimates for the system matrices can be derived. First, the C can be determined up to an unknown similarity transformation T:

$$U_n = \mathcal{O}_s T = \begin{bmatrix} CT \\ CT\left(T^{-1}AT\right) \\ \vdots \\ CT\left(T^{-1}AT\right)^{s-1} \end{bmatrix} = \begin{bmatrix} C_T \\ C_T A_T \\ \vdots \\ C_T A_T^{s-1} \end{bmatrix} \tag{3-21}$$

Where $C_T = U_n(1 : l, :)$. Through the following overdetermined equation, A_T can be computed:

$$U_n(1 : (s-1)\ell, :)A_T = U_n(\ell + 1 : s\ell, :) \tag{3-22}$$

Finally the matrices B_T and D_T are computed by the following least-squares problem:

$$\min_{\theta} \frac{1}{N} \sum_{k=0}^{N-1} \left\| y(k) - \phi(k)^{\mathrm{T}}\theta \right\|_2^2 \tag{3-23}$$

where

$$\phi(k)^{\mathrm{T}} = \left[\widehat{C}_T \widehat{A}_T^k \quad \left(\sum_{\tau=0}^{k-1} u(\tau)^{\mathrm{T}} \otimes \widehat{C}_T \widehat{A}_T^{k-\tau-1} \right) \quad \left(u(k)^{\mathrm{T}} \otimes I_\ell \right) \right] \tag{3-24}$$

$$\theta = \begin{bmatrix} x_T(0) \\ \operatorname{vec}\left(B_T\right) \\ \operatorname{vec}\left(D_T\right) \end{bmatrix} \tag{3-25}$$

3-3-2 DMDc

Dynamic Dynamic Mode Decomposition with Control (DMDc) is based upon Dynamic Mode Decomposition, or Dynamic Mode Decomposition (DMD). DMD finds its origin in the field of fluid dynamics where it was first used to extract dynamics from flow fields. It is a data-driven method and can be used to give insight in the underlying physical mechanisms from snapshot data or to acquire a Reduced Order Model (ROM) from large scale problems [34] [24] [31]. Furthermore, it is often applied to data from high-dimensional nonlinear systems [31].

Measurements from a dynamical system are assumed to be related by a linear operator, $\mathbf{A}$. With measurements $\mathbf{x}_k$ and $\mathbf{x}_{k+1}$, where k is the temporal iteration, the dynamical system can be approximated by:

$$\mathbf{x}_{k+1} \approx \mathbf{A}\mathbf{x}_k \tag{3-26}$$

where $\mathbf{x} \in \mathbb{R}^n$ and $\mathbf{A} \in \mathbb{R}^{n \times n}$. With DMD, we are trying to estimate $\mathbf{A}$ for the entire data set. Because DMD is often used in fluid dynamics or with snapshot data, data at a single time instance is translated to a single vector $\mathbf{x}_k$. In literature this is still denoted as a single snapshot [31]. The total sequence of snapshots can be transformed to the snapshot matrix $\mathbf{X}$ and its time-shifted matrix $\mathbf{X}'$, with m the total number of snapshots:

$$\mathbf{X} = \begin{bmatrix} | & | & & | \\ \mathbf{x}_1 & \mathbf{x}_2 & \dots & \mathbf{x}_{m-1} \\ | & | & & | \end{bmatrix} \qquad \mathbf{X}' = \begin{bmatrix} | & | & & | \\ \mathbf{x}_2 & \mathbf{x}_3 & \dots & \mathbf{x}_m \\ | & | & & | \end{bmatrix} \tag{3-27}$$

The objective of DMD is to approximate A for the entire process, described by combining equation 3-26 and 3-27 into a single matrix form:

$$\mathbf{X}' \approx \mathbf{A}\mathbf{X} \tag{3-28}$$

DMD algorithm With DMD we can find the dynamic modes and eigenvalues of A. Equation 3-28 can be translated to:

$$\mathbf{A} = \mathbf{X}'\mathbf{X}^{\dagger} \tag{3-29}$$

Where † is the Moore-Penrose pseudoinverse. The pseudoinverse can be calculated using the SVD of $\mathbf{X}$:

$$\mathbf{X} = \mathbf{U}\mathbf{\Sigma}\mathbf{V}^* = \begin{bmatrix} \tilde{\mathbf{U}} & \tilde{\mathbf{U}}_{\text{rem}} \end{bmatrix} \begin{bmatrix} \tilde{\mathbf{\Sigma}} & 0 \\ 0 & \mathbf{\Sigma}_{\text{rem}} \end{bmatrix} \begin{bmatrix} \tilde{\mathbf{V}}^* \\ \tilde{\mathbf{V}}^*_{\text{rem}} \end{bmatrix} \tag{3-30}$$

$$\approx \tilde{\mathbf{U}}\tilde{\mathbf{\Sigma}}\tilde{\mathbf{V}}^* \tag{3-31}$$

Where $\mathbf{U} \in \mathbb{R}^{n\times n}, \mathbf{\Sigma} \in \mathbb{R}^{n\times m-1}, \tilde{\mathbf{V}}^* \in \mathbb{R}^{m-1\times m-1}, \tilde{\mathbf{U}} \in \mathbb{R}^{n\times r}, \tilde{\mathbf{\Sigma}} \in \mathbb{R}^{r\times r}, \tilde{\mathbf{V}}^* \in \mathbb{R}^{r\times m-1}$, $_{rem}$ the remaining $m-1-r$ singular values, and * the complex conjugate transpose [31]. By choosing a truncation value r, the dimension of $\mathbf{X}$ can be reduced by equation 3-3-2. Because $\tilde{\mathbf{\Sigma}}$ is square, equation 3-3-2 can be used to obtain a reduced order pseudoinverse of $\mathbf{X}$. Substituting the pseudoinverse of the SVD of $\mathbf{X}$ (3-3-2) into equation 3-29 results in:

$$\mathbf{A} \approx \bar{\mathbf{A}} = \mathbf{X}'\tilde{\mathbf{V}}\tilde{\mathbf{\Sigma}}^{-1}\tilde{\mathbf{U}}^* \tag{3-32}$$

Where $\bar{\mathbf{A}} \in \mathbb{R}^{n\times n}$ approximates A, resulting in the dynamic model:

$$\mathbf{x}_{k+1} = \bar{\mathbf{A}}\mathbf{x}_k \tag{3-33}$$

This model can be reduced in order by a transformation matrix, which is already computed in equation 3-3-2, and can be derived as follows:

$$\begin{aligned} \tilde{\mathbf{x}}_{k+1} &= \tilde{\mathbf{U}}^*\bar{\mathbf{A}}\tilde{\mathbf{U}}\tilde{\mathbf{x}}_k \\ &= \tilde{\mathbf{U}}^*\mathbf{X}'\tilde{\mathbf{V}}\tilde{\mathbf{\Sigma}}^{-1}\tilde{\mathbf{x}}_k \\ &= \tilde{\mathbf{A}}\tilde{\mathbf{x}}_k. \end{aligned} \tag{3-34}$$

Resulting in the following Reduced Order Model (ROM):

$$\tilde{\mathbf{A}} = \tilde{\mathbf{U}}^*\mathbf{X}'\tilde{\mathbf{V}}\tilde{\mathbf{\Sigma}}^{-1} \tag{3-35}$$

Where $\mathbf{A} \in \mathbb{R}^{r\times r}$ with $r \ll n$. This increases the computational efficiency of the eigendecomposition of $\tilde{\mathbf{U}}$, which is given by:

$$\tilde{\mathbf{A}}\mathbf{W} = \mathbf{W}\Lambda \tag{3-36}$$

The eigenvalues and vector can be analysed for system properties like the dynamic modes and resonance frequencies.

DMDc The Dynamic Mode Decomposition with Control was introduced by Proctor et all in 2016 [31]. Where DMD enables us to analyse the internal system dynamics, DMDc can quantify the effect of control inputs on the system. DMDc includes the effect of current control inputs $\mathbf{u}_k$ on $\mathbf{x}_{k+1}$, resulting in the new relation:

$$\mathbf{x}_{k+1} \approx \mathbf{A}\mathbf{x}_k + \mathbf{B}\mathbf{u}_k \tag{3-37}$$

where $\mathbf{x}_j \in \mathbb{R}^n, \mathbf{u}_j \in \mathbb{R}^l, \mathbf{A} \in \mathbb{R}^{n\times n}$, and $\mathbf{B} \in \mathbb{R}^{n\times l}$. The snapshot matrices $\mathbf{X}$ and $\mathbf{X}'$ remain the same as in DMD, however, the control input snapshot matrix is added:

$$\Upsilon = \begin{bmatrix} | & | & & | \\ \mathbf{u}_1 & \mathbf{u}_2 & \dots & \mathbf{u}_{m-1} \\ | & | & & | \end{bmatrix} \tag{3-38}$$

to obtain the new matrix form system relation:

$$\mathbf{X}' \approx \mathbf{A}\mathbf{X} + \mathbf{B}\Upsilon \tag{3-39}$$

The data and input matrices can be concatenated, where the relation can be rewritten as:

$$\mathbf{X}' \approx \mathbf{G}\boldsymbol{\Omega} \tag{3-40}$$

where $\mathbf{G} = \begin{bmatrix} \mathbf{A} & \mathbf{B} \end{bmatrix}$ and $\boldsymbol{\Omega} = \begin{bmatrix} \mathbf{X} \\ \boldsymbol{\Upsilon} \end{bmatrix}$

This can be rewritten to obtain a relation for $\mathbf{A}$ and $\mathbf{B}$:

$$\mathbf{G} = \mathbf{X}'\Omega^\dagger \tag{3-41}$$

$$\begin{bmatrix} \mathbf{A} & \mathbf{B} \end{bmatrix} = \mathbf{X}' \begin{bmatrix} \mathbf{X} \\ \boldsymbol{\Upsilon} \end{bmatrix}^\dagger \tag{3-42}$$

As in DMD, the pseudoinverse is solved using an SVD:

$$\boldsymbol{\Omega} = \mathbf{U}\boldsymbol{\Sigma}\mathbf{V}^* \approx \tilde{\mathbf{U}}\tilde{\boldsymbol{\Sigma}}\tilde{\mathbf{V}}^* \tag{3-43}$$

with the truncation value p. Furthermore, p should be larger than the truncation value r of the SVD of $\mathbf{X}$.

After breaking $\tilde{\mathbf{U}}$ into $\tilde{\mathbf{U}}_1 \in \mathbb{R}^{n\times p}, \tilde{\mathbf{U}}_2 \in \mathbb{R}^{l\times p}$, and $\tilde{\mathbf{U}}^* = \begin{bmatrix} \tilde{\mathbf{U}}_1^* & \tilde{\mathbf{U}}_2^* \end{bmatrix}$, The system matrices can be approximated by:

$$\begin{aligned} &\begin{bmatrix} \mathbf{A}, & \mathbf{B} \end{bmatrix} \approx \begin{bmatrix} \bar{\mathbf{A}}, & \bar{\mathbf{B}} \end{bmatrix} \\ &\approx \left[\mathbf{X}'\tilde{\mathbf{V}}\tilde{\boldsymbol{\Sigma}}^{-1}\tilde{\mathbf{U}}_1^*, \quad \mathbf{X}'\tilde{\mathbf{V}}\tilde{\boldsymbol{\Sigma}}^{-1}\tilde{\mathbf{U}}_2^*\right] \end{aligned} \tag{3-44}$$

A SVD of $\mathbf{X}' = \hat{\mathbf{U}}\hat{\boldsymbol{\Sigma}}\hat{\mathbf{V}}^*$ is used to find a reduced-order output space. Here, the truncation value is r and $\hat{\mathbf{U}} \in \mathbb{R}^{n\times r}, \hat{\boldsymbol{\Sigma}} \in \mathbb{R}^{r\times r}$, and $\hat{\mathbf{V}}^* \in \mathbb{R}^{r\times m-1}$. Using this transformation matrix $\hat{\mathbf{U}}$, $\mathbf{A}$ and $\mathbf{B}$ can be approximated:

$$\tilde{\mathbf{A}} = \hat{\mathbf{U}}^*\bar{\mathbf{A}}\hat{\mathbf{U}} = \hat{\mathbf{U}}^*\mathbf{X}'\tilde{\mathbf{V}}\tilde{\boldsymbol{\Sigma}}^{-1}\tilde{\mathbf{U}}_1^*\hat{\mathbf{U}} \tag{3-45}$$

$$\tilde{\mathbf{B}} = \hat{\mathbf{U}}^{*}\bar{\mathbf{B}} = \hat{\mathbf{U}}^{*}\mathbf{X}'\tilde{\mathbf{V}}\tilde{\mathbf{\Sigma}}^{-1}\tilde{\mathbf{U}}_2^{*} \tag{3-46}$$

The ROM finally becomes:

$$\tilde{\mathbf{x}}_{k+1} = \tilde{\mathbf{A}}\tilde{\mathbf{x}}_k + \tilde{\mathbf{B}}\mathbf{u}_k \tag{3-47}$$

Where we can again do the eigenvalue decomposition $\tilde{\mathbf{A}}\mathbf{W} = \mathbf{W}\mathbf{\Lambda}$. To translate these eigenvectors to dynamic modes of $\mathbf{A}$, the following transformation is required:

$$\phi = \mathbf{X}'\tilde{\mathbf{V}}\tilde{\mathbf{\Sigma}}^{-1}\tilde{\mathbf{U}}_1^{*}\hat{\mathbf{U}}\mathbf{w} \tag{3-48}$$

Finally, the ROM states can be translated back to the original states using the transformation matrix $\hat{\mathbf{U}}$:

$$\mathbf{x}_k = \hat{\mathbf{U}}\tilde{\mathbf{x}}_k \tag{3-49}$$

3-3-3 Comparing MOESP and DMDc

Both the MOESP and DMDc algorithm consist of solving a regression function, equations 3-12 and 3-39 respectively. Furthermore, both models perform a model reduction by taking a truncated part of unitary rotation matrix U from the SVD. In addition, the MOESP algorithm perform this SVD on a part of triangular matrix from the RQ decomposition. Finally, both methods perform parameter estimation to identify the system matrices. However, no least squares problem has to be solved in the DMDc algorithm, compared to MOESP. This results in DMDc being more computational efficient than MOESP.

MOESP is a black-box model identification method, identifying the system matrices from input-output data. In comparison, the DMDc framework requires full-state measurements. This results in the required least squares problem in MOESP, which is not present in DMDc. Another difference is observed in the composed data, input and snapshot matrices. MOESP requires shift-stacking of the data, where every column in the matrices is a time shift of the previous column including a new measurement. In DMDc, shift-stacking is not required. Due to the typically large number of observables, there is little risk of column-rank deficiency [31]. Finally, DMDc and its variants are proven to be capable of identifying high-dimensional, complex and nonlinear systems like disease modelling, fluid dynamics and ROM wind farm modelling [32] [24] [1].

3-3-4 Identification of a dynamic yaw system

The goal of the system identification is to estimate a system that translates the turbine yaw γ to a dynamic yaw γ_{Dyn}. For training data of the identification, we use the dynamic yaw obtained by the parameter estimation from section 3-2-2, which was estimated from the extracted SOWFA center line. To implement this into the MOESP framework, the dynamic yaw is used to obtain the output data matrix $Y_{0,s,N}$ and the turbine yaw for the input matrix $U_{0,s,N}$. This can be performed in multiple ways. Either one Single-Input Multiple-Output (SIMO) system can be identified, or multiple Single-Input Single-Output (SISO) systems. In case multiple SISO systems are identified, the FLORIDyn yaw should also be estimated at downwind distances where the yaw is simulated by the systems. This is required to minimize the delay between the input and output.

In the DMDc framework, γ_{Dyn} is used for the snapshot matrix $\mathbf{X}$ and γ for the input matrix $\boldsymbol{\Upsilon}$. Because DMDc is able to model complex and high dimensional systems and tries to capture the inherent dynamics between the states, only a single model is used to identify the center line states from a single input. The following Section will give an overview of the proposed methodology, which includes the center line extraction, parameter estimation and system identification.

3-4 Overview of the methodology

The overall goal of the methodology is to identify a dynamic system that is implementable in FLORIDyn. The result is a FLORIDyn model that includes center line advection behaviour, designed to decrease the error between the FLORIDyn and extracted SOWFA center line. The dynamic system uses the turbine yaw as an input, and outputs the dynamic yaw for all downwind distances used in the identification process. The overview is visualised in Figure 3-2 as a block diagram.

First of all, single turbine FLORIDyn and SOWFA simulations including a yaw step are performed. From the obtained SOWFA flow field, the center line is extracted using the weighted geometric center approach from section 3-1-1. The output of the weighted geometric center approach is the SOWFA center line over time. Using simulations with a 270 deg inflow angle, the SOWFA center line deflection can directly be extracted from the center line y-coordinates. Thereafter, using the Gaussian wake description and a nonlinear least squares problem from section 3-2-2, we can estimate the required yaw inputs in the FLORIS model that would result in the extracted SOWFA center line deflections. This dynamic yaw is depending on its downwind distance and is defined for the same downwind distances as the center line. The dynamic yaw, together with the turbine yaw (SIMO MOESP or DMDc identification) or FLORIDyn yaw over downwind distance (multiple SISO MOESP identification) can be used to estimate the dynamic yaw system(s), as described in section 3-3-4. The implementation of the dynamic system is described in the following section

3-5 Implementation of the dynamic system in FLORIDyn

The dynamic yaw systems are able to simulate the γ_{Dyn} required to obtain δ_{Dyn} at certain downwind distances from the turbine. This set of downwind locations, x_{nodes}, are the constant downwind locations used to estimate γ_{Dyn} from the extracted SOWFA center line deflection, δ_{SOWFA} , over time. However, the OPs traveling downwind in FLORIDyn do not have a set downwind location. To implement the γ_{Dyn} in the FLORIDyn Center Line (FLORIDyn CL) model, a 1-D interpolation is used to find γ_{Dyn} at the OP locations $x_{\mathrm{OP},1,\mathrm{x}}$. A piecewise cubic interpolation is used to preserve a smooth center line when the distance between x_{nodes} are relatively large. However, the dynamic yaw system is identified for a finite downwind distance. To obtain a γ for OPs located beyond the furthest x_{nodes}, the γ_{Dyn} of the last OP in the range of x_{nodes} , and every OP onward, are shifted one step, together with their OP. This is in line with the original turbine state changes with corresponding OPs.

The γ_{Dyn} is implemented at two places in the FLORIDyn CL model. First, it is used as the γ input to the FLORIS δ-function used to calculate the FLORIDyn crosswind positions

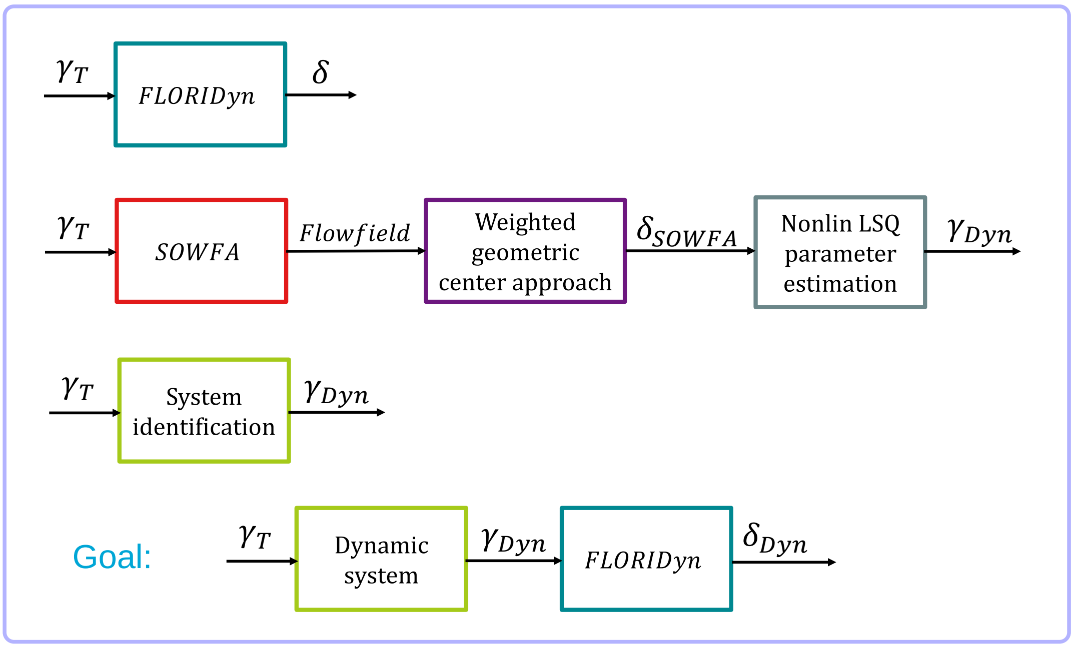

Figure 3-2: Overview of the methodology

of the OPs. The second location is at the TWF, required to calculate the influence of the closest OPs on the flow field. In the TWF, FLORIS is used to obtain the Gaussian wake parameters in the "getVars" function. In this calculation, γ_{Dyn} is only used to obtain θ and δ. The regular γ is used to calculate x_0 and σ_y to maintain a more constant wake width at the locations with large dynamic deflections.
Finally, the way the OPs are interpolated to calculate the effective wind speed in the wind farm is altered. Due to the implementation of the γ_{Dyn}model, the center line experienced steep changes in δ_{Dyn}. This resulted in overlapping wake sections due to the OP interpolation used in the heterogeneous FLORIDyn model. Therefore, the interpolation was changed to only take the closest OP into account based on the downwind component. Note that this results in the model only working with a 270 deg inflow.

Chapter 4

Results of center line extraction and dynamic yaw estimation

In this chapter we show the results from the center line extraction (Section 4-1) and the results from the dynamic SOWFA yaw parameter estimation (Section 4-2). For the center line extraction of Section 4-1, the weighted geometric center approach is used as described in Section 3-1-1. Furthermore, Section 4-1 defines the used SOWFA simulation, shows the flow fields including center lines and defines a filter used in pre-filtering the data. Finally, the parameter estimation from Section 3-2-2 is performed by solving the least-squares problem defined in Section 3-2-2.

4-1 Center line extraction

First, the performed SOWFA simulation which snapshots are used in the center line extraction is stated in Section 4-1-1. This is followed by examples of snapshots with the extracted center line in Section 4-1-2. Section 4-1-3 shows the low-pass filtered center line snapshot, a filter is applied to reduce the center line complexity. Finally, the center line deflection over time at different downwind distances is visualised in Section 4-1-4 to give a different view on the data.

4-1-1 SOWFA simulation case

The flow field data used for the center line extraction is a horizontal slice at hub height acquired every 2 s from a SOWFA simulation with a time-step of 0.2 s. The simulation uses a $4\,\mathrm{km} \times 1\,\mathrm{km} \times 0.6\,\mathrm{km}$ domain with base cells of $50\,\mathrm{m} \times 50\,\mathrm{m} \times 50\,\mathrm{m}$. The turbine is located at $(500, 500)\,\mathrm{m}$ from the domain origin. Three rectangular prism refinements are applied, with origins located at $(200, 200, 0)$m, $(220, 220, 0)$m and $(230, 230, 0)$m with length, width and height of $(2300, 600, 460)$m, $(2200, 560, 420)$m, and $(2000, 500, 400)$m respectively. Every refinement halves the cell dimensions in the x,y and z direction. A horizontal slice of the

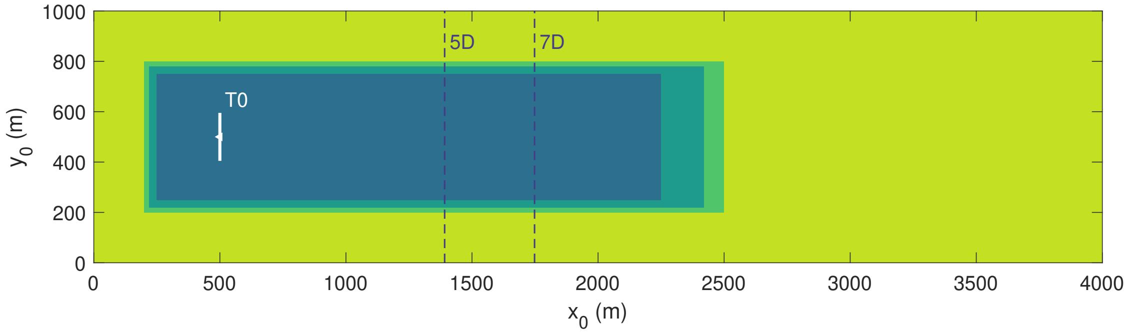

Figure 4-1: The flow field including refinements of the 1T SOWFA simulation. The unrefined (light green) flow field has a base cell size of 50 m × 50 m.

Table 4-1: 1T case SOWFA numerical properties

Turbine model	ALM
Base cells	$50\,\mathrm{m} \times 50\,\mathrm{m} \times 50\,\mathrm{m}$
First refinement	$25\,\mathrm{m} \times 25\,\mathrm{m} \times 25\,\mathrm{m}$
Second refinement	$12.5\,\mathrm{m} \times 12.5,\mathrm{m} \times 12.5\,\mathrm{m}$
Third refinement	$6.25\,\mathrm{m} \times 6.25\,\mathrm{m} \times 6.25\,\mathrm{m}$
Simulation time-step	0.2 s

domain with refinements is visualised in Figure 4-1. The numerical properties are listed in Table 4-1.

The SOWFA simulation is performed for two cases: a 10 deg and a 20 deg yaw-step, both with a rotation speed of $0.3\,\mathrm{deg\,s^{-1}}$. The wind has a constant inflow-angle of 270 ° and a speed of $9.2\,\mathrm{m\,s^{-1}}$. Furthermore, the turbulence intensity is 0 %. All simulation properties are listed in Table 4-2.

4-1-2 Flow field snapshot

From the flow field snapshots at hub height acquired from the 20 deg SOWFA simulations as defined by Section 4-1-1, the center line can be extracted using the weighted geometric center approach. Furthermore, the same simulation was performed using FLORIDyn, where the center line is already defined. Figure 4-3 shows the SOWFA snapshots at 8 different time steps, with intermediate steps of 50 s. Both the SOWFA and FLORIDyn center lines at

Table 4-2: 1T case SOWFA simulation properties

Turbine location	(500, 500) m
Wind speed	$9.2\,\mathrm{m\,s^{-1}}$
Wind inflow angle	270 °
Snap shot time-step	2 s
Yaw-step	10 and 20 deg
Velocity yaw-step	$0.3\,\mathrm{deg\,s^{-1}}$
Turbulence intensity	0 %

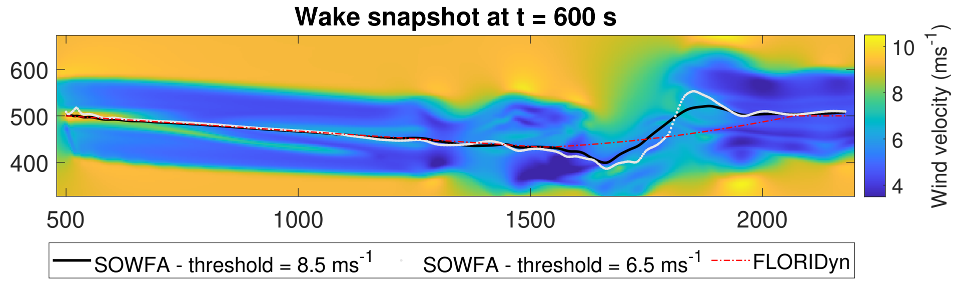

Figure 4-2: Wake snapshot at $t = 600\,\mathrm{s}$ including the extracted SOWFA center line using two different thresholds and the FLORIDyn center line.

the corresponding times are plotted over the snapshots. The snapshot is bounded on x_0 by $[481.3, 2197]\,\mathrm{m}$.
The used threshold of the weighted geometric center approach is $8.5\,\mathrm{m\,s^{-1}}$. The motivation for this is an increase in center line complexity and a lesser empirical fit to the SOWFA snapshot when smaller thresholds were applied. An example of this is given in Figure 4-2, where the center line at $t = 600\,\mathrm{s}$ is plotted for a threshold of both $8.5\,\mathrm{m\,s^{-1}}$ and $6.5\,\mathrm{m\,s^{-1}}$.

4-1-3 Pre-filtering of center line data

From the wake snapshots in Figure 4-3, we can observe that the center line complexity increases when the yaw-induced deflection travels downwind. Furthermore, the wake seems to be breaking down at further distances. This is visible when comparing the 600 s, 650 s and 700 s snapshots consecutively. In the 650 s and 700 s snapshots multiple small eddies can be observed. The center line complexity induced by these small eddies and nonuniform wind velocities in the wake can be reduced by pre-filtering the center lines. This reduction of complexity is applied to simplify the system identification and identified ROM. The applied filter is a zero-phase filtered using a Kaiser filter with cut-off frequency of 0.1Hz. The magnitude response of the filter can be found in Appendix A, Figure A-5. The result of applying the filter on the center line at $t = 600\,\mathrm{s}$ is plotted in Figure 4-4. Besides filtering the deflection of the peak by roughly $5\,\%$, only small waves in the center line are filtered, as intended.

4-1-4 Center line deflection over time

To get a more clear overview of the now acquired filtered data, the SOWFA center lines over time, we can plot the deflection over time for different downwind distances from T0. This is done for both the 10 deg and 20 degree yaw step case. The data is plotted for 20 different downwind distances, uniformly spaced over the domain. Furthermore, 2D surface plots from the deflection over downwind distance and time can be found in Appendix A: Both that of the difference between FLORIDyn and SOWFA, Figure A-1, and that of SOWFA, Figure A-2.

10 deg case The deflection over time for 20 downwind distances of the 10 deg case are plotted in figure 4-5. Note that for some distances, the influence of the flow field initialisation is still observable until $t = 300\,\mathrm{s}$. In the flow field snapshots from Section 4-1-2, an increase in complexity of the center line dynamics at increasing downwind distance was observed.

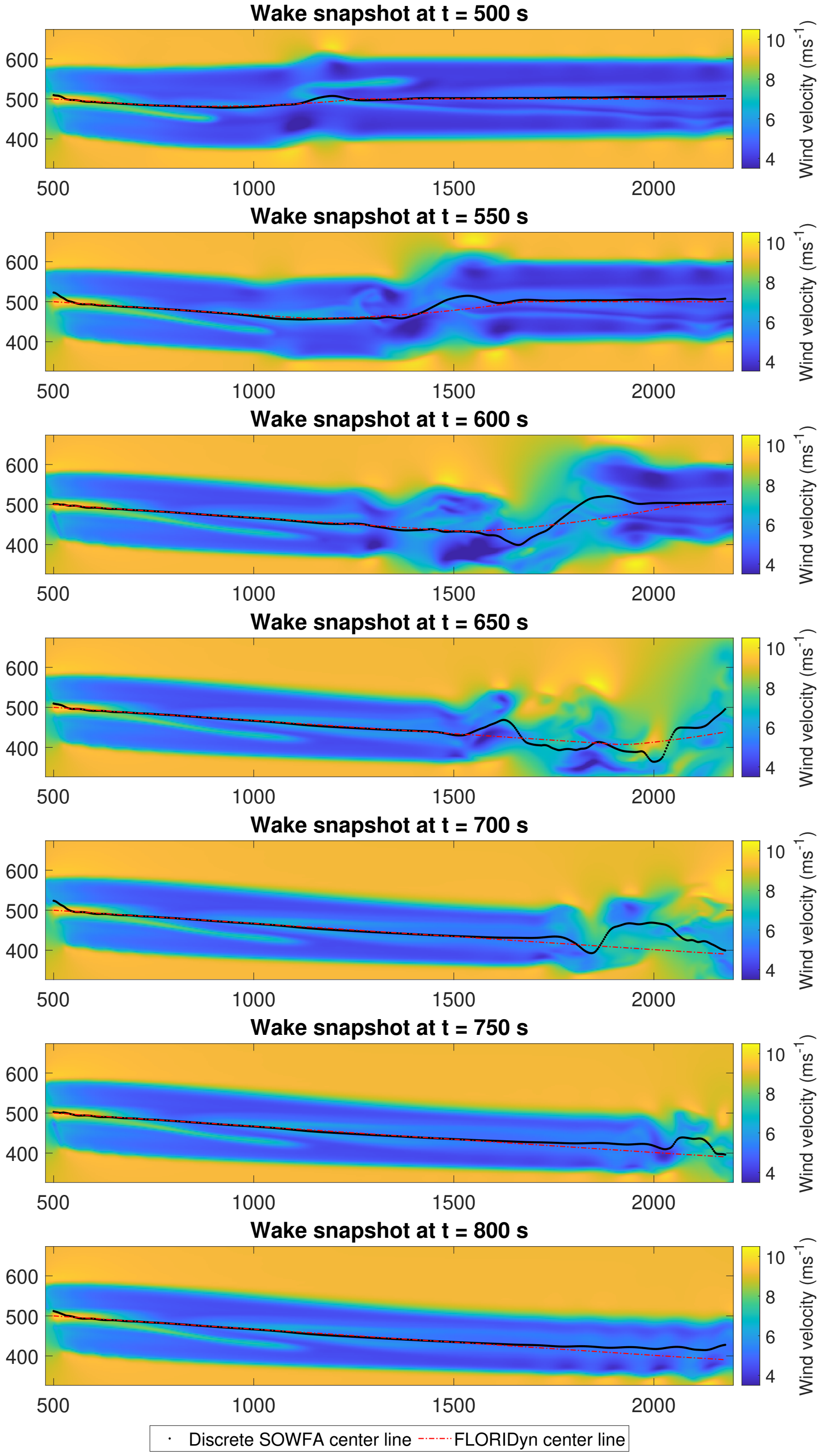

Figure 4-3: Snapshots of the 20 deg yaw step 1T simulation at different time steps. The yaw step is started at 400 s. The extracted center line is depicted in black and the FLORIDyn center line in striped red.

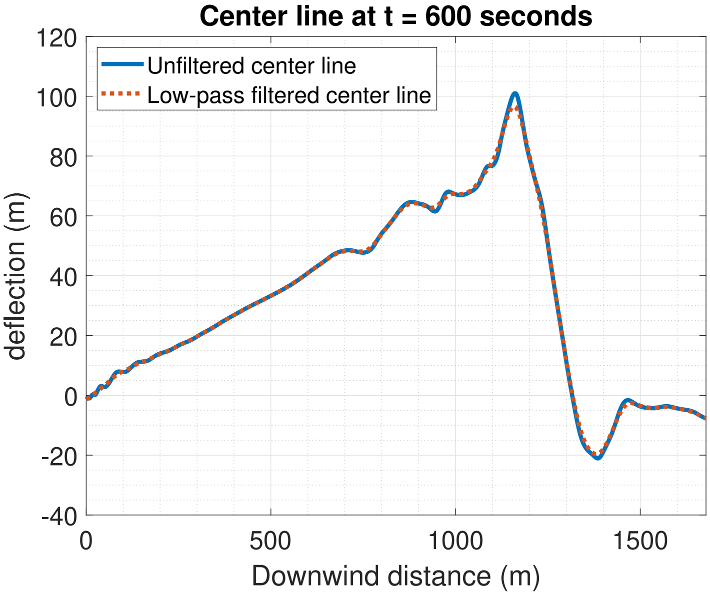

Figure 4-4: SOWFA center line deflection of 20 deg simulation at 600 s and the 1 Hz low-pass filtered center line.

This can also be observed in Figure 4-5. Where the deflection close to the turbine looks to be described by a step-response with only a single overshoot, the complexity increases more downwind. With increasing distance, an increasing undershoot before the increase in deflection occurs. Furthermore, the overshoot increases, followed by a second undershoot and overshoot.

20 deg case The same results for the 20 deg case are shown in Figure 4-6. The results are plotted for the same downwind distances as the 10 deg case. Although the deflection is higher in the 20 deg case, it shows similar under and overshoot behaviour.

4-2 SOWFA yaw: parameter estimation

The pre-filtered SOWFA center line deflection and FLORIDyn deflection can now be translated back to a yaw input into the deflection equation using the LSQ-problem from Section 3-2-2. The estimated yaw angle over time for different downwind distances of both the SOWFA and FLORIDyn 20 deg simulation is shown in Figure 4-7. It can be observed that similar under and overshoot behaviour as that of the deflection occurs (Figure 4-6). The data shown for a downwind distance of 200 m onward. This is because of out of proportionally small (and large) yaw values close-by the turbine, ranging from -2171.4 to 724.9 deg. These values are due to initial deflection close to the rotor, which are an implication of the effect of the turbine yaw on the flow field. The initial deflection can be observed in the wake snapshots of Figure 4-3. For the 2D surface plot of the yaw over downwind distance and time we again refer to Appendix A, Figure A-3. This figure furthermore shows the large deflection close to the turbine. Finally, a similar plot as Figure 4-7, but including the data for the first 200 m downwind, is appended, see Figure A-4.

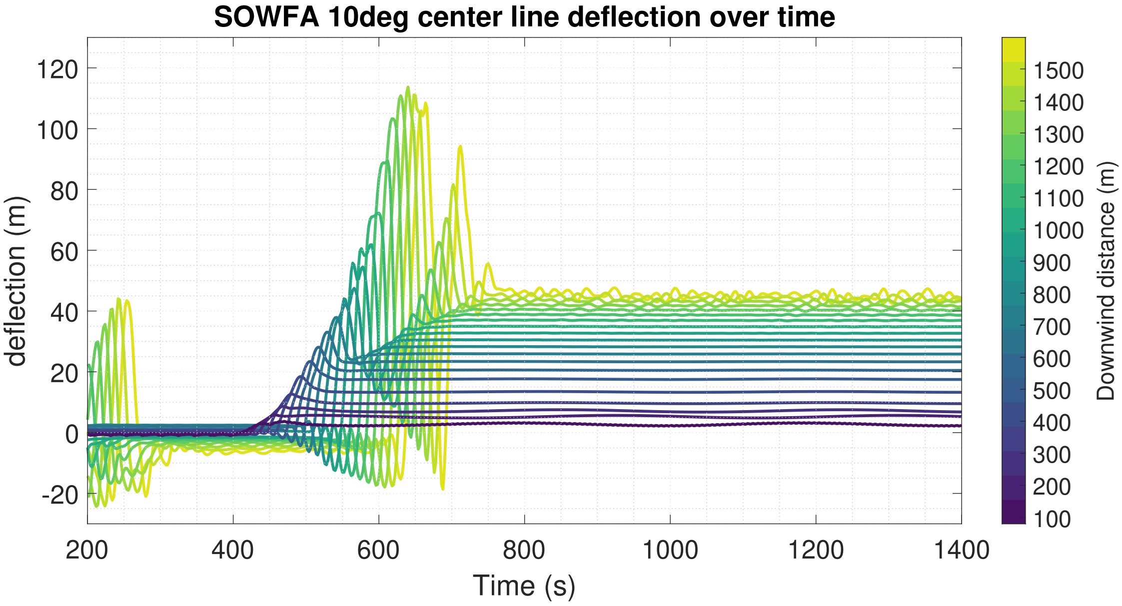

Figure 4-5: SOWFA center line deflection of the 10 deg yaw step over time at different downwind distances.

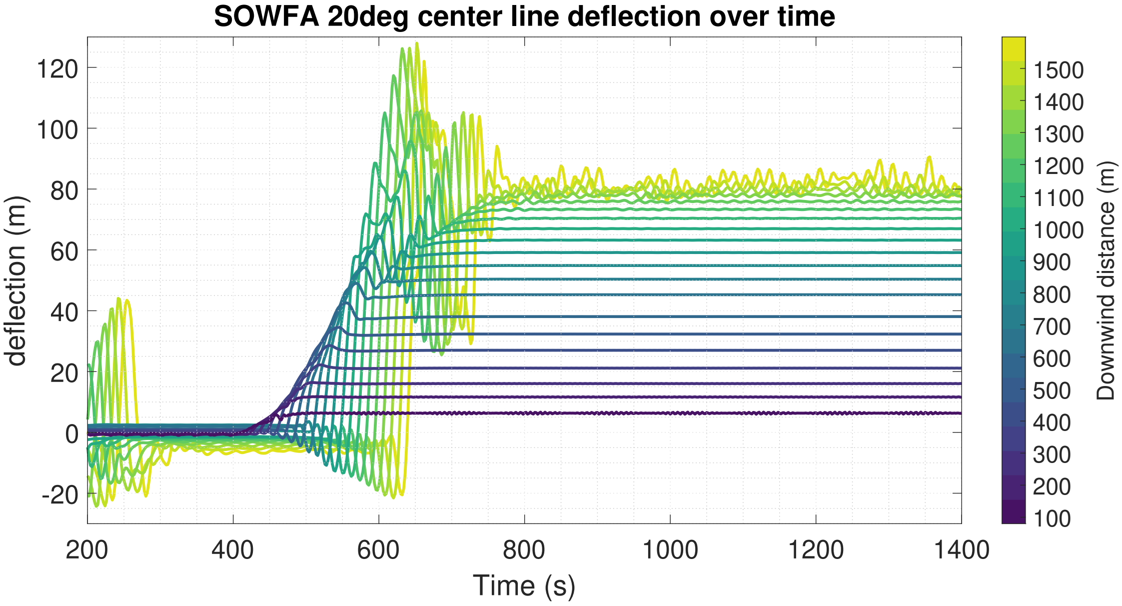

Figure 4-6: SOWFA center line deflection of the 20 deg yaw step over time at different downwind distances.

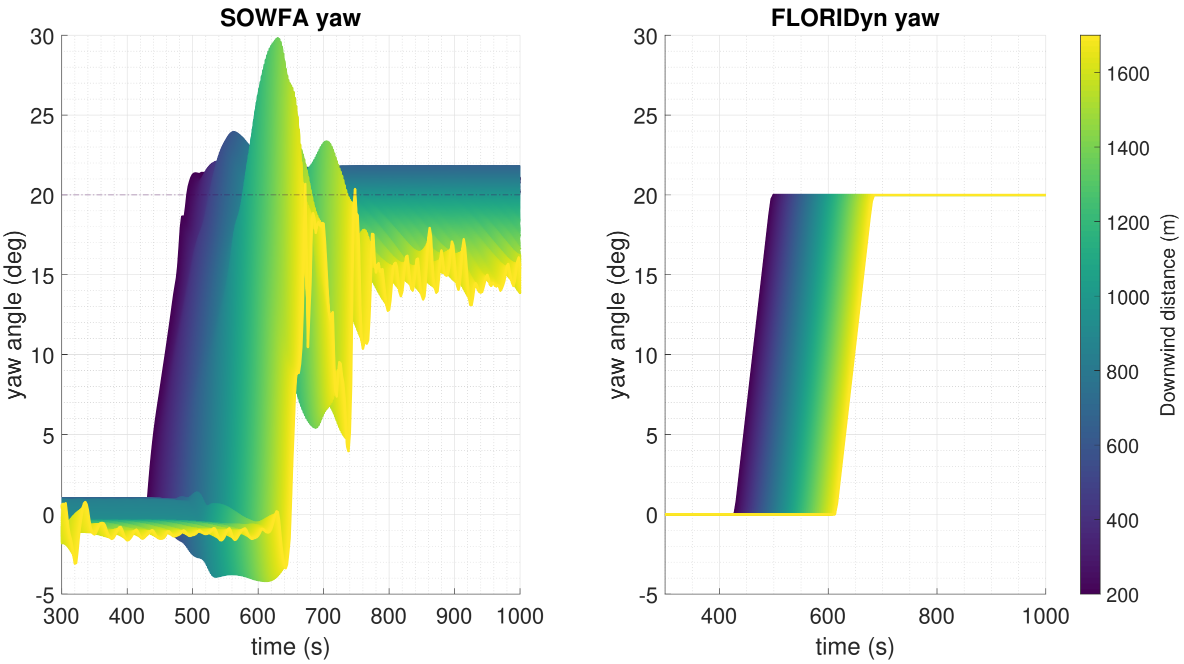

Figure 4-7: Parameter estimated SOWFA and FLORIDyn yaw of the $20\,$deg yaw step over time at different downwind distances.

Chapter 5

System Identification results: dynamic yaw model selection and performance

In the following Chapter, the results from the system identification are presented. The estimated SOWFA and FLORIDyn yaw data from Section 4-2 are used for the MOESP and **DMDc** system identification methods as presented in Section 3-3. To obtain a dynamic yaw model through system identification, an appropriate model order has to be selected. This is done in Section 5-1. Subsequently, Section 5-2 compares the optimal models of the three different identification methods.

5-1 Performance and model order selection of the different identification methods

The identification methods require a pre-determined model order to identify a state-space model. The SVD of the data matrices can be used to determine an optimal model order. Section 5-1-1 determines for which model orders and input data the different identification methods are performed. After which the it looks at the initial model fit of the simulated yaw with the SOWFA yaw. However, the goal of the model is to use the dynamic yaw to obtain a dynamic center line. Therefore, the simulated yaw values are translated to a center line deflection. Section 5-1-2 compares the average, dynamic and steady state fit between the simulated and SOWFA center lines for all SIMO MOESP and **DMDc** models. From this, an optimal model order per identification method is selected. The latter is not performed for the multiple SISO models required to model the center line deflection. This is due to the large number of possible SISO model combinations possible. The optimal SISO models are selected from the results of Section 5-1-1.

Table 5-1: SOWFA simulation properties

model order	10	20	30	40
computation time (s)	32,1	264	2170	5420

5-1-1 Specifications of the different identification methods and initial model fit

This section specifies the performed MOESP and **DMDc** identifications. We first look at the specified data and model order used in both the MOESP identifications. For the MOESP identification, results of different model orders of both the SISO and SIMO identification methods are presented. For both methods, the yaw data at 52 different downwind distances over the simulation time ranging from 300 to 1400 s, with an interval of 2 s is used for the identification. The identified distances range from 59.375 to 1653.125 m with a step size of 31.25 m, being one-tenth of the original extracted center line data. The initial downwind distance of 59.375 m is chosen, to neglect the unreliable and high center line deflection close to the turbine. Furthermore, in the SISO case only one-tenth of the center line data is used to reduce the amount of SISO models required to model the center line over time, and therefore reduce the computation time. Namely, the SISO models model the center line deflection over time at a set downwind distance. This means that 52 SISO models are required to model the center line at 52 distances. The SIMO model simulates the center line deflection at the same 52 distance, but using only a single model. Using all center line data in the SIMO model would result in an underdetermined problem. Therefore, the choice was made to use the same data as in the SISO case. Furthermore, the computation time of the identification process is decreased by using only 52 outputs. To give insight in the fidelity of the decreased center line data, this is plotted in Figure 5-1. This figure shows the entire center line, which pre-filtered, parameter estimated yaw is used as states in the DMDc identification. It furthermore shows which data is used in the MOESP framework. The simulated MOESP output and simulated center line are later compared to the original input and center line data. For this comparison, the 52 MOESP outputs are interpolated to obtain the deflection at the original query points. A shape preserving Piecewise Cubic Hermite Interpolating Polynomial (pchip) is used for this. The result of this interpolation is also show in Figure 5-1, and has a fit of 97.91 % with the original center line. We therefore conclude that one-tenth of the data is sufficient to model the center line. To identify an optimal model order required for the MOESP identification, we can look at the SVD of the Hankel matrix. The log of the singular values for both the SISO and SIMO Hankel matrix are shown in Figure 5-2. We can conclude that no clear gap between the ordered singular values of both the SISO and SIMO Hankel matrices can be determined. Therefore, both MOESP identifications are performed to identify models of order 4 to 40. Because increasing the model order results in exponentially higher computation times of the system identification, finding models with orders beyond 40 are not taken into account in this study. The computation time of the SIMO model with order 40 was 1.5 hours, the computation time of model orders 10, 20, 30 and 40 are shown in Table 5-1.

For the Dynamic Mode Decomposition with Control (DMDc) identification, the SOWFA yaw data from the same time domain as for the MOESP identification is used: 300 to 1400 s. However, the center line data from the entire flow field is used. In comparison, the MOESP identification only used a tenth because of computational complexity due to parameter esti-

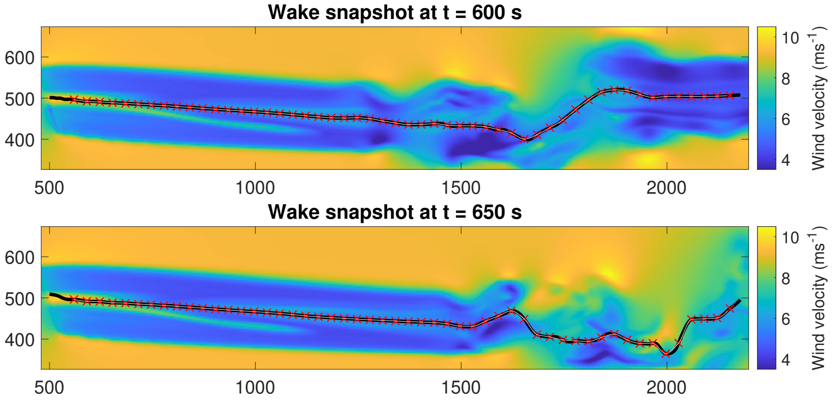

Figure 5-1: Snapshots of the 20 deg yaw step 1T simulation at different time steps. The black line indicates all center line data used in the DMDc system identification before filtering and parameter estimation. The red crosses indicate the downwind distances for which the data is used in the MOESP system identification. The white line shows that pchip interpolation interpolation of these points, resulting in a well defined center line.

mations in the algorithm. We can check if an optimal model order can be derived from the SVD of the combined state and input matrix $\mathbf{\Omega}$. The result is shown in figure 5-3 and, just as the MOESP Hankel SVD, has no clear gap between the ordered singular values. Therefore, the optimal order of the DMDc also has to be derived by identifying multiple models with different order. Because 538 states are present in the data, models with order 1 to 538 can be derived.

We now look at the results from the SISO and SIMO MOESP model fits for different orders of identified models. Because of the high dimensions of the DMDc models, both in states and amount of models estimated, no similar results for the DMDc identification process are shown. However, Section 5-1-2 derives an indication of finding the optimal DMDc model order.

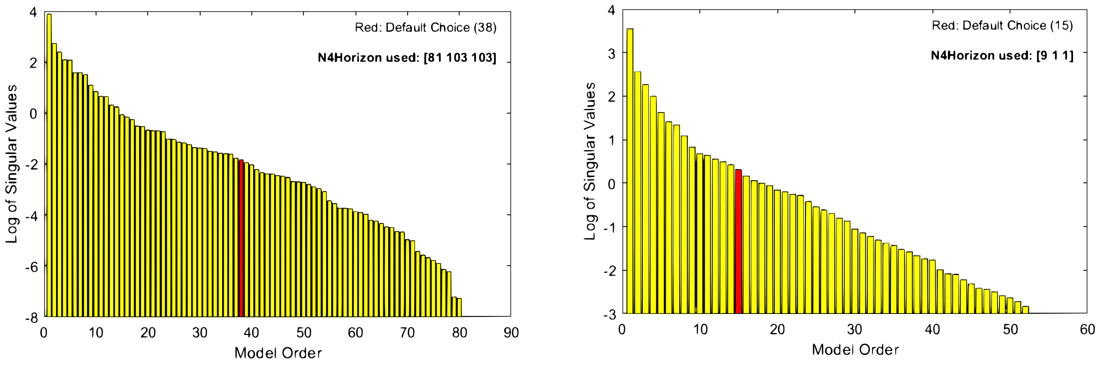

(a) Singular values of the SISO Hankel matrix

(b) Singular values of the SIMO Hankel matrix

Figure 5-2: The log of the singular values for both the SISO and SIMO Hankel matrices.

MOESP - SISO Figure 5-4 shows the 20 best fits between the simulated yaw and SOWFA yaw per downwind distance. Note that most models perform similar per downwind distance,

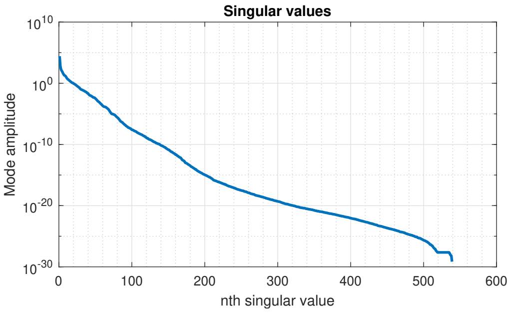

Figure 5-3: The log mode amplitude of the DMDc data matrix singular values.

with a difference of maximal 2 % at most distances. However, for distances further than 600 m downwind, the performance of all models is decreasing. This is due to higher order dynamics of the center line at further downwind distances.

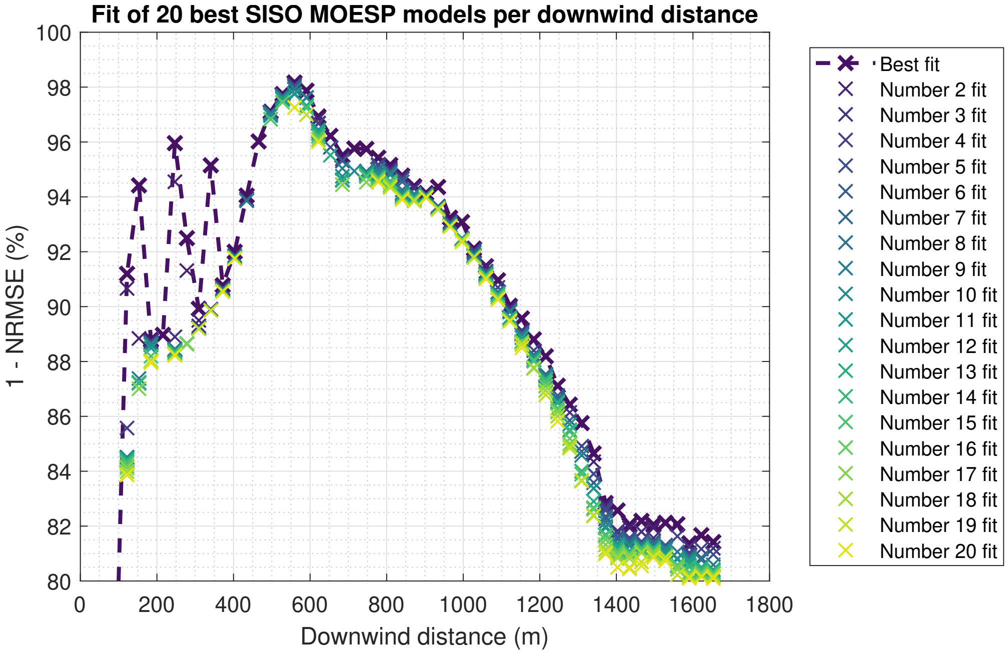

Figure 5-4

MOESP - SIMO Figure 5-5 shows the fit of between the simulated yaw of the SIMO MOESP and SOWFA yaw for every downwind distance. This is shown for all identified model orders. Because a single model is used to simulate the center line yaw, the mean of the fit for every model order is given in the legend. Because the SIMO model simulates the center line yaw, we can furthermore look at the fit of the center line yaw data at every simulation time. These results are shown in Figure 5-6. From this Figure, a decrease in the fit after t = 500 s can be observed. This is due to the increasing complexity of the dynamics, because the yaw step is already traveling past 500 m downwind. The model fit increases again after t = 650 s, when the yaw induced dynamics are moving outside the flow field used for the center line extraction. This can be observed in Figure 4-3. Because the fit over time plotted in Figure 5-6 gives us a good insight in the model performance of both the yaw induced dynamics and the steady state yaw, it is used to derive a performance indication used to determine the optimal model orders for the SIMO MOESP and DMDc methods in Section 5-1-2.

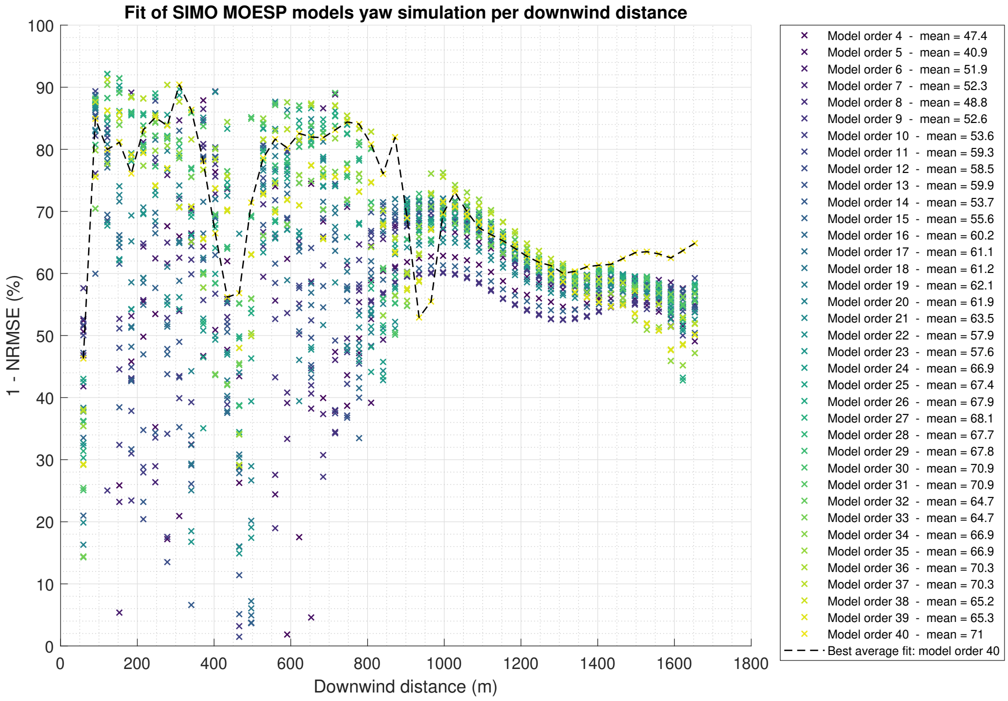

Figure 5-5: Fit of the simulated SIMO MOESP and SOWFA yaw per downwind location. Performed for all possible MOESP model orders. The fit is only calculated for the 52 downwind distances used in the identification.

5-1-2 Optimal model order selection

MOESP - SISO To simulate the center line using the SISO models, a single model is required to model the yaw over time one downwind distance. Because there is only a single output, the best model is chosen as the model that simulates the yaw with the best fit to the training data. Figure 5-7 shows the model order of the 20 best fits at every identified downwind distance. Models that have a higher order than the model with the best fit, are excluded from the right plot for clarity. The purple crosses on the dotted line indicate the best performing models. Using these 52 models, the yaw and thus the deflection at corresponding downwind distances can be calculated. Using interpolation between these identified distances, we can find the yaw and deflection at different downwind distances.

MOESP - SIMO From the SIMO MOESP results of Section 5-1-1, we can use the model fit of the simulated yaw over time to determine an optimal model order. From these results was already already indicated that the SIMO MOESP model with order 40 had the highest average fit. However, our goal is to model the yaw induced center line deflection dynamics. Due to the non-linear relation between the yaw and deflection, we are not sure if the model simulating the best yaw, will also simulate the best center line deflection. Therefore, the

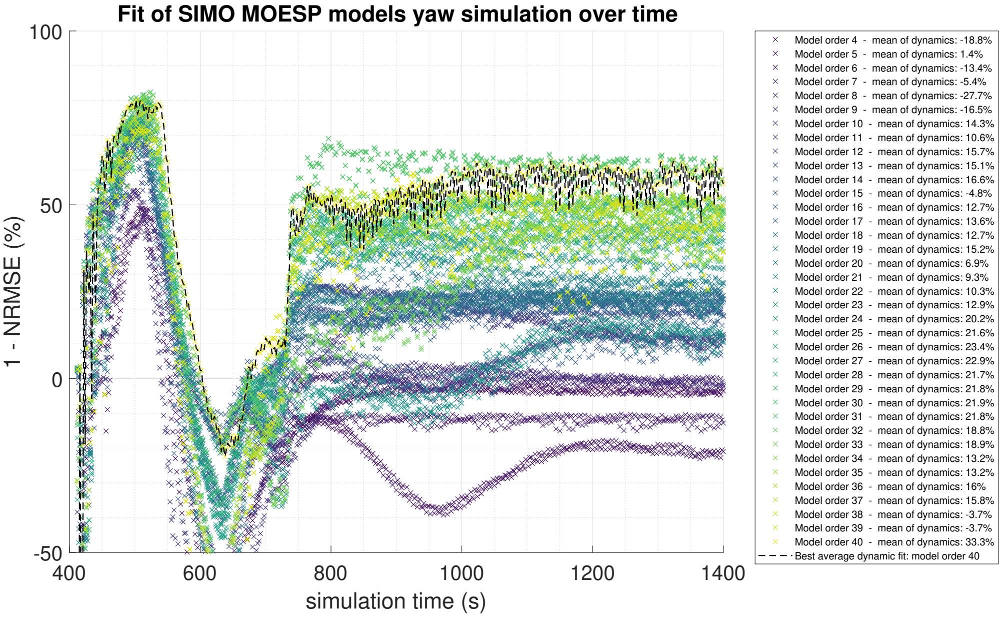

Figure 5-6: Fit of simulated center line yaw over time between the SOWFA and SIMO MOESP. Performed for all possible MOESP model orders. The fit is only calculated for the 52 downwind distances used in the identification. The dynamical section includes the center line between 440 to 800 s of the simulation.

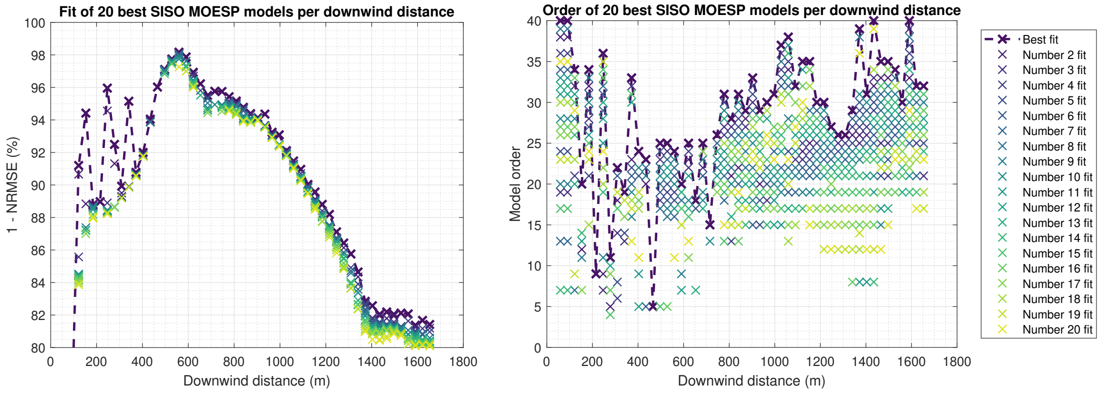

Figure 5-7: 20 best SISO MOESP models, their model fit and model orders.

center line deflection for all SIMO MOESP models is calculated, after which their fit with the SOWFA center line can be derived.

To do this, we first interpolate the simulated yaw to find a yaw description at the same query points for which the SOWFA center line is defined. Then, the deflection is calculated from the interpolated yaw using the deflection function from equation 3-5. Followed by calculating the fit between the simulated center line deflection and the original SOWFA center line deflection. Finally, we can average the fit over the time-domain where center line dynamics are present to obtain an indication for dynamic performance of the models. The turbine starts the yaw step at t = 400s. However, the center line deflections at t = 400s are close or equal to zero before the turbine is yawed. Therefore, the model fit values can become negative. This can also be seen in Figure 5-6. Hence, we start indicating the domain with transient dynamics at a time instance where the deflection is already developed. The dynamic fit is indicated as the mean of the center line fits between 440 and 800 s. Besides capturing the right center line dynamics, the model should also be at steady state when the SOWFA wake is. Therefore, a settled wake performance indicator is derived. The settled wake section is defined as the center line yaw from 900 to 1400 s. The results of the total average fit, the average dynamical fit and the average settled wake fit for all SIMO model orders are shown in Figure 5-8. From these results, we can determine that the 40^{th} order model has both the best dynamic and average fit, being 38.67 % and 59.67 % respectively. furthermore, the settled wake fit is relatively high, meaning a good settled wake is simulated compared to the other SIMO models.

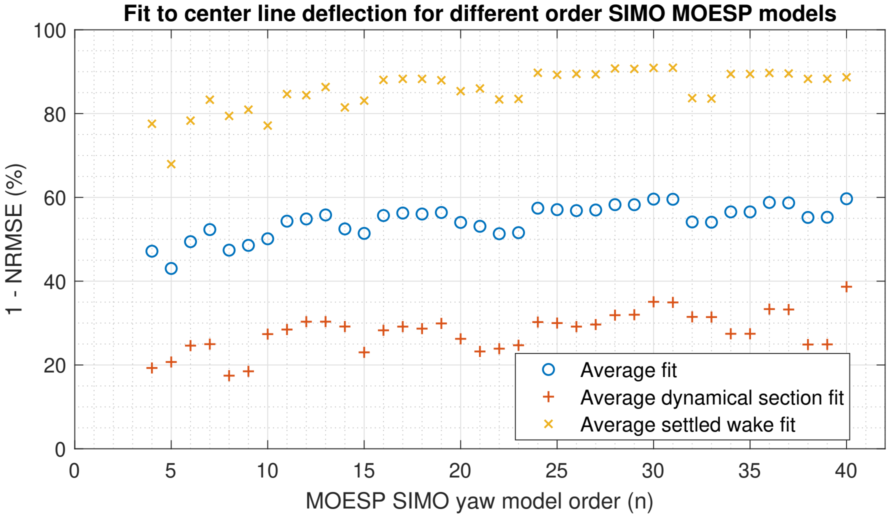

Figure 5-8: Fit between the SOWFA and SIMO MOESP simulated and interpolated center lines for all identified model orders. The dynamical section includes the center line between 440 to 800 s of the simulation. The settled wake includes the center line fit from 900 **s** and onward.

DMDc We can finally evaluate the performance of the DMDc models in the same way as was done for the SIMO MOESP models. The results of average center line fits over the total time domain, the dynamical section and settled wake section are shown in Figure 5-9. From these results an optimal fit for a model order of 190 is observed. The dynamic fit and average fit of the 190th order DMDc model are 79.67 % and 75.77 % respectively. Finally, the DMDc model identification is also performed on the 10 deg yaw data. This optimal fit results in a model of order 186 with average, dynamical and settled wake fit of 75.83 %, 78.24 % and 94.2 % respectively. All three fits for a model order of 50 to 400 are are depicted in Appendix B, Figure B-1.

5-2 Comparison of optimal MOESP and DMDc models

Since we now have obtained an optimal dynamic yaw model from the three identification methods, the models can be compared with each other. Section 5-2-1 shows the center line fit over time of the three different identification methods, followed by the simulated center

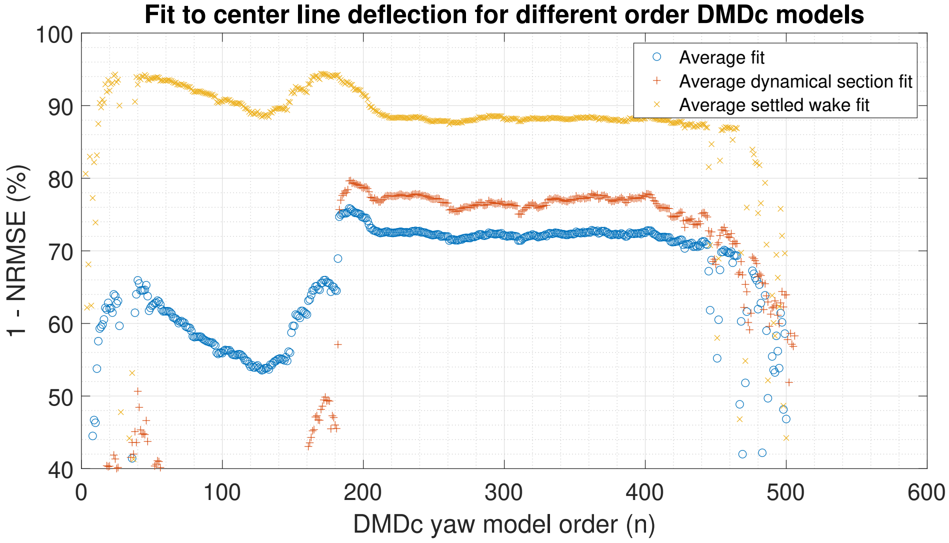

Figure 5-9: Fit between the SOWFA and DMDc simulated center lines for all possible DMDc model orders. The dynamical section includes the center line between 440 to 800 s of the simulation. The settled wake includes the center line fit from 900 **s** and onward.

Table 5-2: The average, average dynamic and average steady state center line fits of the simulated center lines with the SOWFA center line.

Model	DMDc	SISO MOESP	SIMO MOESP	FLORIDyn
Average fit	75.77	70.96	59.67	48.31
Dynamic fit	79.67	67.81	38.67	43.96
Steady state fit	92.87	90.75	86.88	63.91

line snapshots in Section 5-2-2. These snapshots include both the SOWFA and FLORIDyn center line as comparison.

5-2-1 Center line fit over time

The model fit with the unfiltered SOWFA center line of the simulated DMDc, SISO MOESP, SIMO MOESP models and from the FLORIDyn center line are shown in Figure 5-10. From these results there is concluded that the DMDc identified model has the best performance in simulating the 20 deg yaw induced center line dynamics. This is closely followed by the multiple SISO models. Furthermore, the SIMO MOESP model has a worse fit to the data then the original FLORIDyn center line model in a large part of the dynamic section. However, it does capture the steady state deflection almost as good as the DMDc and SISO models. An overview of the average, dynamic and steady state fit from all models is shown in Table 5-2.

5-2-2 Simulated center line snapshots

From the average dynamic fit from Section 5-2-1 we objectively derived that the model identified using DMDc outperformed the two MOESP identified methods. To get more insight on the meaning of the derived center line fits, we now look at snapshots from the simulated,

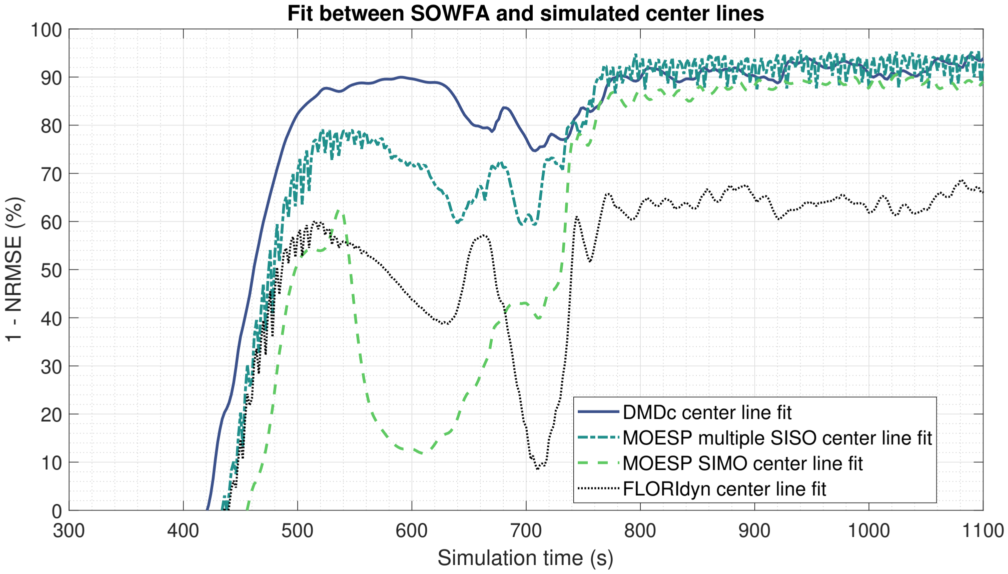

Figure 5-10: Fit between the SOWFA and simulated center lines of the 20 deg yaw step over time.

FLORIDyn and SOWFA center lines. Figure 5-11 shows 9 snapshots, from t = 400 s to t = 800 s with an interval of 50 s. First of all, the results show the reason for the underperforming SIMO MOESP model. From the snapshots at t = 550 s and onward, we see that the model is unable to capture the center line dynamics beyond 1000 m downwind. Instead, the center line deflection has a constant increase for all distances beyond 1000 m. Furthermore, the difference in the dynamic fit between the DMDc and SISO MOESP, 79.67 % and 67.81 % respectively, can be observed. The DMDc model simulated center line follows the SOWFA center line closely. Only at locations where there occur steep hills and valleys in the SOWFA center line, is where the DMDc model simulates a smoother transition. Finally, the multiple SISO models are also unable of simulating these steep hills and valleys. Besides that, the SISO modelled center line also experiences a offset with the SOWFA center line, visible in snapshots at t = 600 s, 650 s and 700 s. Concluding on the snapshots, we observe that the center line snapshots validate the good fit between the dynamic DMDc model simulated center line and SOWFA center line. The model is able of simulating the main center line dynamics, only lacking some amplitude in simulating steep waves of the SOWFA center line. For the interested reader are additional contour plots of the simulated yaw and resulting center line deflection, A matrix, B matrix and 20 different dynamic modes of the 20 deg DMDc model given in Appendix B. The results of the DMDc yaw model implementation in FLORIDyn will be discussed in Chapter 6.

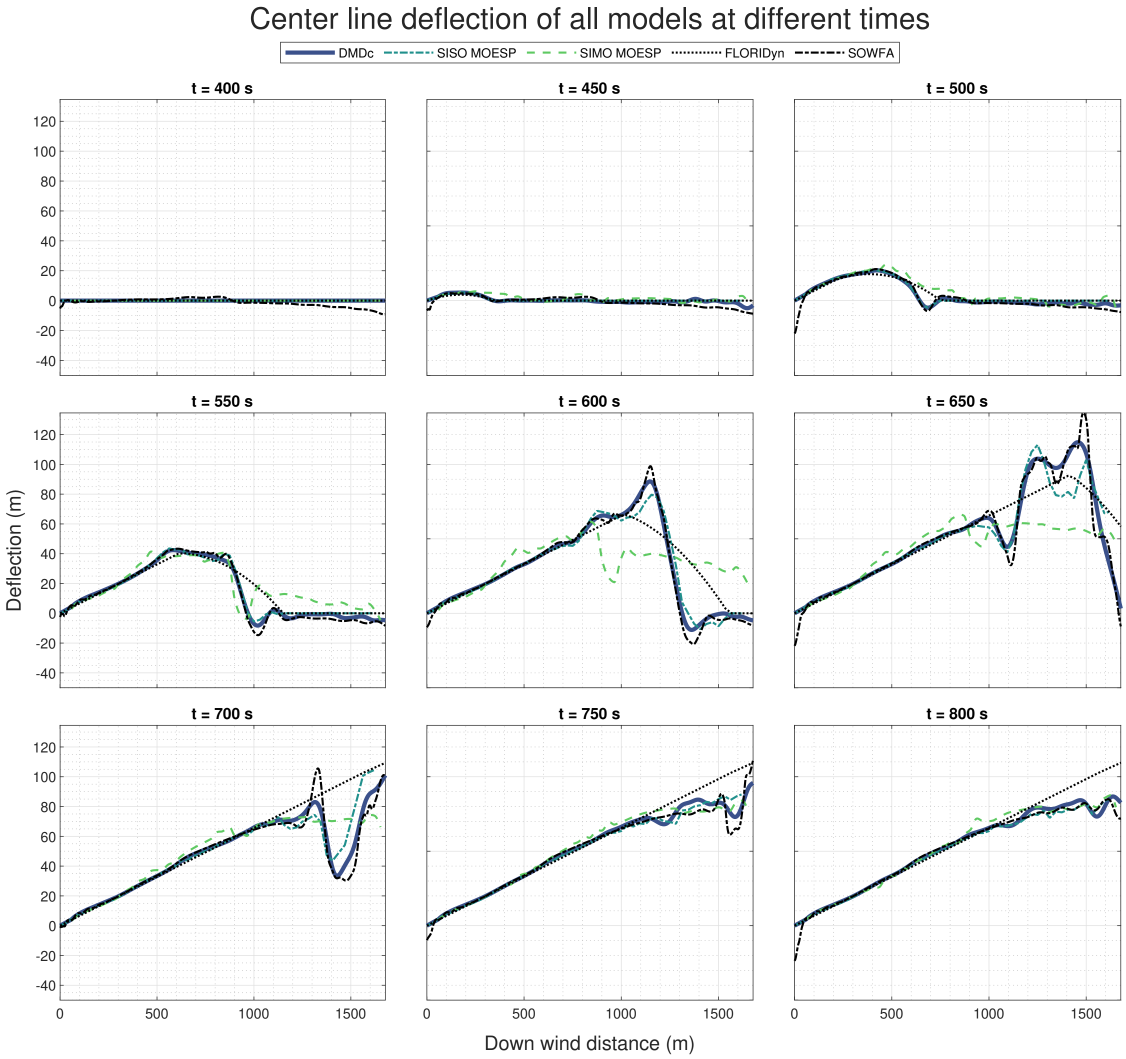

Figure 5-11: Center line deflection snapshots of the different models at multiple time steps

Chapter 6

Results of dynamic center line implementation in FLORIDyn

After obtaining an optimal dynamic yaw model in Chapter 5, this Chapter discusses the results of implementing the model in FLORIDyn. Details of the implementation were discussed in Section 3-5. In Section 6-1, the results of the implemented dynamic model on the single turbine case are discussed. In the 1T case, the effects of the dynamic model are only validated using the same 20 deg yaw simulation as used as training data in the DMDc. Therefore, the results are only used to evaluate the effect of the dynamic yaw model on the wake. This includes both a comparison with the original FLORIDyn CL model and flow field, and with SOWFA. Section 6-1 discusses the results on the two turbine case. This again includes a comparison, with the original FLORIDyn CL model and SOWFA results. Furthermore, results on the generated power are discussed, including the effect of different simulation cases as used in the model identification process.

6-1 1 turbine case

This section evaluates the effect of implementing the dynamic model in FLORIDyn. Section 6-1-1 does this by comparing the FLORIDyn computation time and flow field of the 1T case, both with and without the dynamic model. Section 6-1-2 evaluates the flow field error of these two simulations with SOWFA and compares the flow field of the newly acquired FLORIDyn model with the SOWFA flow fields.

6-1-1 Comparison between FLORIDyn with and without center line dynamics

For the 1T case comparison between the FLORIDyn model with and without dynamic yaw model, the same 20 deg yaw simulation properties are used as in the Dynamic Mode Decomposition with Control (DMDc) identification process (see Table 4-2). The results of the computation time of both models are shown in Table 6-1, and are the average of 10 simulations.

Table 6-1: Computational results of the 1T simulation case using the FLORIDyn CL model with and without the dynamic yaw model included. The results from for a simulation time of 700 s. Furthermore, the computational efficiency is given by the computation time divided by the simulated time and indicated as $t_{\mathrm{comp}}/t_{\mathrm{sim}}$.

	With dynamic CL	Original CL model
Computation time	0.813	0.170
$t_{\mathrm{comp}}/t_{\mathrm{sim}}$	$1.16 \times 10^{-3}\, s\, s^{-1}$	$2.43 \times 10^{-4}\, s\, s^{-1}$

The computational expenses of the dynamic model result in a 4.78 × slower computation. The flow field snapshots from the simulation are shown in Figure 6-1. The snapshots range from 1450 to 1750 s with an interval of 50 s. Furthermore, a final snapshot at t = 1900 s is shown where the center line of both models is settled. Note that the yaw step starts at t = 1400 s. For the DMDc training data, the SOWFA center line was used until 2196 m in the world coordinate system. In this case, the FLORIDyn flow field is simulated until 3000 m. The yaw induced dynamics travel at free wind speed beyond t = 2196 m, and behave as expected. This means that the dynamics reaching the final identified downwind distance flow further without very large deflections. Furthermore, at t = 1900 s, the wake is settled without any large oscillations. From the flow field results, no unexpected wake behaviour can be observed as a result of the dynamic center line implementation. The following step is comparing the FLORIDyn flow field with the SOWFA flow field, this is performed in the following section.

6-1-2 Comparison with SOWFA flow field

This section compares the new FLORIDyn model with center line dynamics with SOWFA for the 1T case. We first compare the flow fields of both models for two different snapshots. Figure 6-2 shows snapshots of the new FLORIDyn model, SOWFA and their error plot at t = 1550 s and 1600 s. Furthermore, the corresponding FLORIDyn center line is visualised in all three snapshots. Empirically, the FLORIDyn center line looks to be good fit for the SOWFA snapshot, at both simulation times. The largest error between the models is observed due to a difference in wake width, or Gaussian fit. FLORIDyn overestimates the wake width near the turbine, and underestimates the width further downwind. Note that scaling of the width, and therefore reducing this error, is out of the scope of this research. What is an effect of the new center line implementation, is a thinner wake at locations where the deflection is increasing or decreasing. Overall, the new FLORIDyn flow field has a good fit with the SOWFA flow field. The same plots as Figure 6-2 for t = 1650 s and 1700 s can be found in Appendix C, Figure C-2.

From the SOWFA flow fields in Section 4-1-2, we observed that the wake and SOWFA center line started to become more complex around 200, s after the the turbine begins its yaw step. To compare the performance of the new FLORIDyn model with the original FLORIDyn CL model at these times, the error plots of both methods are shown in Figure 6-3. This is done for t = 1600 s, 1650 s and 1700 s. Although the average error μ is biased due to the overestimation of the wake width near the turbine, the standard deviation of the error σ is smaller for all FLORIDyn snapshots with center line dynamics compared to those of the original FLORIDyn CL model. This is due to a better overlapping new FLORIDyn wake

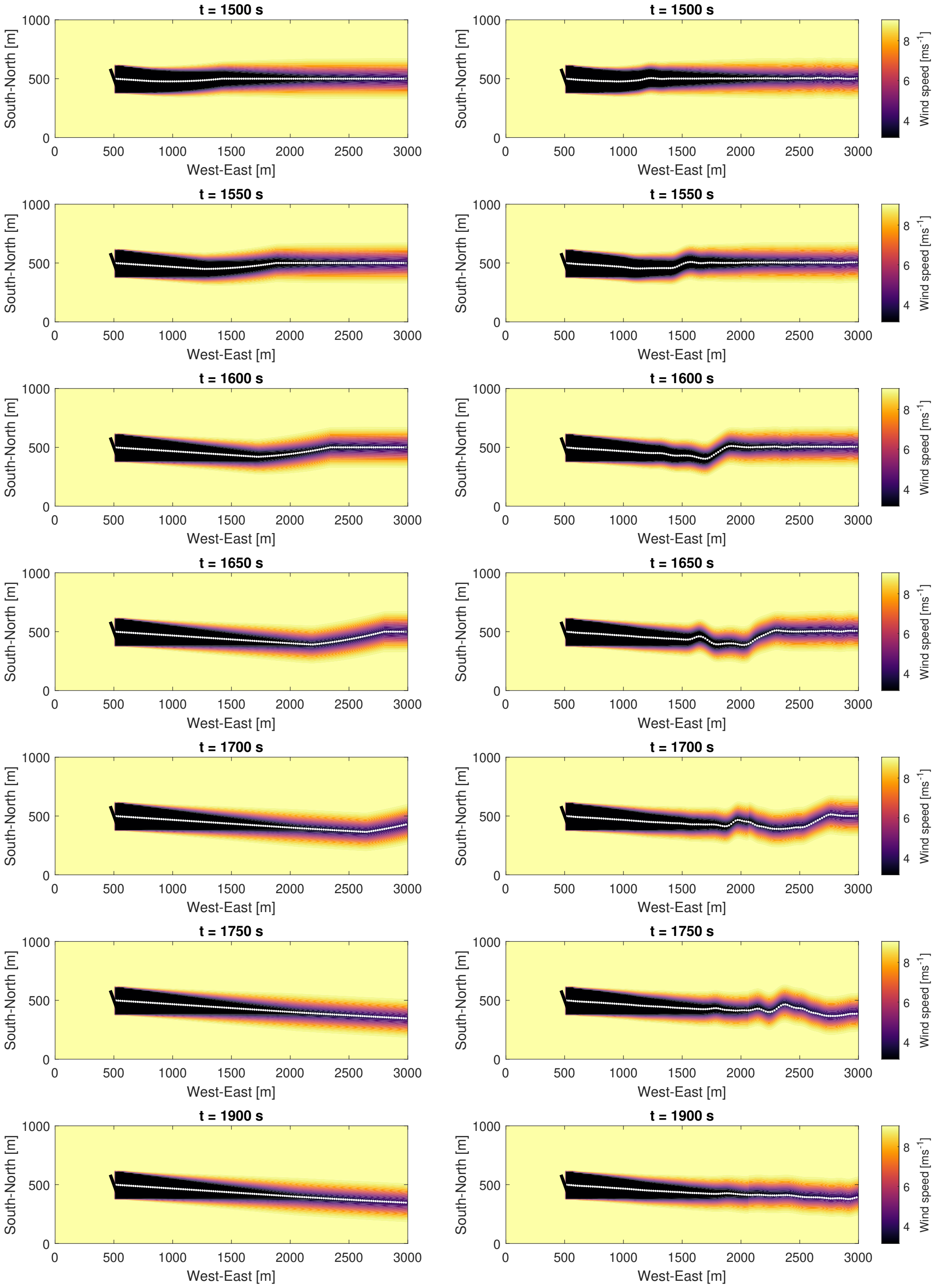

Figure 6-1: Flow field snapshot of FLORIDyn. On the left side the FLORIDyn plot without center line dynamics, and on the right side with the DMDc model dynamics.

with that of SOWFA, resulting in less dark red areas. These dark red areas are where the FLORIDyn velocity deficit is underestimating the SOWFA velocity deficit. Figure C-1 in Appendix C shows comparable results for the wakes at t = 1500 s and 1550 s. Now that the

1T case flow field is validated, the following section will show the result for a 2T case. It compares the flow field and generated turbine output results with the original FLORIDyn CL and SOWFA models. This includes results for both the identified 10 deg and 20 deg yaw case. Furthermore, the dynamic models are validated on robustness using a 15 deg yaw simulation case.

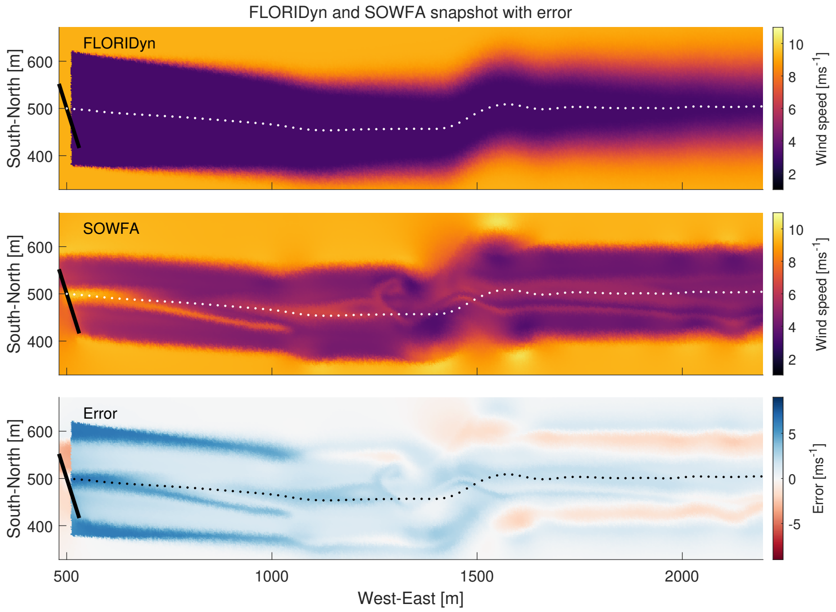

(a) Snapshots at t = 1550 s

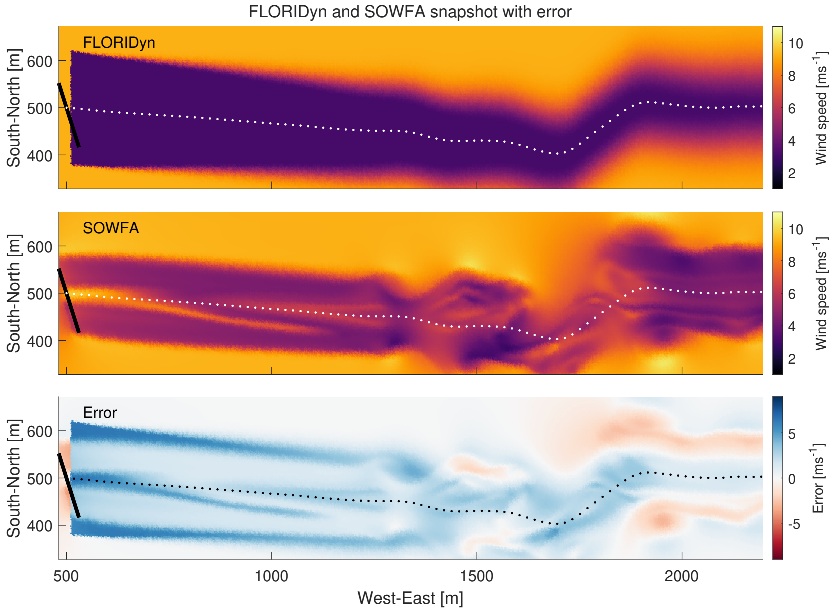

(b) Snapshots at t = 1600 s

Figure 6-2: FLORIDyn with center line dynamics, SOWFA and Error plot at t = 1550 s and t = 1600 s. The error is defined as the wind velocities from SOWFA − FLORIDyn. Furthermore, the FLORIDyn center line is shown in all plots.

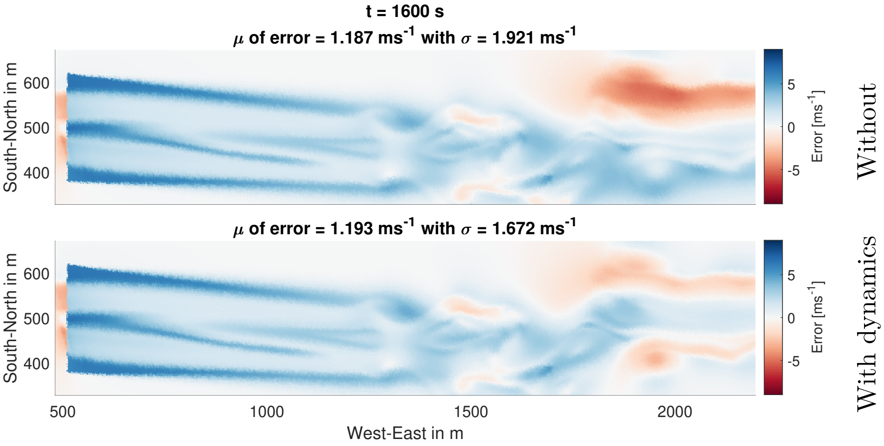

(a) Error plot at t $= 1600$ s. Without and with dynamics respectively.

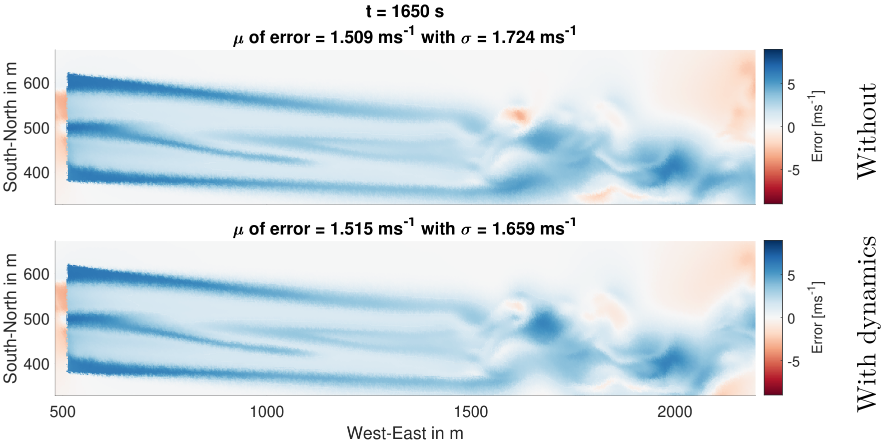

(b) Error plot at t $= 1650$ s. Without and with dynamics respectively.

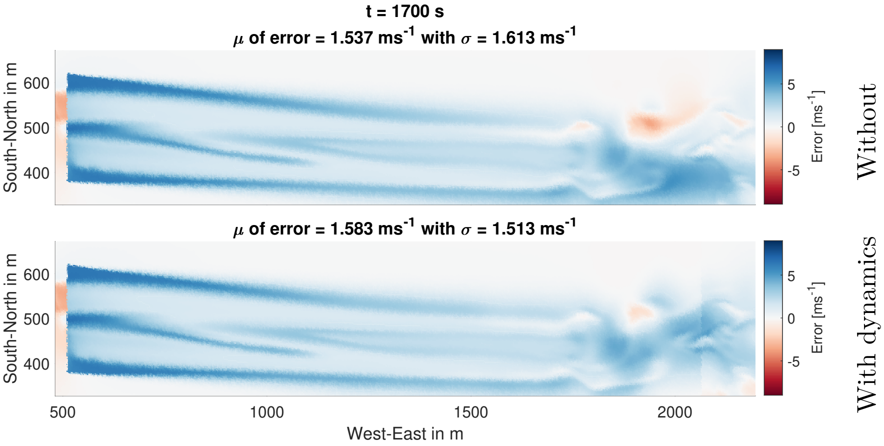

(c) Error plot at t $= 1700$ s. Without and with dynamics respectively.

Figure 6-3: Error plot between FLORIDyn and SOWFA for different time steps. Both without and with center line dynamics. The error is defined as the wind velocities from SOWFA $-$ FLORIDyn.

6-2 2 turbine case

This section evaluates the results of the 2T case of FLORIDyn with dynamic center line implementation. First, Section 6-2-1 compares the FLORIDyn with and without center line dynamics, both on computational efficiency and flow field. Thereafter compares Section 6-2-2 the flow field SOWFA. This is performed for both a 20 deg and 15 deg case. Finally, Section 6-2-3 shows the results of the generated power of the two turbines, also for the 20 deg and 15 deg case.

6-2-1 Comparison between FLORIDyn with and without center line dynamics

This Section compares FLORIDyn with and without center line dynamics. The used simulations are those of a 15 deg and 20 deg yaw of 0.3 deg s^{-1}. by T0. This follows the properties for which the dynamic model was identified. The turbines are located 900 m away from each other, which is just over 5 D. Furthermore, T0 starts yawing at t = 300 s. The remaining simulation properties also follow the 1T case simulation and are specified in Table 6-2. The results of the computation time of this simulation for both the FLORIDyn model with and without dynamic center line implementation are shown in Table 6-3. The consequence of the dynamic center line implementation is a 3.07 × slower computation. With the simulation properties and the effect of the center line model on the computation time specified, we now look at the flow field results of the 20 deg yaw case. Figure 6-4 show the snapshots of the 20 deg FLORIDyn simulation, both with and without center line dynamics. The snapshots range from 350 to 600 s with an interval of 50 s. Furthermore, a final snapshot at t = 1000 s is shown where the center line of both models is settled. Although the yaw is in the opposite direction as in the 1T case, the center line of T0 shows the same behaviour. From the snapshots It can be observed that most complex center line behaviour occurs further downwind than the location of T1. After we already validated the dynamic center line behaviour of the 20 deg yaw step with SOWFA in Section 6-1, we will perform the same validation for the 2T in the following section.

Table 6-2: 2T case simulation properties

Location T0	$(400, 500)$ m
Location T1	$(1300, 500)$ m
Wind speed	$9.2\,\mathrm{m\,s^{-1}}$
Wind inflow angle	270 °
Snap shot time-step	2 s
Yaw-step	20 deg
Velocity yaw-step	$0.3\,\mathrm{deg\,s^{-1}}$
Turbulence intensity	0 %

6-2-2 Comparison with SOWFA flow field

To compare the new FLORIDyn models 2T simulation with SOWFA, we again use SOWFA flow field snapshots. In this section, we compare both the 15 deg and 20 deg simulation,

Table 6-3: Computational results of the 2T simulation case using the FLORIDyn CL model with and without the dynamic yaw model included. The results are from a simulation time of 700 s. Furthermore, the computational efficiency is given by the computation time divided by the simulated time and indicated as t_{comp}/t_{sim}.

	With dynamic CL	Original CL model
Computation time	1.19	0.388
t_{comp}/t_{sim}	$1.7 \times 10^{-3}\,s\,s^{-1}$	$5.54 \times 10^{-4}\,s\,s^{-1}$

with properties specified in Table 6-2. The SOWFA numerical properties are shown in Table 6-4. Furthermore, the horizontal slice of the domain, including refinements is visualised in Figure 6-5. With the SOWFA simulation properties specified, the following paragraphs will now compare the 20 deg and 15 deg simulation cases respectively. For both cases, the 20 deg trained DMDc model is used.

Table 6-4: 2T case SOWFA numerical properties

Turbine model	ALM
Base cells	10 m × 10 m × 10 m
First refinement	5 m × 5 m × 5 m
Second refinement	2.5 m × 2.5 m × 2.5 m
Simulation time-step	0.2 s

20 **deg case** As was done in the 1T FLORIDyn case, the 2T case is first validated by comparing the FLORIDyn, SOWFA and corresponding error flow fields. To correctly model the power output of T1, we are interested in validating the FLORIDyn snapshots when the center line dynamics of T0 occur at T1. Therefore, the snapshots at t = 400 s and 450 s are shown in Figure 6-6. From the snapshot at t = 400 s, it can be seen that the FLORIDyn center line and wake are slightly ahead of the SOWFA wake. However, this difference is only minimal, and the center line deflection at T1 shows a good fit with SOWFA for both cases. Besides this comparison with SOWFA, the error plots of both the FLORIDyn model with and without the dynamic center line model are again plotted in Figure 6-7. This is again done for the time steps at 400 s and 450 s. In addition, this is shown in Figure 6-8 for t = 500 s. The decrease in the standard deviation of the errors is only one fourth compared to the error plots of the 1T case. Mainly, because there are still noticeable dark red areas in the 450 s and 500 s error plots of FLORIDyn with dynamics. Most notable are the lack of FLORIDyn velocity deficit South of T1 at t = 450 s and South of the wake of T1, around 1700 m downwind, at t = 500 s. What the dynamic model does capture better than the original FLORIDyn model, are the velocity deficits North of the turbines. Note that this also is the direction of the wake deflection.

15 **deg case** After having looked at the 20 deg case, we now look into the 2T simulation with a 15 deg yaw. This is done to validate the robustness of the 20 deg identified model. The comparison with SOWFA at t = 500 s and at the steady state time of 1000 s are shown in Figure 6-9. From the first snapshots at t = 500 s, the model looks to approach the

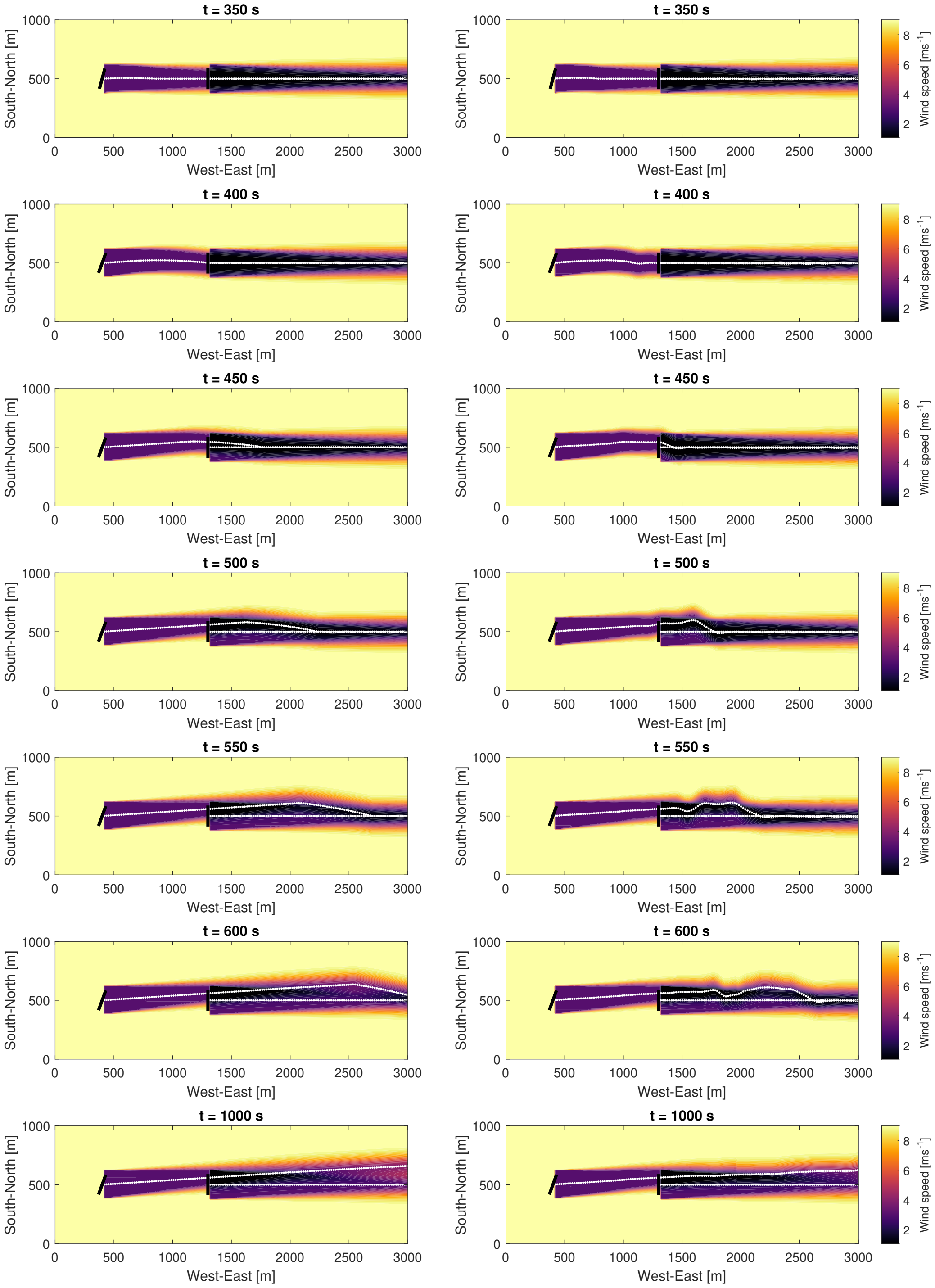

Figure 6-4: Flow field snapshot of the 20 deg yaw step FLORIDyn simulation. On the left side are the flow field plots without center line dynamics, and on the right side with dynamics.

SOWFA center line dynamics. However, from the steady state plot at t = 1000 s, there is still oscillation visible in the FLORIDyn center line. To better analyse the velocity deficit and wake dynamics at T1, the following section will show the turbine power outputs. This

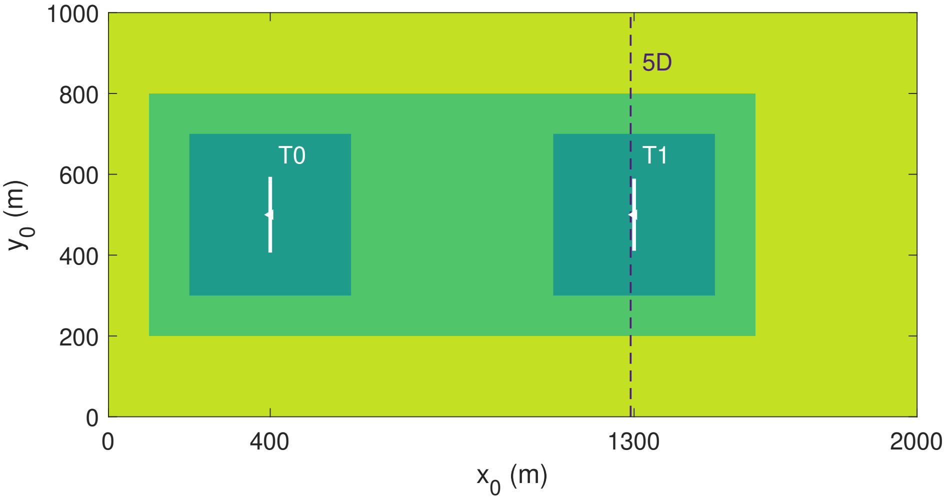

Figure 6-5: The flow field including refinements of the 2T SOWFA simulation. The unrefined (light green) flow field has a base cell size of 10 m × 10 m × 10 m.

includes the power output of this 15 deg case with 20 deg dynamic model, from which the T0 wake oscillations are noticeable.

6-2-3 Turbine power output

So far we have only looked at and compared the flow field results of the new FLORIDyn model. However, the 2T case also models the effect of the wake of T0 on generated power output of T1. In the power output of the 2T case, the improper wake advection was noticeable as was established in Section 2-3-5. For that reason will this section compare the new, dynamic, power output of the 2T case with SOWFA and the original FLORIDyn CL model. The following paragraph will first validate the power output for the 20 deg yaw case. Then, we once more look at the 15 deg yaw case to verify the robustness of the DMDc identified model. This is done using both the 20 deg and 10 deg trained model.

20 deg case The results of the generated power output of both turbines in the 20 deg yaw case are shown in Figure 6-10(a). These results are included for the new FLORIDyn model, SOWFA and the original FLORIDyn CL model. Although there is an offset between the FLORIDyn generated power and SOWFA power for both turbines, the effect of the new center line dynamics on the generated power of T1 stand out. To evaluate the results without the offset due to poor FLORIS parameter scaling in the 0 % TI simulations, the results of the normalized power outputs are shown in Figure 6-10(b). For T0, these results are obtained by dividing the power output of each model, by their own power output at t = 300 s. This is the moment the yaw step is induced. For T1, the normalized power output is obtained by dividing the power of the models by their own power at t = 400 s. This is the instance right before the wake advection of T0 reaches T1. From the results, we observe that the new FLORIDyn model simulates a similar over- followed by an undershoot behaviour as SOWFA. However, what still lacks is second, smaller, overshoot after which the power slowly decreases before settling. A second difference can be seen in how the power initially increases. In the SOWFA

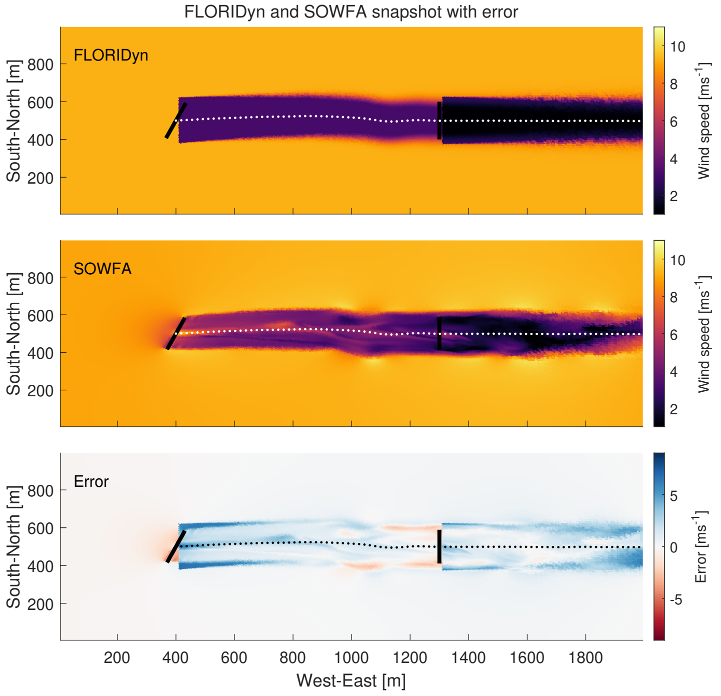

(a) Snapshots at t = 400 s

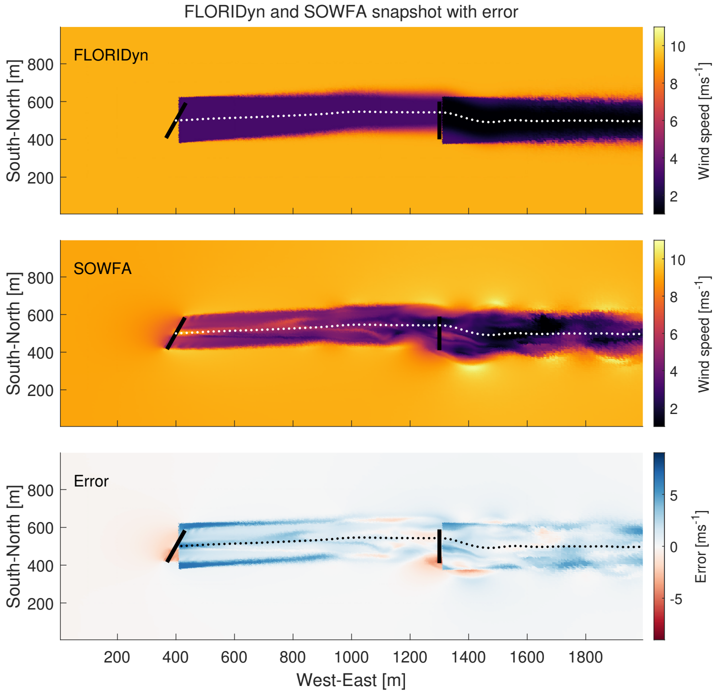

(b) Snapshots at t = 450 s

Figure 6-6: FLORIDyn with center line dynamics, SOWFA and Error plot at t = 400 s and t = 450 s for the 20 deg yaw simulation. The error is defined as the wind velocities from SOWFA − FLORIDyn. Furthermore, the FLORIDyn center line is shown in all plots.

simulation, this is more gradually than in the new FLORIDyn model. For the results on the generated power output and normalized generated power output of the 10 deg yaw case, we would like to refer to Figure C-3 in the Appendix.

15 **deg case** The flow field and center line snapshots of the 2T 15 deg yaw case, using the 20 deg trained model, showed oscillations when a steady state was expected. To evaluate the effect of this at T1, its generated power is shown in Figure 6-11(b). From this plot, we notice similar power output oscillations due to the steady state center line oscillation. We furthermore check the power output of this simulation using the 10 deg yaw step trained model. This result is shown in Figure 6-11(a). Although the center line does settle in this case, this model results in different generated power dynamics. The model follows the initial overshoot as depicted in the validation data. However, this is followed by a double overshoot. The verification of the 15 deg case shows that both the 10 deg and 20 deg result in a stable center line. However, they show different dynamics at T1 compared to the SOWFA validation data, resulting in different dynamics in its generated power. The normalized generated power output for both cases is shown in Figure 6-12. We observe that both models are able to model the initial normalized generated power increase. Again with a faster increase than occurs in the SOWFA model, as we also concluded in the 20 deg yaw case. However, both models show different dynamical behaviour when the generalized power decreases and settles afterwards.

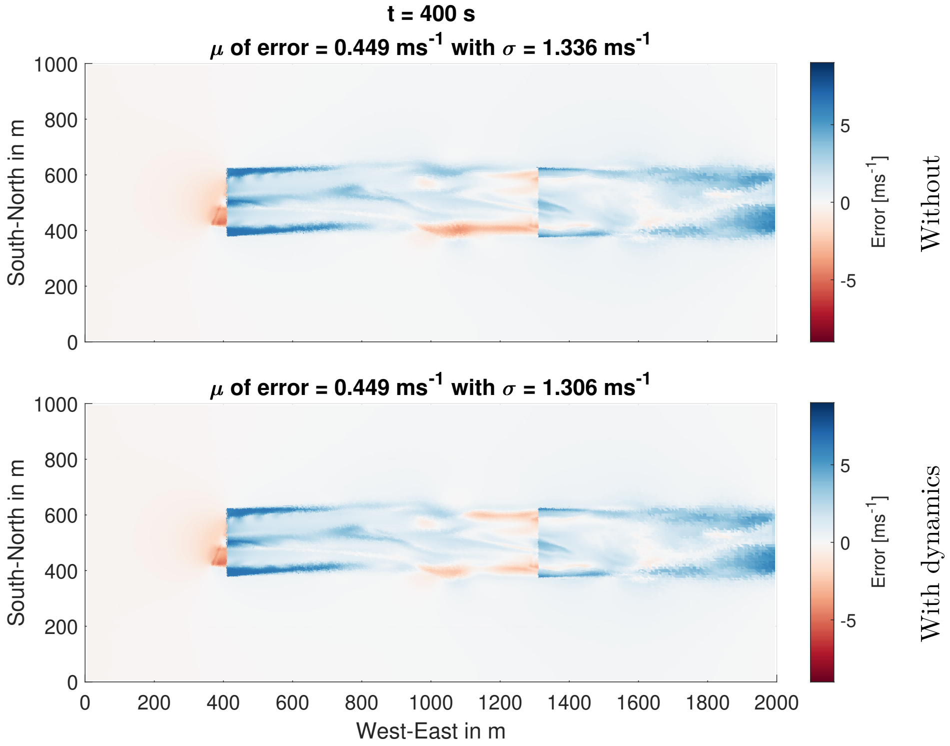

(a) Error plot at t $= 400$ s. Without and with dynamics respectively.

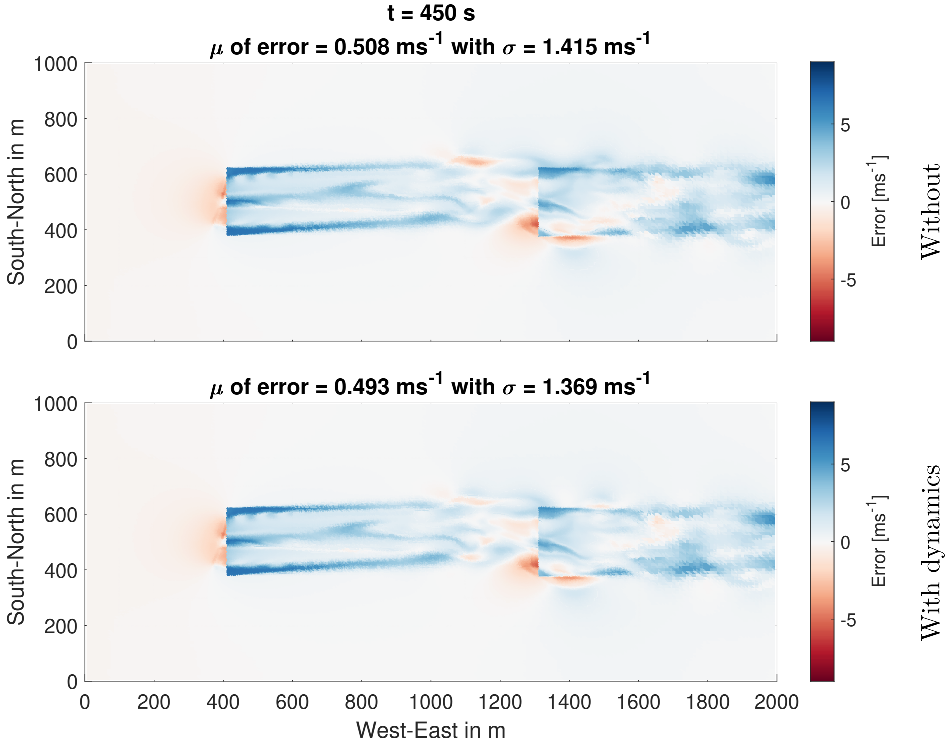

(b) Error plot at t $= 450$ s. Without and with dynamics respectively.

Figure 6-7: Error plot of the 2T 20 deg yaw case between FLORIDyn and SOWFA at t $= 400$ s and 450 s. Both without and with center line dynamics. The error is defined as the wind velocities from SOWFA $-$ FLORIDyn.

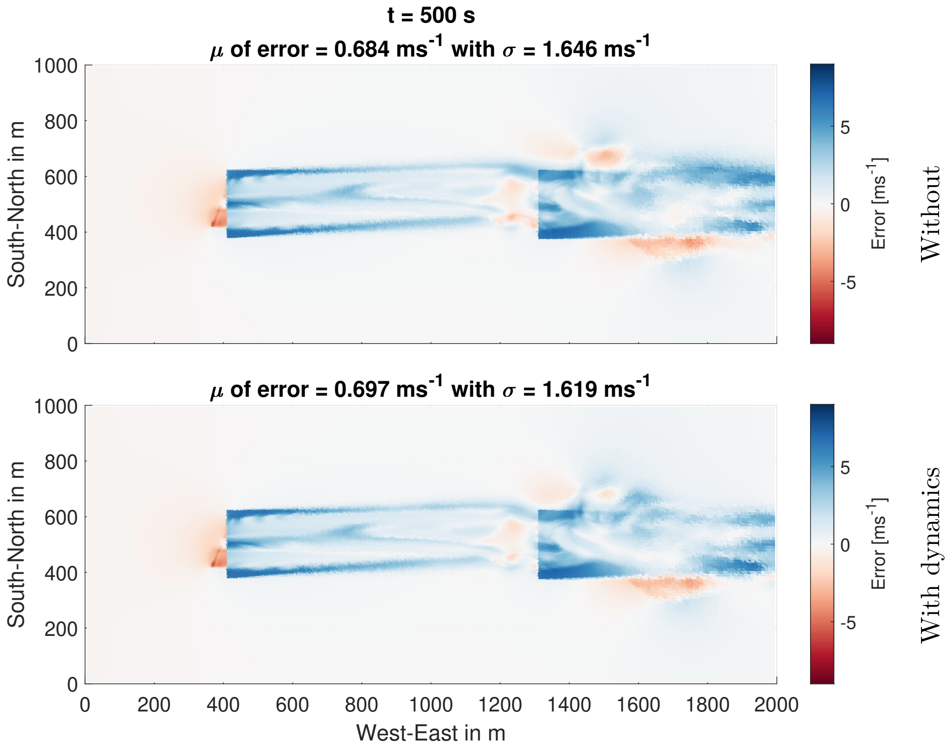

(a) Error plot at t $= 500\,$s. Without and with dynamics respectively.

Figure 6-8: Error plot of the 2T $20\,$deg yaw case between FLORIDyn and SOWFA at t $= 500\,$s. Both without and with center line dynamics. The error is defined as the wind velocities from SOWFA $-$ FLORIDyn.

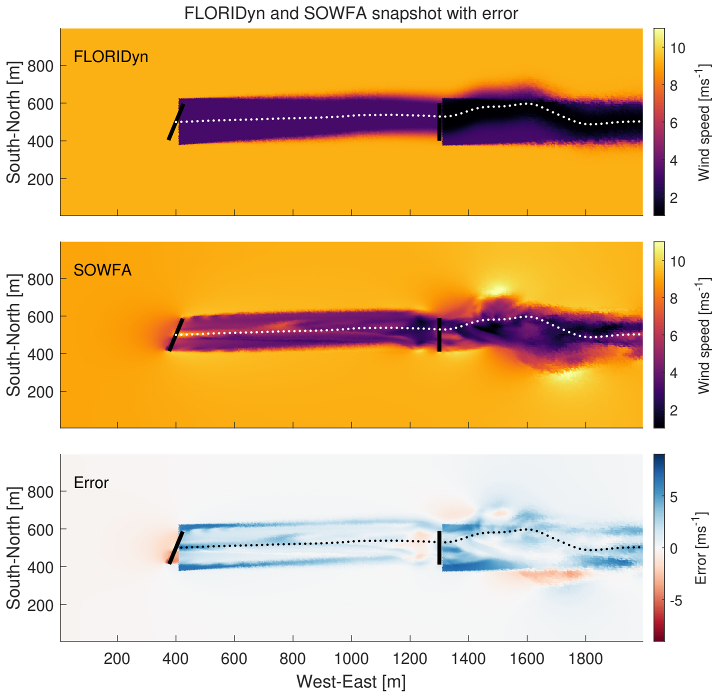

(a) Snapshots at t $= 500\,$s

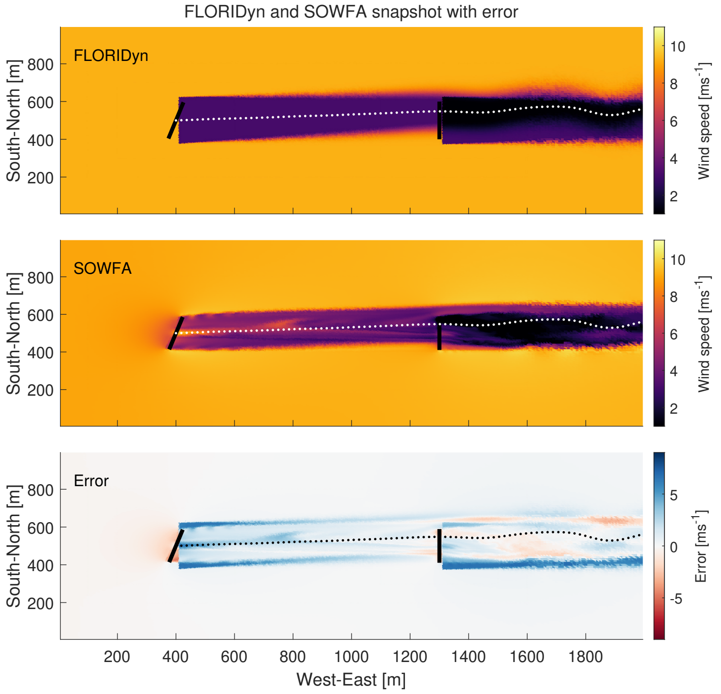

(b) Snapshots at t $= 1000\,$s

Figure 6-9: FLORIDyn with center line dynamics, SOWFA and Error plot at t $= 450\,$s and t $= 1000\,$s for a $15\,$deg yaw simulation. The dynamic system is trained on the $20\,$deg case. The error is defined as the wind velocities from SOWFA $-$ FLORIDyn. Furthermore, the FLORIDyn center line is shown in all plots.

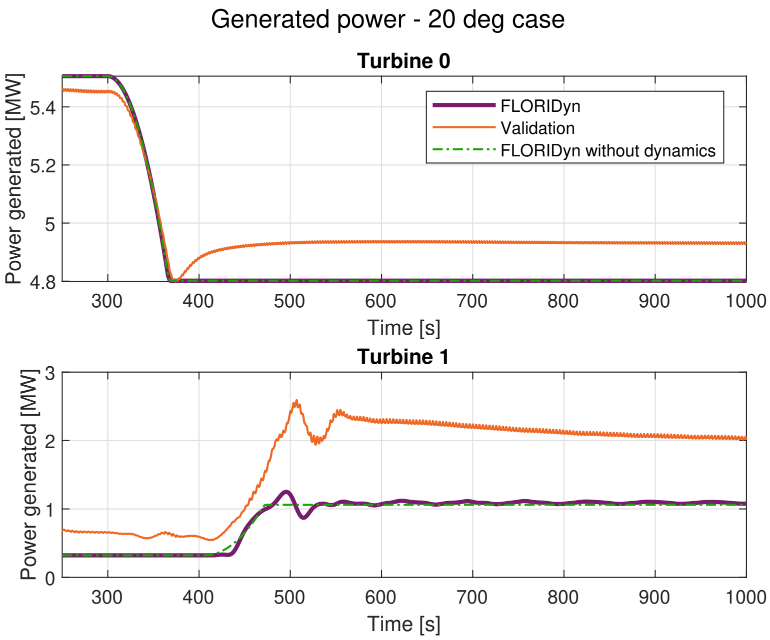

(a) Generated power output.

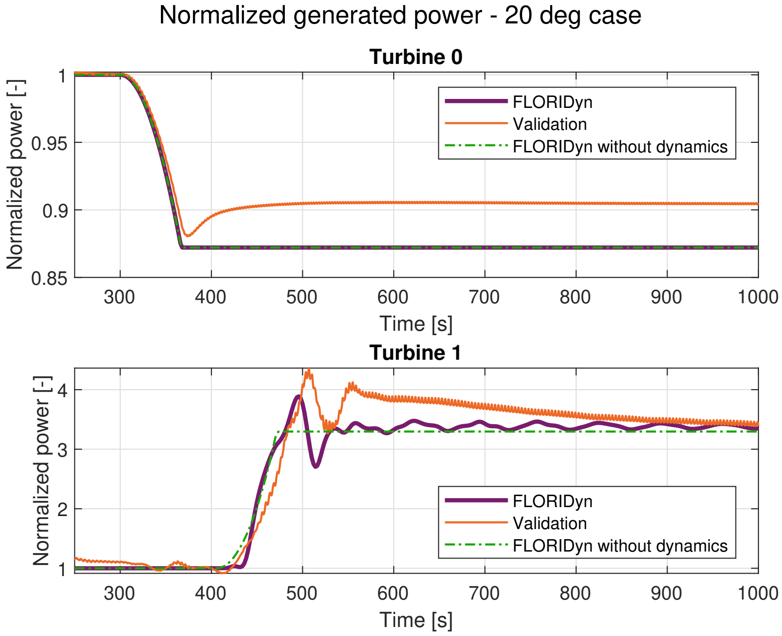

(b) Normalized generated power output.

Figure 6-10: Both the generated power output and normalized generated power output of the $20\deg$ 2T case. The output of both the FLORIDyn simulation with and without center line dynamics is visualised.

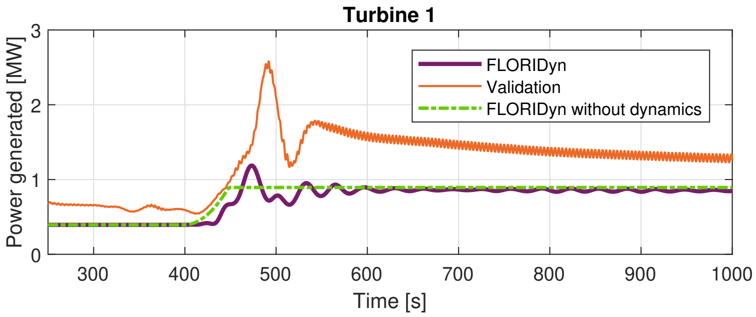

(a) 15 deg simulation with 10 deg trained model

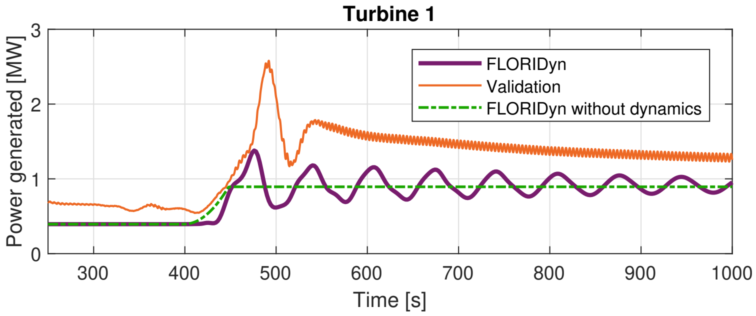

(b) 15 deg simulation with 20 deg trained model

Figure 6-11: Power output of T1 from the $15\ \mathrm{deg}$ 2T case, both for a 10 deg and 20 deg trained DMDc model. The power output of both the simulation with and without center line dynamics is visualised.

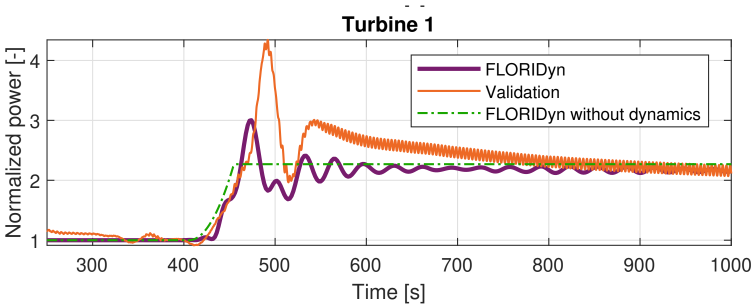

(a) 15 deg simulation with 10 deg trained model

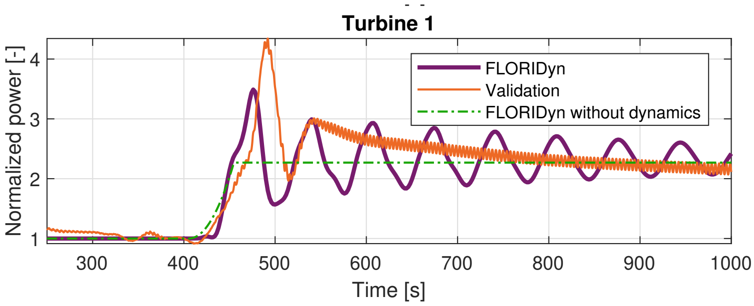

(b) 15 deg simulation with 20 deg trained model

Figure 6-12: Normalized generated power output of T1 from the $15\ \mathrm{deg}$ 2T case, both for a 10 deg and 20 deg trained DMDc model. The power output of both the simulation with and without center line dynamics is visualised.

Chapter 7

Conclusion, recommendation and discussion

7-1 Conclusion

This master thesis identified improper advection in the dynamic wake description of FLORIDyn compared to the SOWFA model. The cause of this improper wake advection is the lack of realistic dynamics in the way turbine state changes travel through the FLORIDyn wake. Furthermore, identification and modeling of dynamic wake advection lacks in current literature in the field of wind farm modelling. Therefore, the goal and novel contribution of this thesis is to propose a method able to identify and accurately model the propagation of turbine states in the wake, resulting in proper advection behaviour of the FLORIDyn wake. To verify this goal, the following main research question was posed:

Will the proposed cycle of identifying a state-space model relevant to accurately model the propagation of wind turbine state changes through the FLORIDyn wake improve the models performance?

In the proposed methodology, three different methods of system identification were proposed, based on either the MOESP or the Dynamic Mode Decomposition with Control (DMDc) system identification method. Although the extracted SOWFA center line data was high dimensional and showed nonlinear behaviour, the DMDc method proved to be well suited for identifying a Reduced Order Model (ROM) capable of accurately modelling dynamic turbine state changes. Furthermore, the implementation of the state-space model showed an increase in the FLORIDyn model performance. This performance increase was evaluated by three performance objectives, which were derived in the Introduction. The first objective was to decrease the difference in center line description and flow fields between FLORIDyn and SOWFA. The dynamic center line, obtained from the simulated dynamic yaw by the DMDc identified model, showed to have a good dynamic fit with the extracted SOWFA yaw. The center line fit during its increase in deflection, the dynamic fit, and at steady state showed to be 79.67 % and 92.87 % respectively. For comparison, the corresponding original FLORIDyn center line fits are 43.96 % and 63.91 % respectively. As a result of implementing the dynamic model, the overlap between the FLORIDyn and SOWFA wakes in flow field snapshots was improved. This was demonstrated by the flow field error plots, and decrease in corresponding standard deviation of the error. The second performance objective was to decrease the difference in generated turbine power between FLORIDyn and SOWFA. To validate this, a two turbine case was used. The improved wake advection of the new FLORIDyn model showed to result in similar dynamics in the power output of the downwind turbine, as was modelled by SOWFA. The final objective was to improve the FLORIDyn model, by means of achieving previous objectives, at a minimal cost of computational power. This is of importance for the possible use of FLORIDyn as a surrogate model in a Model Predictive Control framework. As implemented in this thesis, the effect of the model was a 3.07 to 4.78 times slower computation time compared to the original FLORIDyn CL model. This is an increase of less than an order of magnitude in computational efficiency. However, future research on wind farm control is required to determine if this trade off between increasing wake advection and increasing computation time is beneficial.

The main research question was subdivided in three sub questions. These research questions target different parts of the proposed identification cycle. The first research question targeted the data acquisition from the high-fidelity SOWFA flow field snapshots, and was stated as follows:

Is it possible to accurately extract a high-fidelity center line deflection from SOWFA simulations, from which high-fidelity FLORIDyn turbine states can be estimated?

The proposed weighted geometric center approach resulted accurate empirical center lines for the complementary flow field snapshots. The SOWFA center lines showed similar behaviour for both the 10 deg and 20 deg simulation case, although varying in amplitude and complexity. Using the deflection function and specified least-squares problem, a high-fidelity dynamic yaw could be estimated from these SOWFA center line. The extracted dynamic yaw was then used in the process of identifying a dynamic yaw model. Therefore, the following research question was derived:

Is it possible to identify systems translating the FLORIDyn turbine states to more dynamical turbine states and implement these into FLORIDyn to achieve better wake advection?

As stated in the answer to the main research question, was the DMDc identification method suitable for identifying the high dimensional and nonlinear turbine states over downwind distance. Implementing the ROM showed similar behaviour in wake advection between the new FLORIDyn model and SOWFA flow field snapshots from the single turbine simulation. Furthermore, the new FLORIDyn model showed to be able to simulate similar dynamics as SOWFA in the power output of the downwind turbine in a two turbine case. Finally, the third research question relates to the identified model:

How robust are the identified systems to other simulation cases?

To answer this question, the FLORIDyn simulation of a 15 deg yaw step was performed. This amplitude was not used in the identification of the dynamic center line models. Although the simulated center line dynamics were stable, the flow field snapshots and power output showed that the 10 deg and 20 deg identified models lacked the right dynamics located at the downwind distance where the second turbine was located.

7-2 Discussion and recommendations for future work

The proposed data acquisition, system identification using DMDc and implementation of this model in FLORIDyn shows to be promising in increasing the models fidelity. However, the used data, methodology and validation in this study result in certain limitations of the research. The SOWFA flow field data in this study, used to extract the high-fidelity center line, is first of all limited to the 2D snapshot at hub-height. Because vertical snapshots of a yawed wake show that the wake profile is kidney shape instead of circular, is the fidelity of a center line extracted from 2D data up to discussion. Another note on the performed SOWFA simulations, is that the wind speed between the 1T and 2T case is different. The 1T case is performed with a wind speed of $9.2\,\mathrm{m\,s^{-1}}$, compared to the $8.6\,\mathrm{m\,s^{-1}}$ used in the 2T case. This difference results to a dynamic model that captures the wake advection for the faster wind speed, which is then compared to advection behaviour at a slightly slower wind speed. The study is also limited to the use of 0 %TI simulations. This results both in poorly trained steady state FLORIDyn parameters, and a lower fidelity of the extracted center line in real life conditions. However, it enables for better center line extracting without noise due to turbulence in the wake and flow field. Furthermore, the performed single turbine simulations for the center line extraction limit the training data for the system identification to that of a single yaw step. This is furthermore due to the constraint of the DMDc method, which is limited to the use of only a single input-output data set in identifying a state-space system. The DMDc identification process was further only performed with the use of all center line observables as DMD states, thus not taking the objective in minimising the computational cost of the dynamic yaw model into account. Finally, the validation process does not include verifying simulation cases in which the identified yaw models are robust enough in properly modelling the wake dynamics outside the scope of the simulation used in acquisition of the training data. Therefore, this study is mainly a proof-of-concept of the methodology able to extract high-fidelity wake dynamics, identifying these and implementing them in a parametric model. The discussion on the limitations of the work does identify opportunities for improvement and extension of the used framework and application.

Recommendations for future work

1. Future work should include a study into the fidelity of the use of 2D snap shots at hub height, or extend the center line extraction to 3D SOWFA data. This is required to increase the fidelity of the extracted center line. The same can be concluded for both the use of simulations with TI and different wind speeds. Performing simulations including TI increases the fidelity of the simulation, and thus the extracted center line.

Performing simulations with different wind speeds enables the analysis of the effect of the wind speeds on the dynamic center line behaviour. Broader simulation cases enables the identification of a more robust model.

2. In extending the current goal of identifying a dynamic yaw model, future work should include the use of staircase or multiple short pulse input sequences. For the latter, the multiple pulses should be of different amplitude. Further inputs can be used to identify a model that is robust to changes in simulation properties besides the yaw amplitude. For example changes in wind speed and the yaw velocity. Note that performing the SOWFA simulations is computational expensive and therefore time consuming, limiting possibilities of extensive simulation cases and input sequences.

3. The current study could be extended by using less center line observables in the DMDc identification process, as are used in the MOESP identification. From this, a trade-off can be made between the amount of states required to model the center line accurately and the gain in computational efficiency of the model. Research on the effect of the improper FLORIDyn center line dynamics in a MPC framework is required to make this trade-off.

4. As the data used in the identification process was limited, so was the data used in the validation process. Further research should validate the 10 deg and 20 deg models not only with the 2T 15 deg case, but also with corresponding 1T case. This could include extracting the 15 deg center line and using this data to validate the simulated center lines from the identified models.

5. With the use of turbulence free data, the FLORIDyn parameters are not tuned to obtain a generated power output without an offset to the validation data in the 2T case. Future research is needed to show the acquired power output dynamics without a offset to the validation data.

6. The framework proposed in this thesis can be extended to identify models for other dynamic turbine states. For example, from the same SOWFA data, the wake width can be extracted. This opens up the possibility of using both the center line and wake width data to estimate multiple dynamic states in the least squares parameter estimation.

Appendix A

Additional center line and dynamic yaw results

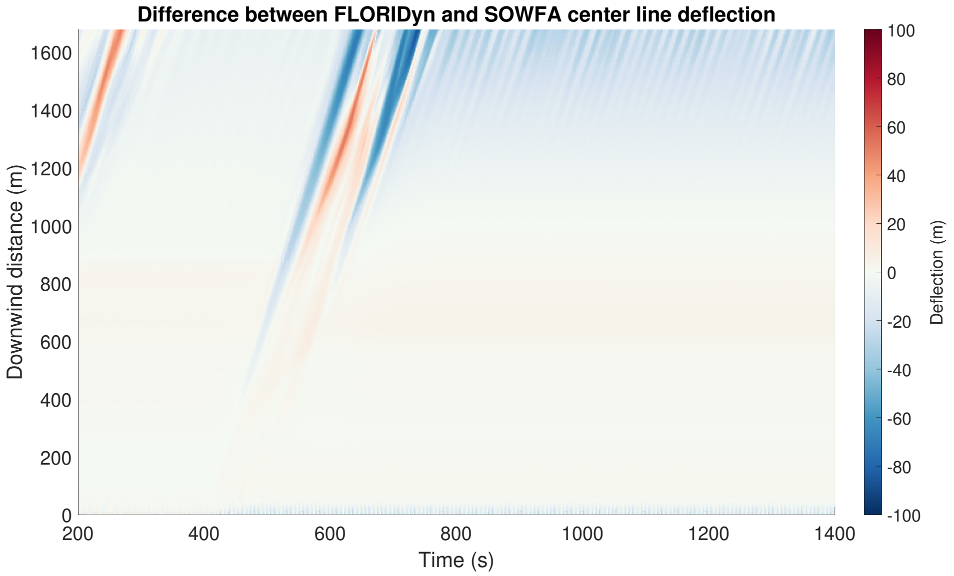

Figure A-1: Surface plot of the difference between SOWFA and FLORIDyn center line deflection over both time and downwind distance for the $20\,\text{deg}$ case.

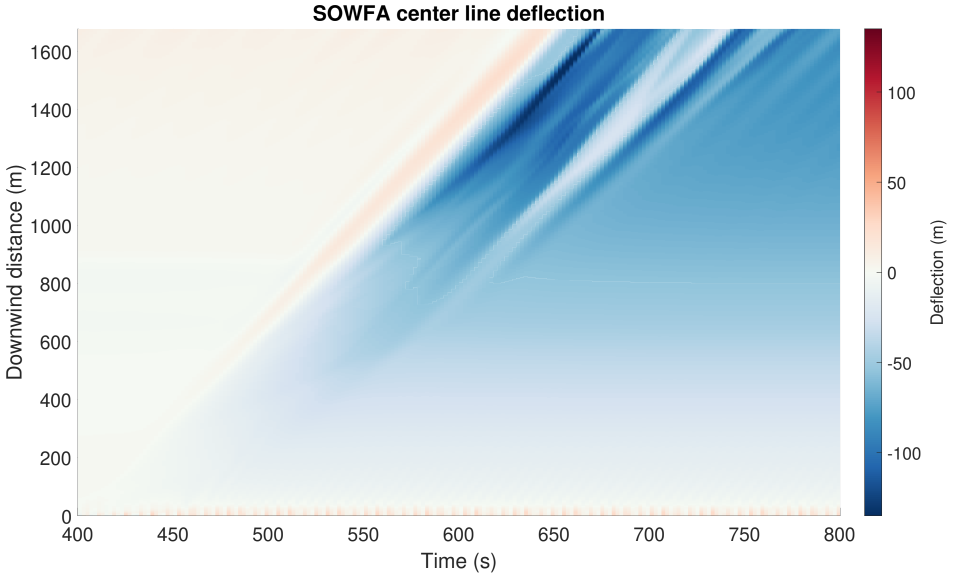

Figure A-2: Surface plot of the center line deflection over both time and downwind distance for the $20\,$deg case. Note that the steady state deflection is negative due to the snapshot orientation.

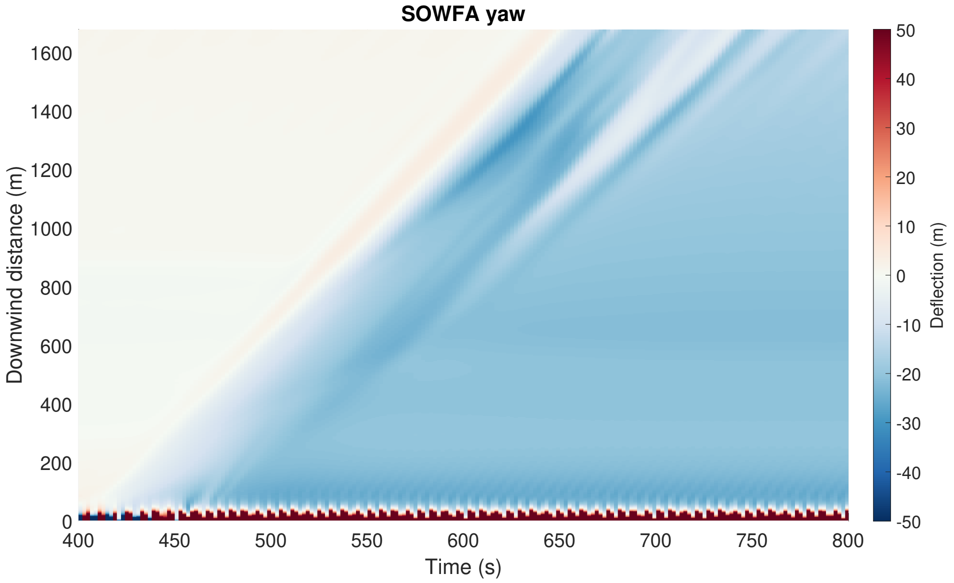

Figure A-3: Surface plot of the dynamic SOWFA yaw over both time and downwind distance for the $20\,$deg case. Note that the steady state yaw is negative due to the use of original deflection data. The yaw close to the turbine ranges from -2171.4 to $724.9\,$deg. To still show the important dynamics, this range is not fully included.

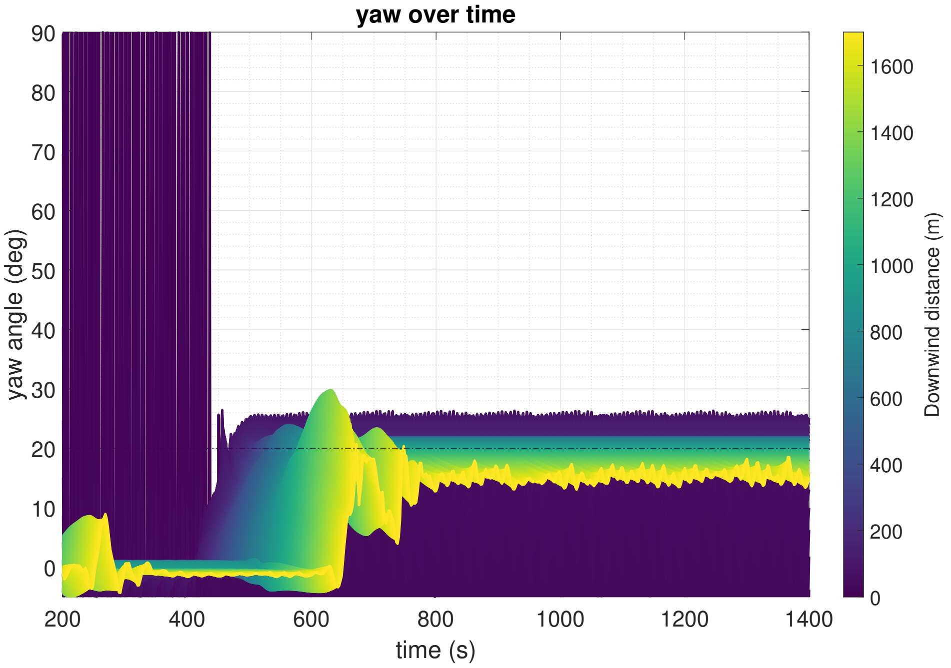

Figure A-4: SOWFA yaw over time for all downwind distances for the 20 deg case. Note how the yaw close to the turbine blows up do to deflection close to the turbine. The yaw close to the turbine ranges from -2171.4 to 724.9 deg. To still show the important dynamics, this range is not fully included.

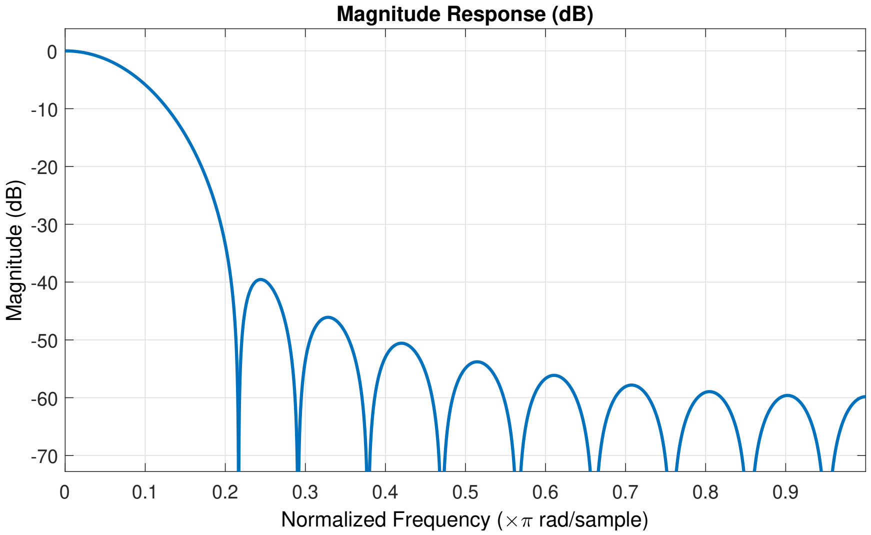

Figure A-5: The applied Kaiser filter. The filter is applied in both directions to obtain a zero-phase filter.

Appendix B

Additional system identification results

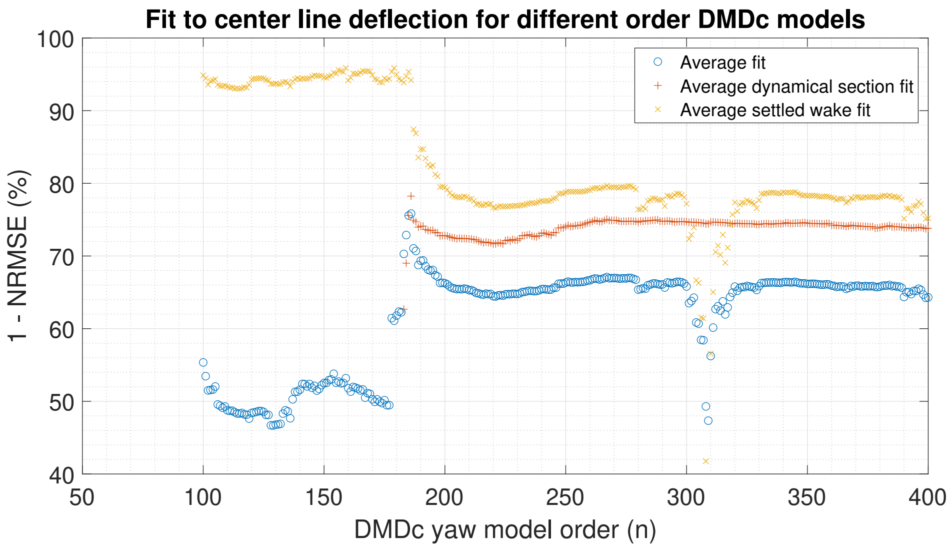

Figure B-1: Fit between the 10 deg yaw step SOWFA and DMDc model simulated center lines for model order 50 to 400. The dynamical section includes the center line between 440 to 800 s of the simulation. The settled wake includes the center line fit from 900 **s** and onward.

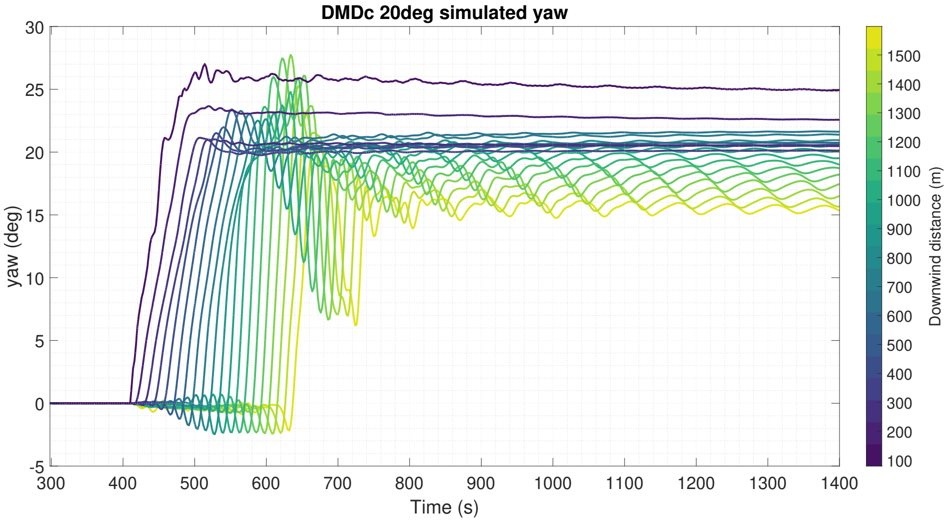

Figure B-2: Contour plot of the simulated yaw by the $20\,\text{deg}DMDcmodel$.

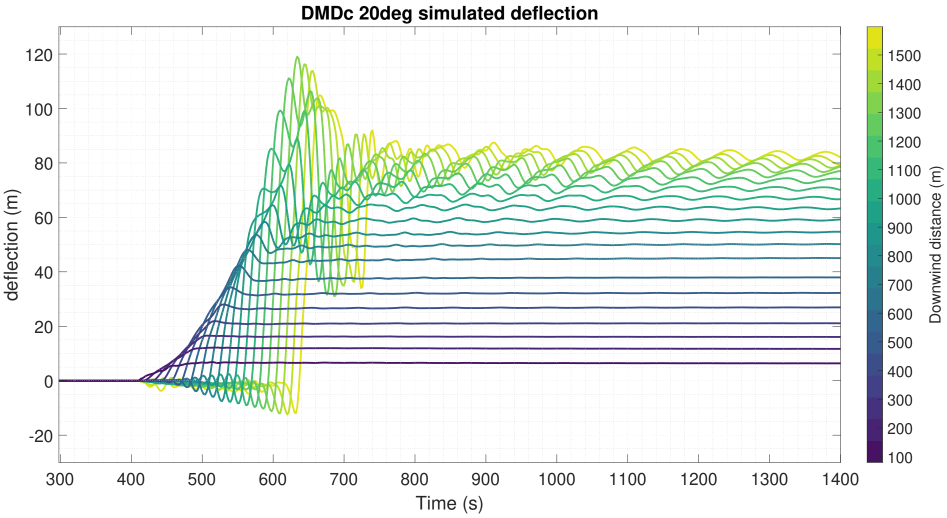

Figure B-3: Contour plot of the simulated center line deflection by the $20\,\text{deg}$ DMDc model.

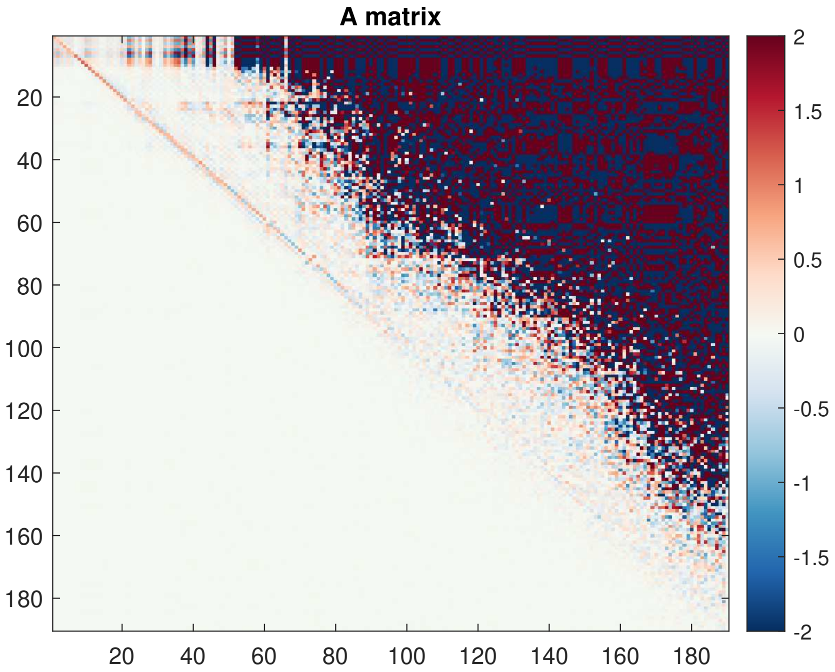

(a) A matrix

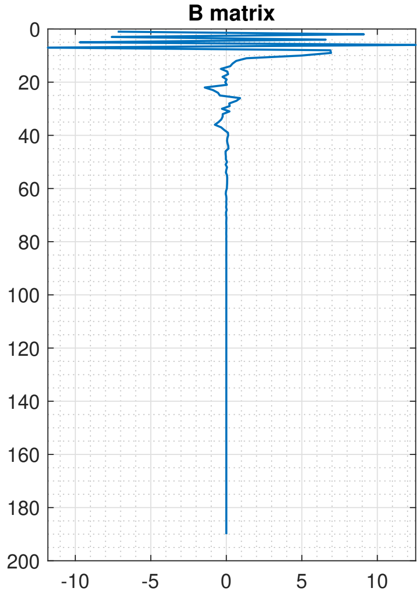

(b) B matrix (vector)

Figure B-4: A and B matrix of the DMDc ROM, note that the colorbar is limited by -2 and 2, while there are values outside of this range.

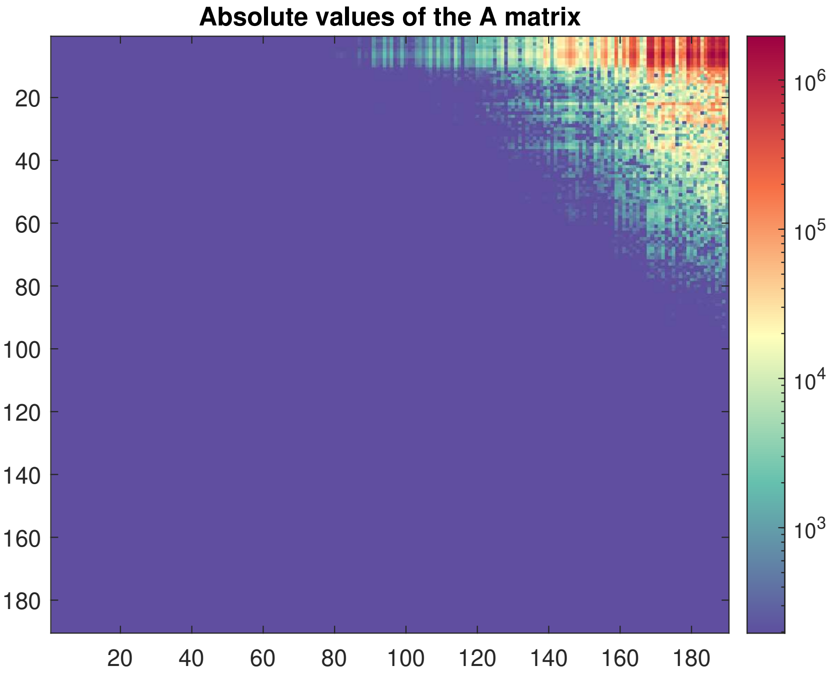

Figure B-5: Absolute values of the A matrix

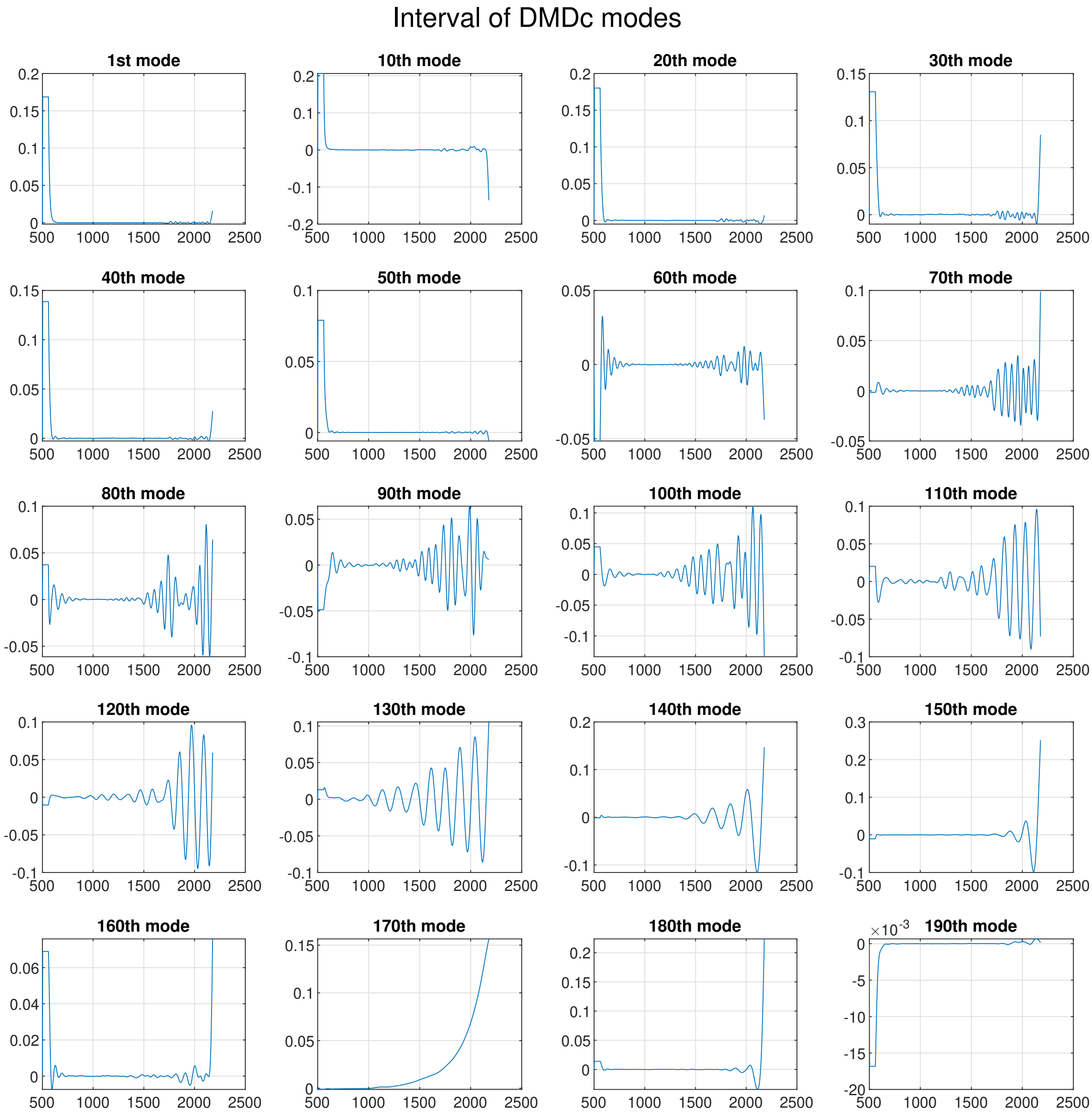

Figure B-6: 20 different DMDc modes

Appendix C

Additional FLORIDyn results

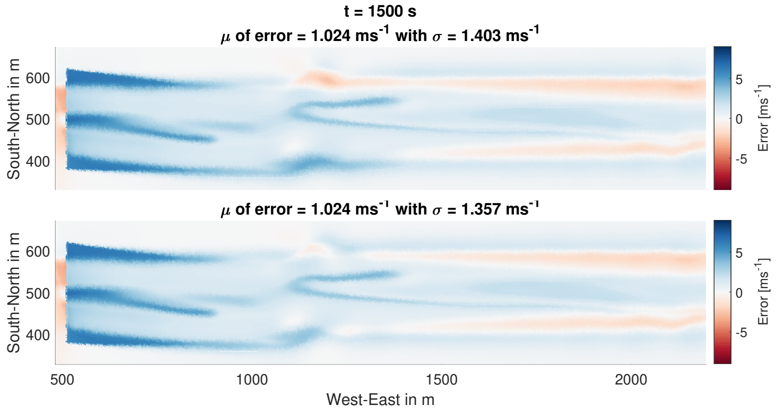

(a) Error plot at t $= 1500$ s. Without and with dynamics respectively.

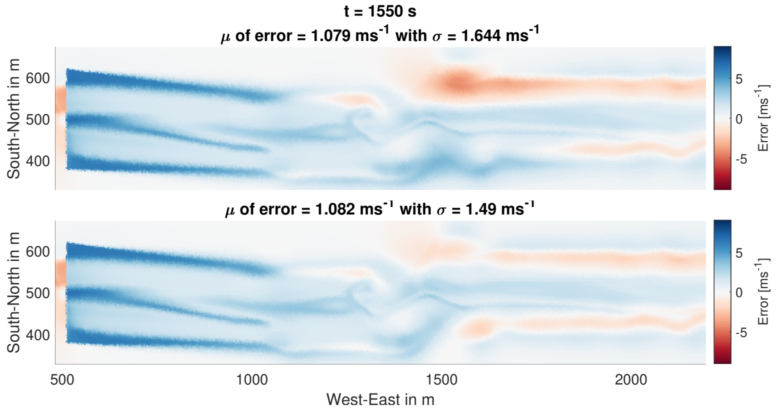

(b) Error plot at t $= 1550$ s. Without and with dynamics respectively.

Figure C-1: Error plot between FLORIDyn and SOWFA for different time steps. Both without and with center line dynamics. The error is defined as the wind velocities from SOWFA $-$ FLORIDyn.

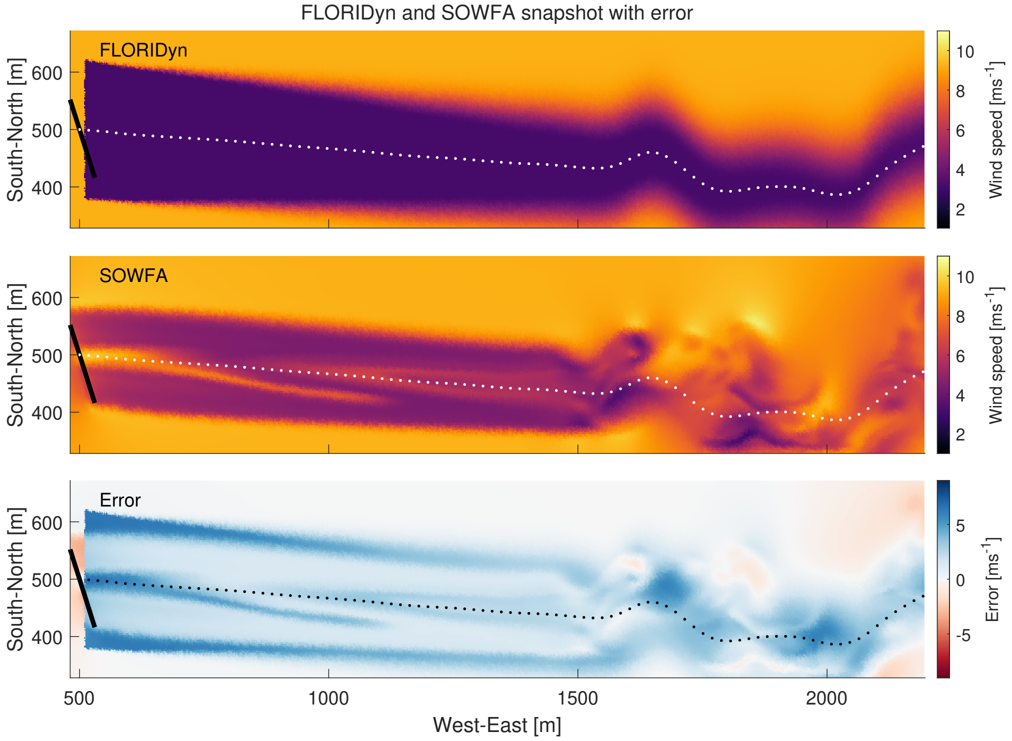

(a) Snapshots at t $= 1550\,$s

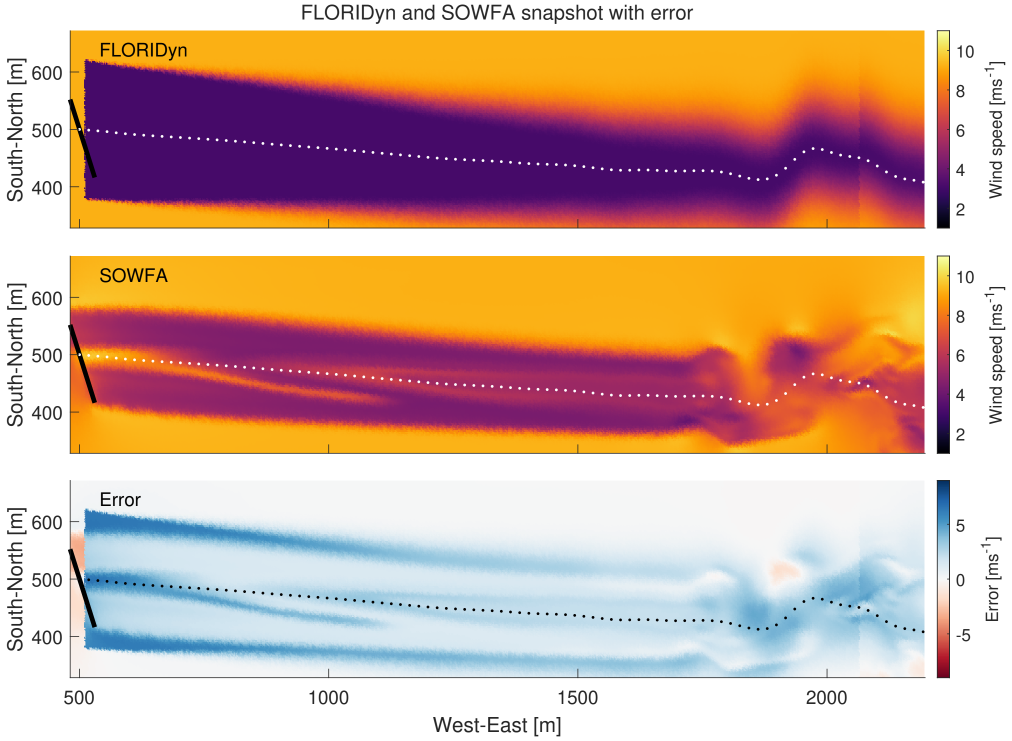

(b) Snapshots at t $= 1600\,$s

Figure C-2: FLORIDyn with center line dynamics, SOWFA and Error plot at t $= 1700\,$s and t $= 1600\,$s. The error is defined as the wind velocities from SOWFA $-$ FLORIDyn. Furthermore, the FLORIDyn center line is shown in all plots.

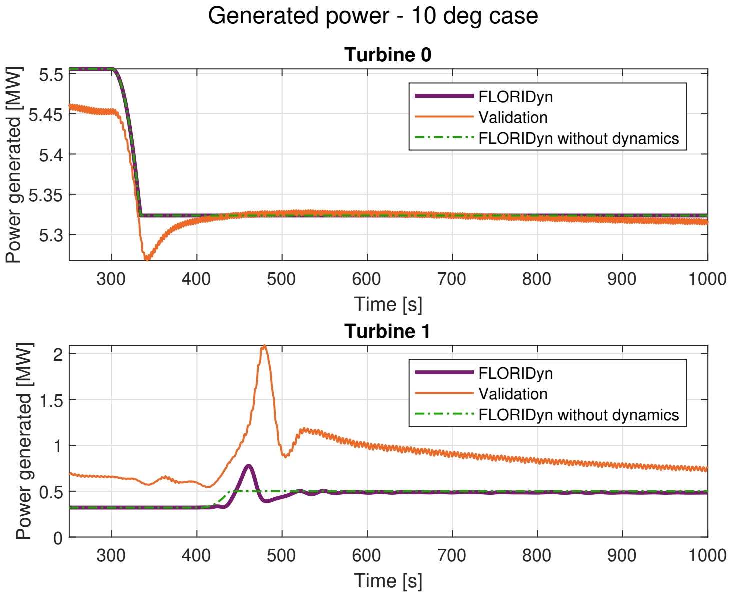

(a) Generated power output.

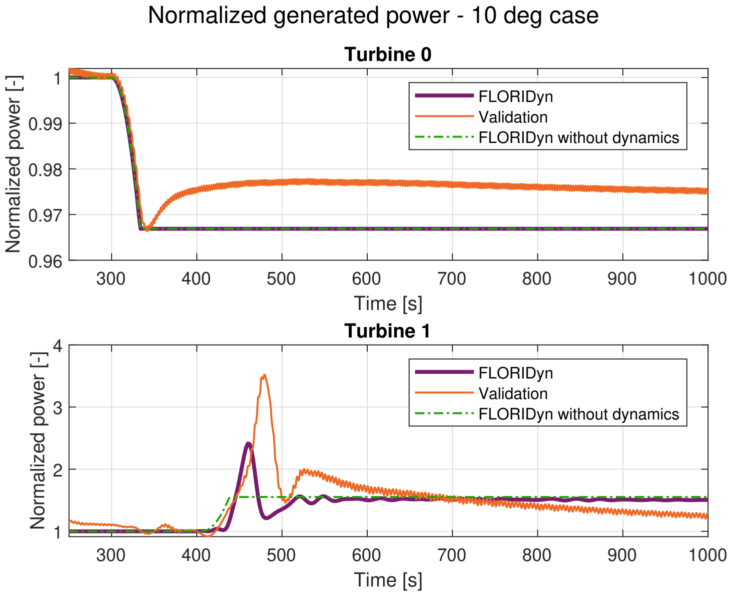

(b) Normalized generated power output.

Figure C-3: Both the generated power output and normalized power output of the $10\,\mathrm{deg}$ 2T case. For T1, the output of both the simulation with and without center line dynamics is visualised.

Bibliography

[1] Jennifer Annoni, Pieter Gebraad, and Peter Seiler. "Wind farm flow modeling using an input-output reduced-order model". In: *2016 american control conference (acc)*. IEEE. 2016, pp. 506–512.

[2] Majid Bastankhah and Fernando Porté-Agel. "Experimental and theoretical study of wind turbine wakes in yawed conditions". In: *Journal of Fluid Mechanics* 806 (2016), p. 506.

[3] M Becker. "Maturing FLORIS towards a Dynamic Wind Farm Model". In: (2020).

[4] M. Becker, D. Allaers, and J.W. Van Wingerden. "FLORIDyn - A dynamic and flexible framework for real-time wind farm control". In: (2022).

[5] Marcus Becker et al. "The revised FLORIDyn model: Implementation of heterogeneous flow and the Gaussian wake". In: *Wind Energy Science Discussions* (2022), pp. 1–25.

[6] S Boersma et al. "A control-oriented dynamic wind farm flow model:"WFSim"". In: *Journal of Physics: Conference Series*. Vol. 753. 3. IOP Publishing. 2016, p. 032005.

[7] Sjoerd Boersma et al. "A control-oriented dynamic wind farm model: WFSim". In: *Wind Energy Science* 3.1 (2018), pp. 75–95.

[8] Sjoerd Boersma et al. "A tutorial on control-oriented modeling and control of wind farms". In: *2017 American control conference (ACC)*. IEEE. 2017, pp. 1–18.

[9] T Burton et al. "Wind Energy Handbook Second Edition [Internet]". In: (2011).

[10] Rebecca L Busby. *Wind power: The industry grows up*. PennWell Books, 2012.

[11] Eduardo F Camacho and Carlos Bordons Alba. *Model predictive control*. Springer science & business media, 2013.

[12] CNN. *The stakes couldn't be higher for America's first major offshore wind farm*. 2021. URL: https://edition.cnn.com/2021/05/16/business/offshore-wind-farm-vineyard-wind/index.html.

[13] TU Delft. *FRED*. June 2021. URL: https://github.com/TUDelft-DataDrivenControl/FRED.

[14] Science Direct. *MPC literature summary*. URL: `https://www.sciencedirect.com/topics/engineering/predictive-control-model`.

[15] Bart M Doekemeijer, Daan van der Hoek, and Jan-Willem van Wingerden. “Closed-loop model-based wind farm control using FLORIS under time-varying inflow conditions”. In: *Renewable Energy* 156 (2020), pp. 719–730.

[16] Paul Fleming et al. “A simulation study demonstrating the importance of large-scale trailing vortices in wake steering”. In: *Wind Energy Science* 3.1 (2018), pp. 243–255.

[17] GE. *Haliade-X offshore wind turbine*. 2021. URL: `https://www.ge.com/renewableenergy/wind-energy/offshore-wind/haliade-x-offshore-turbine`.

[18] Pieter MO Gebraad and JW Van Wingerden. “A control-oriented dynamic model for wakes in wind plants”. In: *Journal of Physics: Conference Series*. Vol. 524. 1. IOP Publishing. 2014, p. 012186.

[19] Pieter MO Gebraad et al. “Wind plant power optimization through yaw control using a parametric model for wake effects—a CFD simulation study”. In: *Wind Energy* 19.1 (2014), pp. 95–114.

[20] IRENA. *Offshore Wind Capacity Goal*. 2018. URL: `https://twitter.com/IRENA/status/1042581608342011904/photo/1`.

[21] Niels Otto Jensen. “A note on wind generator interaction”. In: (1983).

[22] Jason M Jonkman et al. “Development of fast. farm: A new multi-physics engineering tool for wind-farm design and analysis”. In: *35th Wind Energy Symposium*. 2017, p. 0454.

[23] Ali C Kheirabadi and Ryozo Nagamune. “A quantitative review of wind farm control with the objective of wind farm power maximization”. In: *Journal of Wind Engineering and Industrial Aerodynamics* 192 (2019), pp. 45–73.

[24] J Nathan Kutz et al. *Dynamic mode decomposition: data-driven modeling of complex systems*. SIAM, 2016.

[25] Ewan Machefaux et al. “Empirical modeling of single-wake advection and expansion using full-scale pulsed lidar-based measurements”. In: *Wind Energy* 18.12 (2015), pp. 2085–2103.

[26] Karl Nilsson et al. “Large-eddy simulations of the Lillgrund wind farm”. In: *Wind Energy* 18.3 (2015), pp. 449–467.

[27] NREL. *Simulator for Offshore Wind Farm Applications*. June 2021. URL: `https://github.com/dcsale/SOWFA`.

[28] A O’Carroll et al. “Correlation of the rain erosion performance of polymers to mechanical and surface properties measured using nanoindentation”. In: *Wear* 412 (2018), pp. 38–48.

[29] OpenCFD. *OpenFOAM*. June 2021. URL: `https://www.openfoam.com/`.

[30] European Parliament. *Offshore wind energy in Europe*. Oct. 2020. URL: `https://www.europarl.europa.eu/thinktank/en/document.html?reference=EPRS_BRI(2020)659313`.

[31] Joshua L Proctor, Steven L Brunton, and J Nathan Kutz. “Dynamic mode decomposition with control”. In: *SIAM Journal on Applied Dynamical Systems* 15.1 (2016), pp. 142–161.

[32] Joshua L Proctor and Philip A Eckhoff. “Discovering dynamic patterns from infectious disease data using dynamic mode decomposition”. In: *International health* 7.2 (2015), pp. 139–145.

[33] Eliot Quon. “A set of python-based tools for rotor wake analysis”. In: (2017). URL: https://ewquon.github.io/waketracking/methodology.html.

[34] Peter J Schmid. “Dynamic mode decomposition of numerical and experimental data”. In: *Journal of fluid mechanics* 656 (2010), pp. 5–28.

[35] Jared J Thomas, Pieter MO Gebraad, and Andrew Ning. “Improving the FLORIS wind plant model for compatibility with gradient-based optimization”. In: *Wind Engineering* 41.5 (2017), pp. 313–329.

[36] Maarten J Van den Broek and Jan-Willem Van Wingerden. “Dynamic Flow Modelling for Model-Predictive Wind Farm Control”. In: *Journal of Physics: Conference Series*. Vol. 1618. 2. IOP Publishing. 2020, p. 022023.

[37] Frans Van Hulle et al. “Integrating Wind. Developing Europe’s power market for the large-scale integration of wind power”. In: (2009).

[38] M Verahegen and Patrick Dewilde. “Subspace model identification. part i: The output-error state-space model identification class of algorithm”. In: *Int. J. Control* 56 (1992), pp. 1187–1210.

[39] Michel Verhaegen and Patrick Dewilde. “Subspace model identification part 2. Analysis of the elementary output-error state-space model identification algorithm”. In: *International journal of control* 56.5 (1992), pp. 1211–1241.

[40] Michel Verhaegen and Vincent Verdult. *Filtering and System Identification: A Least Squares Approach*. Cambridge University Press, 2007. DOI: 10.1017/CBO9780511618888.

[41] Helmut Vogel. “A better way to construct the sunflower head”. In: *Mathematical Biosciences* 44.3 (1979), pp. 179–189. ISSN: 0025-5564. DOI: https://doi.org/10.1016/0025-5564(79)90080-4. URL: https://www.sciencedirect.com/science/article/pii/0025556479900804.

Glossary

List of Acronyms

CFD	Computational Fluid Dynamics
D	Diameter of turbine rotor plane
DMD	Dynamic Mode Decomposition
DMDc	Dynamic Mode Decomposition with Control
FLORIDyn	FLOw Redirection and Induction Dynamics
FLORIS	FLOw Redirection and Induction in Steady-state
GW	Giga Watts
IREA	International Renewable Energy Agency
LES	Large Eddy Simulation
MOESP	Multivariable Output Error State sPace
MPC	Model Predictive Control
MW	Mega Watts
OPs	Observation Points
pchip	Piecewise Cubic Hermite Interpolating Polynomial
ROM	Reduced Order Model
RQ decomposition	Decomposition of a matrix in both an upper triangular (R) and orthogonal (Q) matrix
SIMO	Single-Input Multiple-Output
SISO	Single-Input Single-Output
SOWFA	Simulator for Offshore Wind Farm Applications
SVD	Singular Value Decomposition
T0/T1	Turbine 0/1
TI	Turbulence Intensity
TWF	Temporary Wind Farm